Periodic structures : transmission invariance and symmetry effects

Elie Salemeh

COLLEGE DOCTORAL PAYS DE LA LOIRE
SCIENCES DE L'INGENIERIE ET DES SYSTEMES

Le Mans Université

THESE DE DOCTORAT

DE
LE MANS UNIVERSITE
SOUS LE SCEAU DE
LA COMUE ANGERS – LE MANS

ECOLE DOCTORALE N° 602
Sciences de l'Ingénierie et des Systèmes
Spécialité : Acoustique

Par
Elie SALEMEH

Periodic structures: transmission invariance and symmetry effects

Numéro National de Thèse : 2024LEMA1010

Thèse présentée et soutenue au Mans, le 04/07/2024
Unité de recherche : LAUM, UMR CNRS 6613

Composition du Jury :

Rapporteurs :	Jean-François MERCIER	Directeur de Recherche CNRS, ENSTA Paris, Paris, France
	Tony VALIER-BRASIER	Maitre de conférence, Institut Jean Le Rond d'Alembert, Paris, France
Examinateurs :	Matthieu DAVY	Professeur, IETR, Rennes, France
	Agnès MAUREL	Directrice de Recherche CNRS, Institut Langevin, Paris, France
	Vicent ROMERO-GARCIA	Professeur, Université Polytechnique de Valence, Espagne
Dir. de thèse :	Simon FELIX	Directeur de Recherche CNRS, LAUM, Le Mans, France
Co-dir. de thèse :	Vincent PAGNEUX	Directeur de Recherche CNRS, LAUM, Le Mans, France

Remerciements

Tout d'abord, je tiens à exprimer ma sincère gratitude à Simon Félix et Vincent Pagneux pour m'avoir proposé ce sujet de thèse. Je les remercie pour leur disponibilité à tout moment, pour les réunions hebdomadaires, ainsi que pour leur patience et leur bienveillance tout au long de ce parcours. Je les remercie également pour les connaissances scientifiques qu'ils m'ont transmises, ainsi que le goût et la curiosité pour la recherche scientifique. Une mention spéciale pour la curiosité que nous avons explorée au cours de nos recherches, notamment celle concernant le champ convergent malgré la divergence de la matrice de transfert, ainsi que pour les échanges enrichissants que nous avons eus au Colorado. Ils m'ont aussi fait découvrir de nombreux aspects de la culture française.

Je souhaite exprimer mes sincères remerciements à Mme Agnès Maurel d'avoir accepté la présidence du jury, ainsi qu'à MM. Jean-François Mercier et Tony Valier-Brasier pour avoir accepté de rapporter cette thèse, participant ainsi à l'enrichissement de ces travaux. Je remercie également Matthieu Davy et Vincent Romero-Garcia pour avoir accepté d'examiner cette thèse et pour leur participation en tant que membres du Comité de Suivi Individuel, ainsi que pour les discussions constructives que nous avons eues lors de nos réunions annuelles.

Cette thèse a été préparée au Laboratoire d'Acoustique de l'Université du Mans. Je tiens à remercier pleinement l'ensemble du personnel du LAUM pour l'ambiance de travail agréable qui règne au sein du laboratoire. Un grand merci à toutes les personnes avec qui j'ai pu échanger sur divers sujets. Ces conversations ont cultivé ma curiosité scientifique. Je souhaite exprimer ma reconnaissance à Jean-Philippe Groby, Guillaume Penelet et Gaëlle Poignand pour nos discussions sur la thermoacoustique, ainsi qu'à Stéphane Lebon, James Blondeau et Hervé Mézière pour leur contribution à l'expérience que j'ai réalisée au laboratoire du LAUM.

Durant les trois premières années de thèse, j'ai bénéficié d'une mission complémentaire en enseignement. Je tiens à exprimer ma sincère gratitude à Frédéric Ablitzer, Bertrand Lihoreau, Olivier Richoux et Najat Tahani, aux côtés desquels j'ai eu beaucoup de plaisir à m'impliquer dans l'enseignement. Un grand merci particulier à Najat pour son soutien et son encouragement tout au long de cette thèse. Durant la quatrième année, j'ai bénéficié

d'un contrat d'enseignement et de recherche en CNU 63, ce qui m'a permis d'élargir mes connaissances, d'accroître mon expérience en enseignement et de finaliser la rédaction de ma thèse. Je remercie Pascal Picart de m'avoir donné cette opportunité et pour toute l'aide qu'il m'a apportée dans la préparation des cours. Je remercie également Denis Mounier pour ses explications et son aide dans le montage des expériences en salle de TP.

Je tiens à remercier l'association RAmDAM pour les événements qu'elle a organisés, notamment le cabinet de curiosité auquel j'ai eu le plaisir de contribuer. Je remercie l'ancien président Guilhem Pages et l'ancien trésorier Nicolas Pajusco pour nos échanges sur la terrasse au 4ème étage et au pub. Je remercie également les membres du LAUM à l'UFR et à l'ENSIM pour les échanges que nous avons eus durant les pauses café et les sorties.

Pour finir, je tiens à remercier mes parents et mes beaux-parents pour leurs encouragements, sans lesquels je n'aurais jamais pu prendre la trajectoire qui est la mienne aujourd'hui. Un immense merci à ma femme Claire pour son soutien inconditionnel et ses encouragements.

Table of Contents

Chapter 1

Introduction: Wave transport in complex media

Interferences are crucial in wave transport through complex media, significantly influencing the scattering characteristics and leading to numerous wave control applications. One example is the band structure of the transmission spectrum in periodic media [1]. Other examples are conductance fluctuations or Anderson localization in disordered media [2–4]. In this manuscript, we show that we can observe phenomena such as freezing of the speckle pattern or transmission enhancement due to symmetry in both random and periodic media, even if they host different natures of wave propagation.

Disordered media can be constructed experimentally (Fig. 1.1 (a)). They can be found in nature, such as in certain biological media (Fig. 1.1 (b)), but also in our atmosphere on a foggy winter morning (Fig. 1.1 (c)).

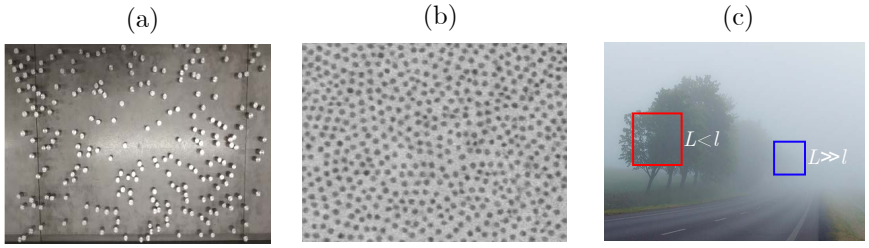

Figure 1.1 – Disordered media. (a) Random distribution of aluminum cylinders in rectangular waveguides. Source: E. Chéron [5]. (b) TEM image of an arrangement of collagen fibrils in the human cornea by G. Latour. Source: O. Leseur [6]. (c) Imaging through fog. It is composed of small water droplets that scatter light. Red square: Imaging through a fog layer thinner than the transport mean free path l. The image is slightly degraded. This parameter represents the typical distance after which the wave loses memory of its initial direction. Blue square: Image through a layer of fog much larger than l. The image is so degraded that the sharp features of any object are no longer discernible. Source: Wikimedia Commons.

When light interacts with such disordered media, it is scattered by the particles that constitute the media. The cumulative effect of these diffusion events results in the generation of constructive or destructive interferences at every point in space. Consequently, when we examine the transmitted light intensity on a screen, we encounter the intricate complex patterns of these interferences, often referred to as "speckle patterns". Fig. 1.2 serves as an illustrative example. These speckle patterns are highly sensitive to the nature and position of the scatterers and the excitation source.

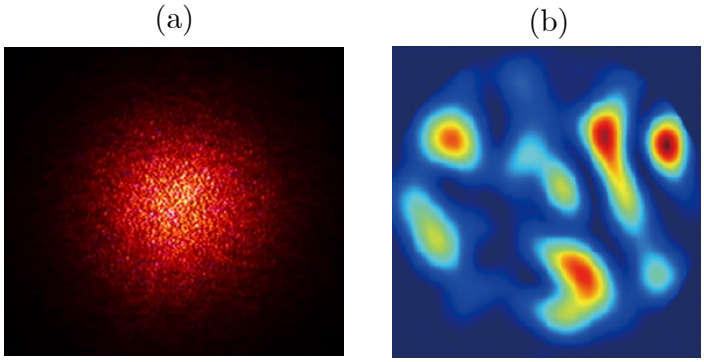

Figure 1.2 – Transmitted speckle pattern. (a) Through a 70 $\boldsymbol{u}$m sample composed of silica beads with a diameter of 400 nm, illuminated by a He-Ne laser. Measurement carried out by E. Perros. Source: O. Leseur [6]. (b) Through a 40 cm sample composed of alumina spheres with a diameter of 0.95 cm, illuminated by a source at a frequency in the range of 14.70–14.94 GHz. Source: Z. shi [7].

Taking an illustrative example of a disordered media, such as the fog (Fig. 1.1 (c)), we can effectively distinguish two distinct regions of interest. The first region exhibits minimal degradation in imaging quality, allowing us to see the tree clearly. In contrast, the second region demonstrates significant degradation, to the point where sharp object features become imperceptible. The degradation of image quality depends on how and how much light is scattered. This degradation is intricately linked to the properties of the medium through which light propagates and can be quantified by a fundamental parameter known as the transport mean free path, denoted as l [8]. This parameter represents the typical distance after which the wave loses the memory of its initial direction. Thus, at a distance L smaller than l, only a small fraction of light has been scattered, resulting in a minimal reduction in imaging quality. This corresponds to the ballistic regime. For $L \gg l$, essentially all of the light has been scattered, corresponding to the diffusive regime, also known as the metallic regime. A third regime can be defined; the localized regime.

In this regime, after a characteristic distance ξ, $L \gg \xi$, the wave is trapped inside the disorder due to interferences; diffusion no longer occurs, and there is a transition between the diffusive and the localized regime. Localization was originally discovered by P. W. Anderson when he observed the absence of diffusion when electron propagation takes place in a highly disordered potential [9]. Anderson localization has become a central concept in wave physics. Localization has been clearly established in electronics [10], acoustics [11, 12], electromagnetic waves [13], and optics [14, 15]. Fig. 1.3 summarizes the transport regimes in disordered media.

Figure 1.3 – Schematic representation of different transport regimes as a function of the disordered medium length L.

In this introductory chapter, we first present the solution of the wave equation in a 2D waveguide in a multimodal formulation. We introduce some quantities and useful tools that allow us to characterize the different transport regimes in disordered waveguides. We then highlight the sensitivity of the transmitted pattern to the incidence conditions in the diffusive regime, which is due to the transmission properties in this regime. In contrast, in the localized regime, the transmitted pattern is insensitive to the incidence conditions [7, 16]. Finally, we introduce the next chapters.

1.1 2D waveguide

1.1.1 Solution of the wave equation and scattering matrix

Consider an infinite 2D waveguide with unitary width and rigid boundaries, where scatterers are randomly distributed in the region $x \in [0, L]$, see Fig. 1.4. In this disor-

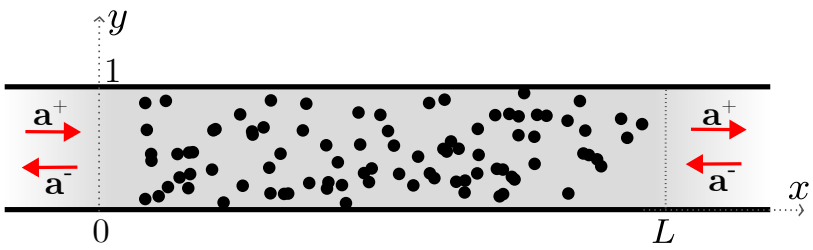

Figure 1.4 – Schematic representation of an inhomogeneous medium of length L placed in an infinite waveguide. The black points represent scatterers modeled as local index changes.

dered waveguide, we consider that the propagation of a wave $\psi(x, y)$ is governed by the Helmholtz equation

$$\Delta\psi(x, y) + k^2[1 + \delta n(x, y)]\psi(x, y) = 0, \tag{1.1}$$

where k is the wave number in the homogeneous medium and $-1 < \delta n(x, y) < 1$ models the change in the local index of the scatterers. We impose Neumann boundary conditions on the waveguide walls

$$\left.\frac{\partial\psi}{\partial y}\right|_{y=0,1} = 0. \tag{1.2}$$

In the two homogeneous regions of the waveguide ($x \leq 0$ and $x \geq L$), we use the modal decomposition of the wave field $\psi(x, y)$

$$\psi(x, y) = \sum_n a_n(x) g_n(y), \tag{1.3}$$

with $g_n(y)$ the solution of the the transverse eigenproblem

$$g_n'' = -\gamma_n^2 g_n. \tag{1.4}$$

These transverse modes are

$$g_n(y) = \sqrt{2 - \delta_{n0}} \cos(\gamma_n y), \tag{1.5}$$

with the eigenvalues $\gamma_n = n\pi$ and $n \in \mathbb{N}$. They form a basis of orthogonal functions satisfying the relations,

$$(g_n, g_m) = \delta_{nm} \quad \text{and} \quad (g'_n, g'_m) = \gamma_n^2 \delta_{nm}, \tag{1.6}$$

with

$$(f_1, f_2) = \int_0^1 f_1 f_2^* \, \mathrm{d}y \tag{1.7}$$

the scalar product.

By projecting the Helmholtz equation onto the basis of the g_n functions, we obtain the second-order equation

$$a_n''(x) + \alpha_n^2 a_n(x) = 0, \tag{1.8}$$

where

$$\alpha_n = \sqrt{k^2 - \gamma_n^2} \tag{1.9}$$

is the longitudinal wave number associated with mode n. Eq. (1.9) separates the N propagating transverse modes for which $\alpha_n \in \mathbb{R}^+$ and the evanescent transverse modes for which $\alpha_n \in \mathrm{i}\mathbb{R}^+$. The solution of the second-order equation (Eq. (1.8)) reads as a sum of right-going ($c_n^+ \mathrm{e}^{\mathrm{i}\alpha_n x}$) and left-going ($c_n^- \mathrm{e}^{-\mathrm{i}\alpha_n x}$) wave with amplitude $c_n^\pm$. Thus, at both ends of the scattering regions, the solution to the problem is as follows

$$\begin{aligned} \psi(x = 0, y) &= \sum_{n=0}^{N-1} \left(a_n^+(0) + a_n^-(0) \right) g_n(y) + \psi_{\mathrm{l}}^{(\mathrm{e})}, \\ \psi(x = L, y) &= \sum_{n=0}^{N-1} \left(a_n^+(L) + a_n^-(L) \right) g_n(y) + \psi_{\mathrm{r}}^{(\mathrm{e})}, \end{aligned} \tag{1.10}$$

where a_n^+ (resp. a_n^-) are the modal amplitudes of the right (resp. left) going wave, and $\psi_{\mathrm{l,r}}^{(\mathrm{e})}$ denotes the evanescent field.

To define the scattering matrix S, we restrict the above series to the N propagating modes and rewrite the wavefield as follows

$$\begin{aligned} \psi(x=0,y) &= \boldsymbol{g}^{\mathsf{T}}(y)\left(\boldsymbol{a}^{+}(0)+\boldsymbol{a}^{-}(0)\right), \\ \psi(x=L,y) &= \boldsymbol{g}^{\mathsf{T}}(y)\left(\boldsymbol{a}^{+}(L)+\boldsymbol{a}^{-}(L)\right), \end{aligned} \tag{1.11}$$

with $\boldsymbol{g} \equiv (g_n)$, $\boldsymbol{a}^{+} \equiv (a_n^{+})$ and $\boldsymbol{a}^{-} \equiv (a_n^{-})$ are vectors with N components. The incoming waves on the inhomogeneous medium $\boldsymbol{a}^{+}(0)$ and $\boldsymbol{a}^{-}(L)$ are related to the outgoing waves $\boldsymbol{a}^{-}(0)$ and $\boldsymbol{a}^{+}(L)$ by the scattering matrix S, which is of size $2N \times 2N$ and composed of reflection matrices R and R', as well as transmission matrices T and T' of the inhomogeneous medium,

$$\begin{pmatrix} \boldsymbol{a}^{-}(0) \\ \boldsymbol{a}^{+}(L) \end{pmatrix} = \begin{pmatrix} \mathsf{R} & \mathsf{T}' \\ \mathsf{T} & \mathsf{R}' \end{pmatrix} \begin{pmatrix} \boldsymbol{a}^{+}(0) \\ \boldsymbol{a}^{-}(L) \end{pmatrix}.$$

Since the scattering matrix is restricted to propagative components, with proper normalization the reciprocity property implies that S is symmetric, i.e., $\mathsf{S} = \mathsf{S}^{T}$, with S^{T} the transpose of S, and the energy conservation implies that S is unitary, i.e., $\mathsf{S}\mathsf{S}^{\dagger} = \mathsf{I}$, with $\dagger$ represents the adjoint operator of a complex matrix. For general relations verified by the S matrix with evanescent waves, see [17, 18].

1.1.2 Conductance and transmission eigenvalues

The different transport regimes in 2D disordered waveguides can be characterized by the conductance [19, 20] and by the transmission eigenvalues (TEVs) [21].

The dimensionless conductance g of the medium measures the total transmission due to the contribution of all incoming modes

$$g = \mathrm{Tr}\left(\mathsf{T}\mathsf{T}^{\dagger}\right) = \sum_{n,m=1}^{N} |T_{nm}|^2 . \tag{1.12}$$

To calculate the TEVs, we consider the singular value decomposition of the transmission matrix T; this decomposition gives the product of 3 matrices,

$$\mathsf{T} = \mathsf{U}\sqrt{\tau}\mathsf{V}^{\dagger}, \tag{1.13}$$

with $\tau = \mathrm{diag}(\tau_1, \ldots, \tau_n, \ldots, \tau_N)$ is a diagonal matrix containing the transmission eigenvalues, they are real numbers between 0 and 1, and the two complex unitary matrices $\mathsf{U} \equiv (\boldsymbol{U}_n)$ and $\mathsf{V} \equiv (\boldsymbol{V}_n)$ contain their corresponding eigenvectors. $\boldsymbol{U}_n$ (resp. $\boldsymbol{V}_n$) map the output (resp. input) field of transmission eigenchannels (TECs) to the lead propagating modes. The conductance can be expressed directly as a function of the TEVs,

$$g = \sum_{n=1}^{N} \tau_n. \tag{1.14}$$

Note that the transmission matrix T, which relates the modal amplitudes of the transmitted wave $\boldsymbol{a}^+(L)$ to the modal amplitudes of the incident wave $\boldsymbol{a}^+(0)$, can be written as a sum of rank-1 matrices

$$\mathsf{T} = \sum_{n=1}^{N} \sqrt{\tau_n} \boldsymbol{U}_n \boldsymbol{V}_n^\dagger, \tag{1.15}$$

thus, $\boldsymbol{a}^+(L)$ can be written as linear combination of the TEC ($\boldsymbol{U}_n$),

$$\boldsymbol{a}^+(L) = \sum_{n=1}^{N} b_n \tau_n \boldsymbol{U}_n, \tag{1.16}$$

with

$$b_n = \boldsymbol{V}_n^\dagger \boldsymbol{a}^+(0) \tag{1.17}$$

a scalar coefficient.

1.1.3 Random matrix theory (RMT)

The use of random matrices to analyze transmission in disordered systems [22–29] has proven to be an effective approach for determining the scaling and fluctuations of conductance and for determining the distribution of the TEVs.

The simulations presented in this document are based on the fact that the scattering matrix Qs for a portion of disordered media is generated through the Circular Orthogonal Ensemble (COE), characterized by unitary and symmetric matrices [30]. The corresponding Matlab function is:

```
function Qs=RMT_COE(N)
Z = (randn(2*N)+i*randn(2*N))/sqrt(2);
[Q,R] = qr(Z);
D = diag(R);
ph = D./abs(D);
Q = Q*diag(ph); %%% CUE: unitary matrix
Qs = Q*Q.'; %%% COE: unitary and symmetric matrix
end
```

The total scattering matrix S of a complete disordered medium of length L is then reconstructed by using iteratively the composition product, often referred to as the Redheffer star-product [31]:

$$\mathsf{S} = \mathrm{Qs}^{(1)} \star \ldots \star \mathrm{Qs}^{(m)} \star \ldots \star \mathrm{Qs}^{(M)}, \tag{1.18}$$

with $\mathrm{Qs}^{(m)}$ the scattering matrix of the mth portion, and $m = 1, \ldots, M$. An example is given in App. 1.A, which provides the procedures to obtain the total scattering matrix of two portions.

1.2 Diffusive regime

1.2.1 Statistical properties of the conductance and transmission eigenvalues

The diffusive regime is characterized by intermediate waveguide length, $1 \ll s \ll N$, with $s = L/l$ the scaling parameter. In this regime, by averaging over multiple configurations, the mean value of the conductance $\langle g \rangle$ obeys the law of Ohm

$$\langle g \rangle = \frac{N}{s+1}, \tag{1.19}$$

that is, $\langle g \rangle$ decreases with the length of the disordered waveguide according to an ohmic law. For a waveguide without disorder, the conductance can be normalized to the number of propagating modes N.

In this regime, the distribution of the conductance $\mathsf{P}(g)$ follows a Gaussian distribution [4, 28]. The central peak is centered at the mean value of the conductance, and the variance

δ_g remains constant, independent of the scaling parameter s:

$$\mathsf{P}(g) = \frac{1}{\sqrt{2\pi\delta_g}} \exp\left(\frac{-(g - \langle g\rangle)^2}{2\delta_g}\right), \tag{1.20}$$

with $\delta_g = \langle g^2\rangle - \langle g\rangle^2$ represents the variance of conductance. A numerical example is shown in Fig. 1.5 (a).

Furthermore, the distribution of the TEVs $\mathsf{P}(\tau)$ is bimodal [4, 28]:

$$\mathsf{P}(\tau) = \frac{N}{s+1} \frac{1}{\tau\sqrt{1-\tau}}. \tag{1.21}$$

A numerical example is shown in Fig. 1.5 (b). This distribution indicates that transmission is realized either by TEVs close to zero, indicating that the TECs are closed, i.e., the medium is opaque, or by TEVs close to unity, indicating that the TECs are open, i.e., the medium is transparent. This bimodal distribution is not symmetric, with more closed channels than open channels.

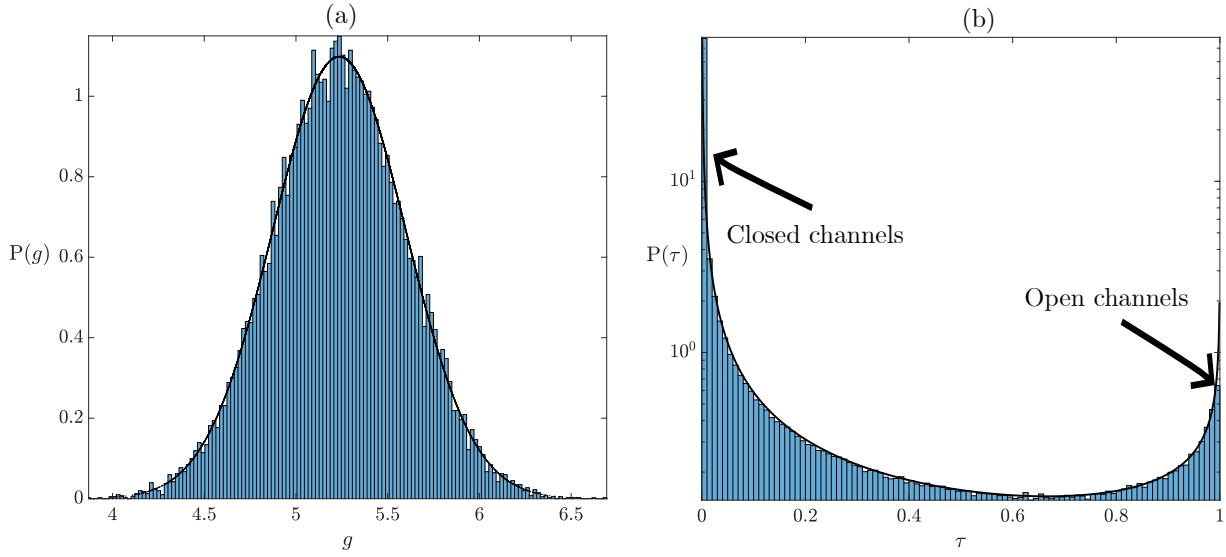

Figure 1.5 – (a) Conductance distribution. The solid line represents the Gaussian distribution given by Eq. (1.20). (b) Transmission eigenvalues distribution. The solid line represents the bimodal distribution given by Eq. (1.21). These distributions are generated from an RMT simulation based on 2.10^4 realizations for $N = 50$ and $s = 8$.

1.2.2 Sensitivity of the transmitted pattern

Let us consider a single configuration of a disordered medium ($1 > s \simeq 8 > N = 50$) placed in an infinite waveguide. Fig. 1.6 shows the spectrum of the conductance and the TEVs. It shows that the conductance is carried by several TEVs. Consequently, the transmitted wave is a linear combination of several TECs (Eq. (1.24)). The pattern of the transmitted field is sensitive to the incidence conditions.

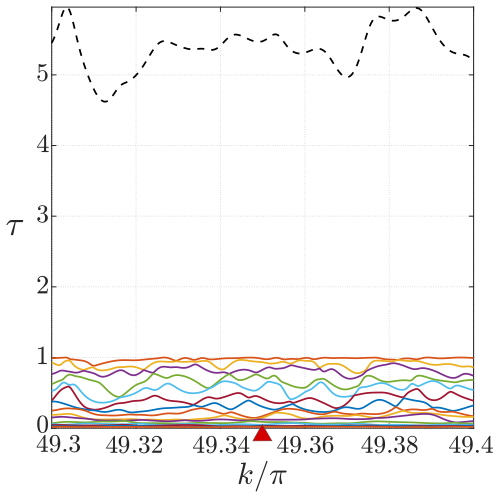

Figure 1.6 – Spectrum of the transmission eigenvalues (solid lines in colors) and conductance (dashed black line) of a disordered sample $s \simeq 8$ placed in an infinite waveguide supporting $N = 50$ propagating modes. The red triangle represents the frequency of excitation $k/\pi = 49.35$ used to simulate the wavefield in Fig. 1.7.

An example of such sensitivity is shown in Fig. 1.7 (a) and (b). A disordered waveguide is excited by two different incident conditions. An incident plane wave ($n = 0$) in Fig. 1.7 (a). An incident wave that corresponds to a higher-order mode ($n = 20$). Comparing both configurations allows us to observe the strong sensitivity of the wave pattern to the incidence conditions in the entire system.

By applying wavefront shaping to the incident wave, we can control the transmitted wave within a complex medium [33–35]. In practice, when the incident wave $\boldsymbol{a}^+(0)$ aligns with $\boldsymbol{V}_1$, the disordered medium can effectively become transparent. An example is shown in Fig. 1.7 (c). The wave entering the medium is almost entirely transmitted, with nearly zero reflection.

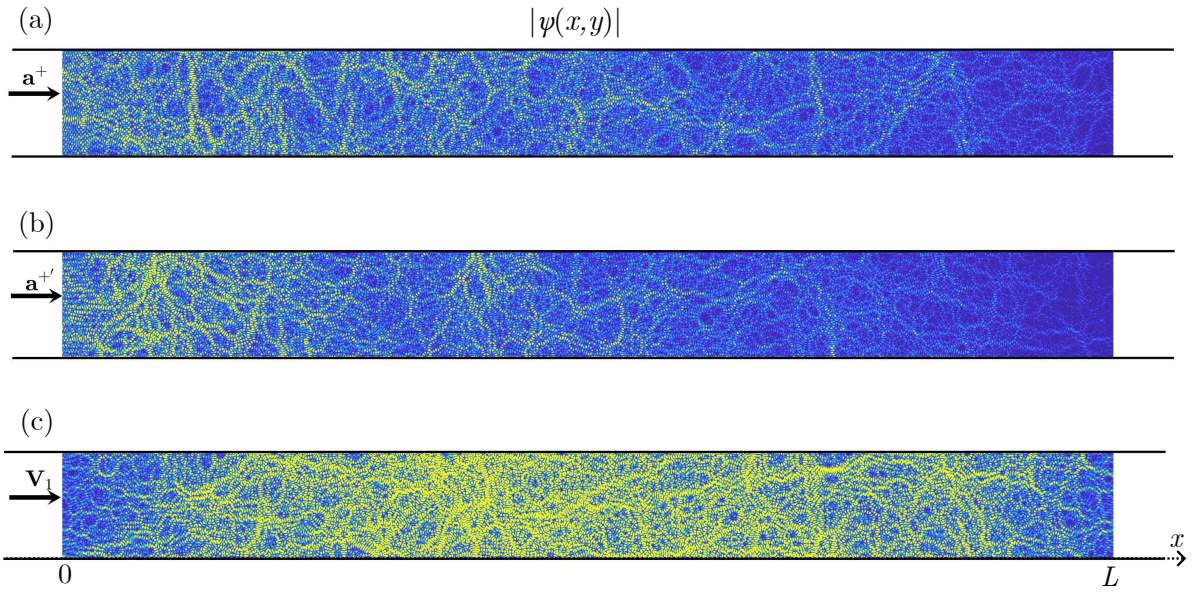

Figure 1.7 – Wavefield modulus in a disordered sample $s \simeq 8$ placed in an infinite waveguide for three different incident waves, at a frequency $k/\pi = 49.35$. (a) and (b) $\boldsymbol{a}^+(0) \equiv (\delta_{n,0})$ and $\mathbf{a}^{+'}(0) \equiv (\delta_{n,20})$. Here, δ represents the Dirac function. (c) For an incident wave shaped to match $\boldsymbol{V}_1$ associated with the largest eigenvalue τ_1. In this case, the transmission is almost perfect. Numerics are performed using a code developed by E. Chéron [32]

.

1.3 Localized regime

1.3.1 Statistical properties of the conductance and transmission eigenvalues

The localized regime is characterized by a waveguide length such as $s \gg N$. In this regime, transmission along the system decreases exponentially [36, 37]. The fluctuation associated with the conductance is so significant that the average conductance inadequately represents the transport properties. Therefore, in order to represent the typical conductance, the most suitable quantity for characterizing transport properties is the logarithm of the conductance, $\mathsf{log}(g)$. Then, after averaging over many configurations, $\mathsf{log}(g)$ decreases linearly as a function of the length of the system,

$$\langle \mathsf{log}(g) \rangle = -2L/\xi, \tag{1.22}$$

with $\xi = Nl$.

In this regime, the conductance distribution $\mathsf{P}(g)$ transitions from a Gaussian distribution typical of the diffusive regime to a log-normal distribution [21, 28]. A numerical example is shown in Fig. 1.8 (a).

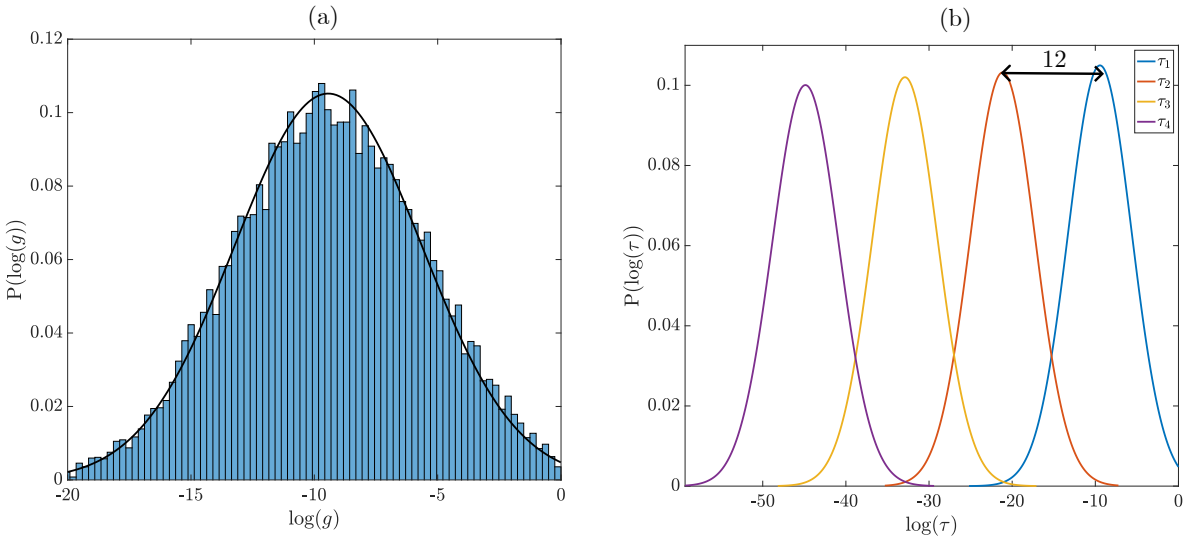

Figure 1.8 – (a) Conductance distribution. (b) TEVs distribution. The distributions are generated from an RMT simulation based on 2.10^4 realizations for $N = 16$ and $s = 76$.

Furthermore, the distribution of the TEVs corresponds to a log-normal distribution [21, 28]. This distribution is spread over a regular grid, where $\mathsf{log}(\tau_{n+1}/\tau_n) = 12$ in the numerical example presented in Fig. 1.8 (b). This regime is also known as a single channel regime since the transmission is dominated by the first TEV τ_1 [7, 16].

1.3.2 Invariance of the transmitted pattern : "freezing"

Let us consider a single configuration of a disordered medium ($s \simeq 34 > N = 16$) placed in an infinite waveguide.

Fig. 1.9 shows the spectrum of the conductance and the five largest TEVs. It shows that the conductance is dominated by the first TEV with a low amplitude, $g \approx \tau_1 \ll 1$. Therefore, the transmission matrix can be approximated by a rank-one matrix

$$\mathsf{T} \approx \sqrt{\tau_1}\boldsymbol{U}_1\boldsymbol{V}_1^\dagger, \tag{1.23}$$

and the transmitted wave is dominated by a single channel, the first TEC, $\boldsymbol{U}_1$, regardless

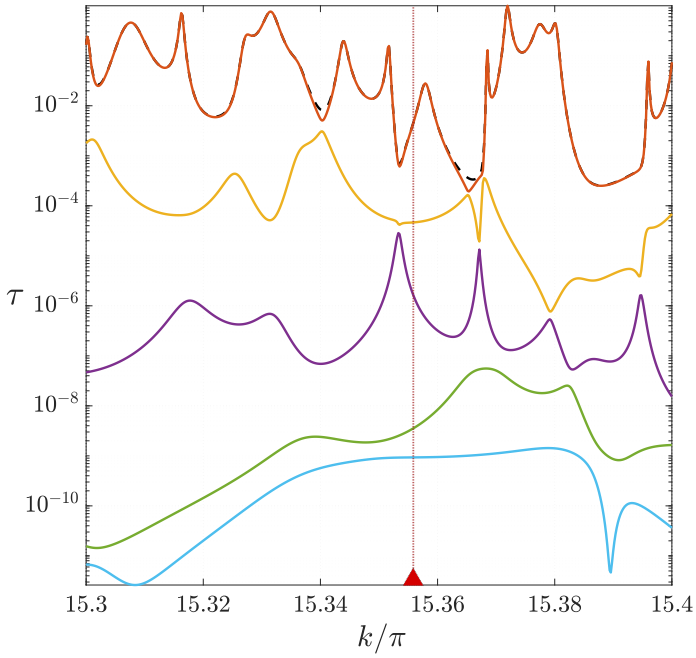

Figure 1.9 – Spectrum of the transmission eigenvalues (solid lines in colors) and conductance (dashed black line) of a disordered sample $s \simeq 34$ placed in an infinite waveguide ($N = 16$). The red triangle represents the frequency of excitation $k/\pi = 15.357$ used to simulate the wavefield in Fig. 1.10.

of changing incident conditions $\boldsymbol{a}^+(0)$

$$\boldsymbol{a}^+(L) \approx b_1 \tau_1 \boldsymbol{U}_1, \text{ with } b_1 = \boldsymbol{V}_1^\dagger \boldsymbol{a}^+(0) \text{ a scalar coefficient.} \tag{1.24}$$

That is, the vector $\boldsymbol{a}^+(L)$ is parallel to $\boldsymbol{U}_1$, and only the amplitude remains dependent on changing $\boldsymbol{a}^+(0)$. "the speckle pattern of the transmitted intensity is literally frozen" [16].

An example of such freezing is shown in Fig. 1.10. The disordered waveguide is excited by 3 different incident waves. The first two are arbitrary (Fig. 1.10 (a) and (b)), and the third one is shaped to match $\boldsymbol{V}_1$ (Fig. 1.10 (c)), associated with the first TEV ($\tau_1 \simeq 0.01$). Comparing the wavefields, we can already observe the strong decrease in amplitude, but above all, the progressive freezing of the wave pattern as we move away from $x = 0$ and a complete freezing of the transmitted pattern. The transmitted pattern corresponds to the pattern of the first transmission eigenchannel. Only the amplitude of the transmitted pattern remains dependent on the incidence conditions.

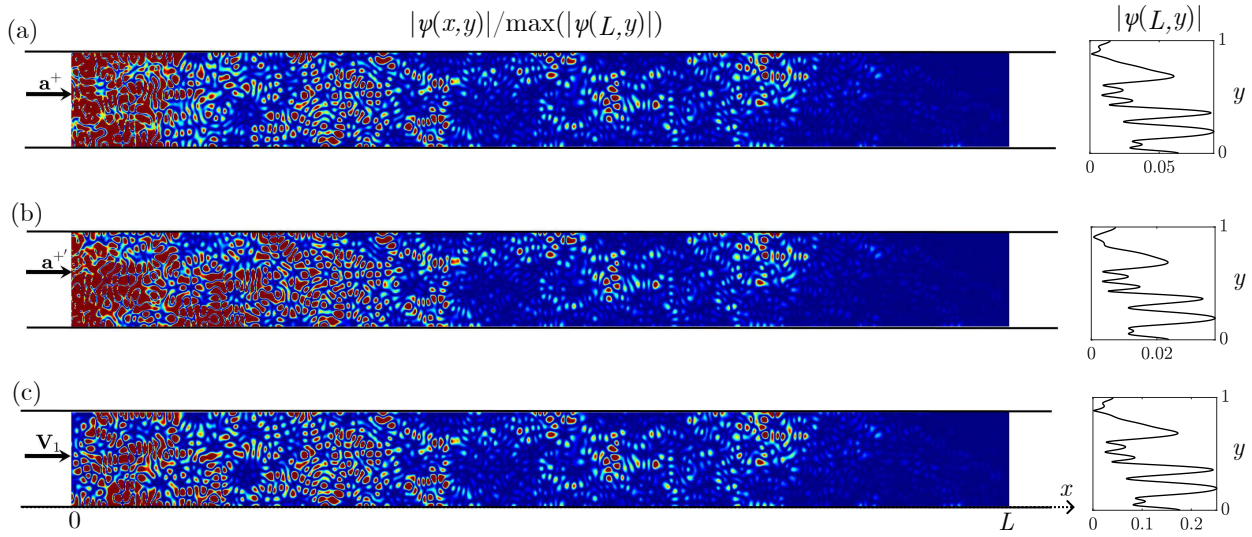

Figure 1.10 – Wavefield modulus in a disordered sample $s \simeq 34$ placed in an infinite waveguide for three different incident waves, at a frequency $k/\pi = 15.357$. (a) and (b) $\boldsymbol{a}^+(0) \equiv (\delta_{n,3})$ and $\mathbf{a}^{+'}(0) \equiv (\delta_{n,15})$. Here, δ represents the Dirac function. (c) For an incident wave shaped to match $\boldsymbol{V}_1$ associated with the largest eigenvalue τ_1. Numerics are performed by using a code developed by Chéron [32].

Another example of such freezing in 2D waveguide geometries has been observed in microwave experiments by Z. Shi [7]. One of their results is shown in Fig. 1.11. It shows the transmitted speckle pattern through a disordered waveguide illuminated by a source at two different positions. They highlight the difference between a diffusive regime, where the transmitted speckle pattern depends strongly on the source position, and a localized regime, where the transmitted speckle pattern is independent of the source position.

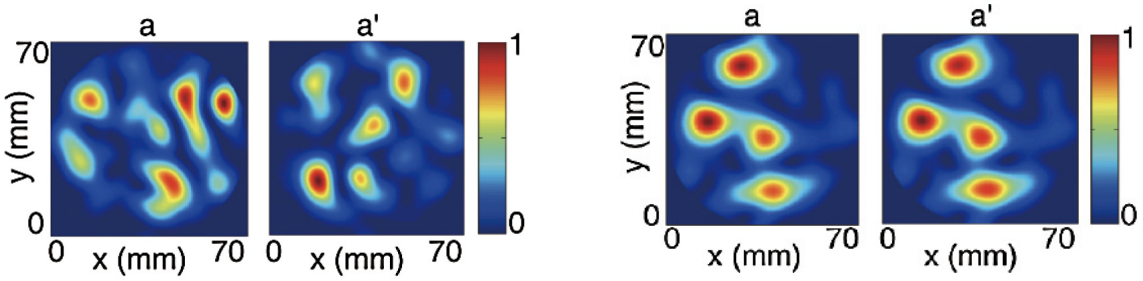

Figure 1.11 – Transmitted speckle patterns through a disordered medium illuminated successively by sources a and a'. The frequency is fixed. Diffusive regime (left row). Localized regime (right row). Source: Z. Shi [7].

The Freezing phenomenon has also been observed numerically for 2D geometries in

a single configuration of an open disordered medium [38]. One of their results is shown in Fig. 1.12. It shows the spatial evolution of the transmitted Intensity through a 2D disordered medium illuminated by a Gaussian beam at two different incident angles, $\theta = 0°$ and $\theta = 30°$. They highlight the difference between a diffusive regime, in which the spatial evolution of the transmitted intensity shows a strong dependence on the incident angle, and a localized regime, which is independent of the incident angle.

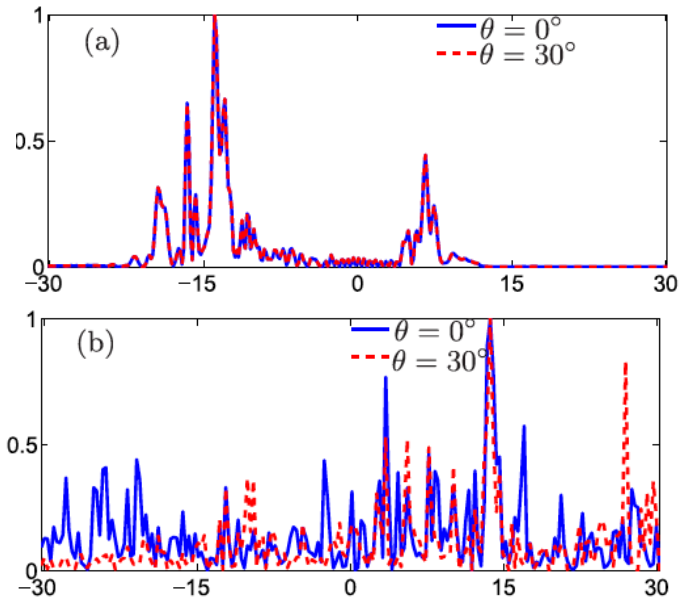

Figure 1.12 – Normalized transmitted intensity versus the normalized transverse direction in the localized regime (a) and in the diffusive regime (b) at normal incidence (solid blue line) and for an incidence angle $\theta = 30°$ (dashed red line). Source: O. Leseur [38].

A large part of this manuscript focuses on the invariance of the transmitted pattern to incidence conditions. We show that this feature is not intrinsically related to the localized regime in disordered media and can be observed in other contexts, in particular in periodic media. In chapters 2 and 3, we show numerically and experimentally that the transmitted pattern through a periodic waveguide can be frozen under proper conditions. In chapter 4, we characterize this phenomenon in the case of transmission through a grating. In Chapter 5, we present numerical observations on the transmission enhancement induced by symmetry when an opaque barrier is placed in a periodic waveguide. Finally, we will conclude this manuscript by presenting preliminary results as perspectives to this work.

APPENDIX

1.A Total scattering matrix of two portions

This section provides the procedures to obtain the total scattering matrix S of two portions of disordered media (Fig. 1.A.1).

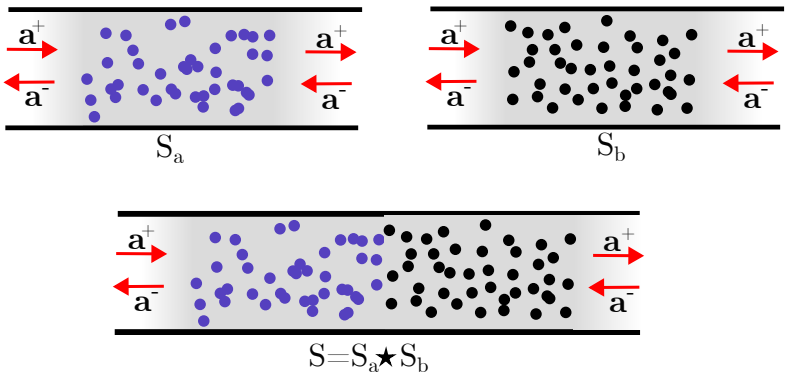

Figure 1.A.1 – Schematic representation of a combination of two portions of disordered media.

Let S_a and S_b be the scattering matrices of the two portions,

$$\mathsf{S}_a = \begin{pmatrix} \mathsf{R}_a & \mathsf{T}'_a \\ \mathsf{T}_a & \mathsf{R}'_a \end{pmatrix},$$
$$\mathsf{S}_b = \begin{pmatrix} \mathsf{R}_b & \mathsf{T}'_b \\ \mathsf{T}_b & \mathsf{R}'_b \end{pmatrix},$$

with $\mathsf{R}_{a,b}$, $\mathsf{R}'_{a,b}$, $\mathsf{T}_{a,b}$, $\mathsf{T}'_{a,b}$ the corresponding reflection and transmission matrices. The reflection (R, R') and the transmission (T, T') matrices corresponding to the total scattering matrix S are given by:

$$\begin{cases} \mathsf{R} = \mathsf{R}_a + \mathsf{T}'_a \left(\mathsf{I} - \mathsf{R}_b \mathsf{R}'_a\right) \mathsf{R}_b \mathsf{T}_a, \\ \mathsf{T} = \mathsf{T}_b \left(\mathsf{I} - \mathsf{R}'_a \mathsf{R}_b\right) \mathsf{T}_a, \\ \mathsf{T}' = \mathsf{T}'_a \left(\mathsf{I} - \mathsf{R}'_a \mathsf{R}_b\right) \mathsf{T}'_b, \\ \mathsf{R}' = \mathsf{R}'_b + \mathsf{T}_b \left(\mathsf{I} - \mathsf{R}_b \mathsf{R}'_a\right) \mathsf{R}'_a \mathsf{T}'_b. \end{cases} \tag{1.25}$$

Chapter 2

Invariance of the transmitted speckle pattern in periodic waveguides

In this chapter, we report on conditions of invariance of the transmitted speckle pattern with the incidence condition in the propagation through a periodic waveguide. This phenomenon is reminiscent to that observed when illuminating a disordered medium in the regime of Anderson localization, as a consequence of the contribution of a single transmission eigenchannel to the transmitted wave. The freezing of the transmitted wave is not intrinsically related to disorder, and it can also be observed in a regular, periodic system, provided that at most one Bloch mode is propagating. Moreover, while all localized modes in a disordered medium are exponentially decaying, a periodic waveguide makes it possible to observe the freezing of a propagating wave, hence without the counterpart of having a very low energy transmission.

2.1 Introduction

Among the many striking wave phenomena that arise in disordered media and explain undiminished interest in the field of wave physics over decades [2, 4, 8, 28], the single channel regime, although not the most famous, is nevertheless quite remarkable. Since the ratio between two successive transmission eigenvalues (TEVs) is large in the localized regime, the first (largest) one dominates all others, and so does the corresponding eigenchannel in the transmission problem. A consequence is that "*the speckle pattern of the transmitted intensity is literally frozen*" [16], that is, at a given frequency, the speckle pattern is independent of the incidence conditions. The single channel regime was experimentally evidenced with microwaves [7, 39, 40] and later numerically investigated in optics in a two-dimensional medium, and used to probe Anderson localization in a single configuration of the medium [38]. Among the situations where TEVs are insightful, this insensitivity to incidence conditions in the localized regime is very particular: indeed, in most cases, TEVs are used for wavefront shaping, which reflects the capability of using the sensitivity to incident wave in the diffusive regime to control the transmitted field [33–35, 41–43].

Let us consider the typical scattering problem of a L-length disordered waveguide that connects two semi-infinite leads, see Fig. 2.1(a). The wave incident on the disordered medium, as well as the resulting scattered waves in the leads, are decomposed over the set of $2N$, right- and left-going, propagating modes, and the transmission matrix T couples the transmitted wave components to those of the incident wave. Using the singular value decomposition, this matrix is written as the sum of rank one matrices: $\mathsf{T} = \sum_{n=1}^{N} \sqrt{\tau_n}\, \boldsymbol{U}_n \boldsymbol{V}_n^\dagger$, where τ_n are the TEVs and where the unit vectors $\boldsymbol{U}_n$ (resp. $\boldsymbol{V}_n$) map the output (resp. input) field of the transmission eigenchannels to the leads propagating modes. In the localized regime, $1 \gg \tau_1 \gg \tau_2 \gg \tau_3 \gg \dots$ [27, 44, 45], thus $\mathsf{T} \approx \sqrt{\tau_1}\, \boldsymbol{U}_1 \boldsymbol{V}_1^\dagger$ following a single-channel behavior and, whatever the incident field, the pattern at the output will be that of the mode combination $\boldsymbol{U}_1$.

Although the single-channel phenomenon is understood as being characteristic of the localized transport, the medium-induced reduction of the transmission problem to a rank-1 matrix is not intrinsically related to disorder and can be observed in other contexts, in particular in regular media. A simple example of a single channel regime would be the low-frequency propagation (*i.e.*, at most one mode is propagating) in a uniform waveguide segment connecting two leads: inside the waveguide, in the far-field from inlet and outlet,

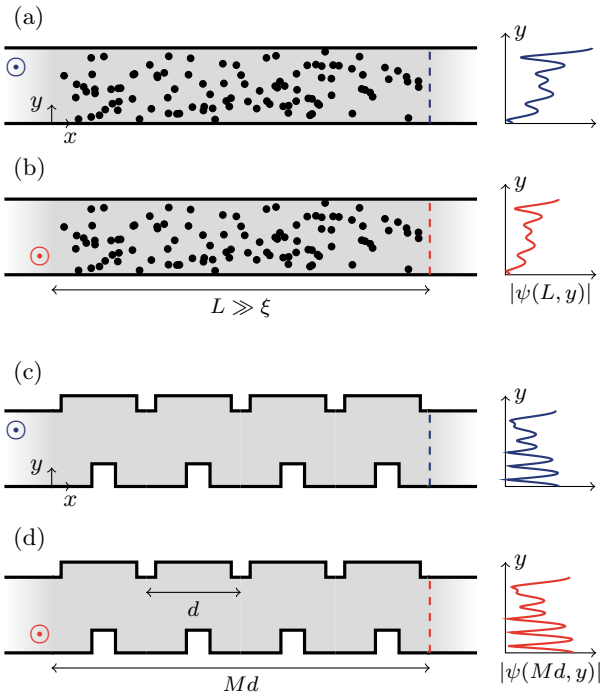

Figure 2.1 – Invariance of the transmitted speckle pattern. (a-b) In a disordered waveguide, which length L is larger than the localization length ξ, only one eigenchannel contributes to transmission, giving then the transmitted field its spatial pattern, regardless of the incident wave (here generated by a source $\odot$ at two different positions in the waveguide) [7, 38]. (c-d) A similar phenomenon can be observed with waves traveling through a periodic waveguide, in which at most one pair of right- and left-going Bloch modes is propagating, while all others are evanescent.

it reduces to a single mode. This mode then gives the field its transverse shape and the transmitted field pattern is consequently invariant with the incident wave. However, in this simple example, when saying "single mode" one actually speaks of the linear combination of two modes, a right-going and a left-going: $a\phi(y)e^{\mathrm{i}\kappa x} + b\phi(y)e^{-\mathrm{i}\kappa x}$, and it is only because both have the same transverse structure $\phi(y)$ that the total field is separable in the variables x and y and that one can directly link this pattern to that of the transmitted field. Would the structure of the left-going mode be different from that of the right-going mode, then different linear combinations of them will not produce an invariant pattern. Indeed, in a periodic waveguide as illustrated in Fig. 2.1(c-d), the linear combination of a pair of right- and left-going Bloch modes reads $a\phi^+(x, y)e^{\mathrm{i}qx} + b\phi^-(x, y)e^{-\mathrm{i}qx}$. Then, due to the form of the Bloch eigenvalue problem, ϕ^+ and ϕ^- are complex-conjugated one to the other under proper normalization; $\phi^- = \bar{\phi}^+$ being not proportional to ϕ^+, there

is no separation in the variables x and y in the total field. Consequently, as shown in Fig. 2.2, different linear combinations of these right- and left-going Bloch modes will give rise to different patterns, both at the input and output of the unit cell. Thus, making the single-mode propagation (actually a single pair) a direct analog to the single-channel regime can be misleading, or at least insufficient to conclude that the transmitted pattern will be *frozen*.

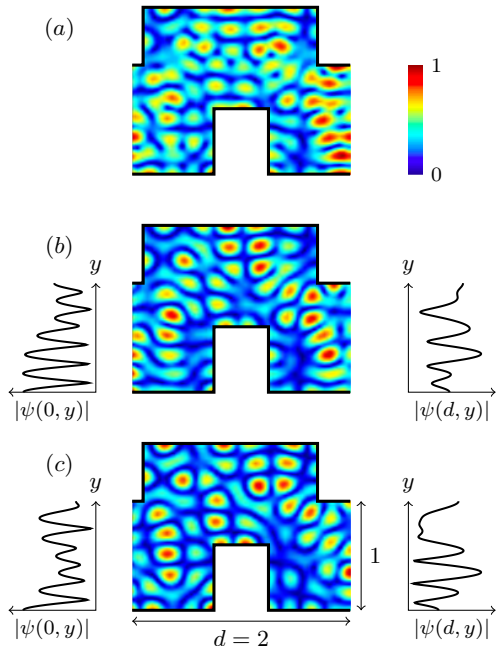

Figure 2.2 – (a) Unit cell of a periodic waveguide as studied in this paper and, at frequency $k = 6.23\pi$, amplitude of the only propagating right-going Bloch mode, ϕ_+ [see the dispersion relation in Fig. 2.3(b)]. The corresponding left-going mode, ϕ_-, is the complex conjugate of ϕ_+. (b-c) Two different linear combinations of the Bloch modes $\phi_\pm$ with, at the input and output ends of the unit cell, the corresponding transverse profile

In this paper, we show that periodic waveguides can actually produce a freezing of the transmitted pattern under proper frequency conditions and we prove algebraically the reduction of the transmission matrix to a rank-1 matrix taking into account right- and left-going waves through a scalar form factor D.

2.2 Periodic waveguides and freezing conditions

To do this, we consider a finite, d-periodic, waveguide [Fig. 2.1(c-d)] and numerically solve the propagation problem when a source ($\odot$) is placed in the left lead at various

positions to change the incident field. As in the above-mentioned disordered case, we assume that the semi-infinite leads at the left ($x \leq 0$) and right ($x \geq Md$) of the M-cell scattering region supports $2N$ right- and left-going propagating modes. Denoting $g_n(y)$, $n = 1, \ldots, N$, the associated transverse eigenfunctions, the solution of the wave equation $(\Delta + k^2)\psi(x, y) = 0$ at both ends of the scattering region is

$$\psi(0, y) = \boldsymbol{g}^{\mathsf{T}}(y) \left(\boldsymbol{a}^{+}(0) + \boldsymbol{a}^{-}(0) \right) + \psi_{\mathrm{l}}^{(\mathrm{e})}(y), \tag{2.1}$$

$$\psi(Md, y) = \boldsymbol{g}^{\mathsf{T}}(y) \left(\boldsymbol{a}^{+}(Md) + \boldsymbol{a}^{-}(Md) \right) + \psi_{\mathrm{r}}^{(\mathrm{e})}(y), \tag{2.2}$$

where $\boldsymbol{g} \equiv (g_n)$, $\boldsymbol{a}^{+}$ (resp. $\boldsymbol{a}^{-}$) is the vector of the modal coefficient of the right- (resp. left-) going propagating wave, and $\psi_{\mathrm{l,r}}^{(\mathrm{e})}(y)$ denotes the evanescent fields at $x = 0$ and Md. With a source located in the left lead ($x < 0$), $\boldsymbol{a}^{-}(Md) = 0$ and $\boldsymbol{a}^{+}(Md) = \mathsf{T}\boldsymbol{a}^{+}(0)$. Fig. 2.3(a) shows the variations of the three largest TEVs, $\tau_1 > \tau_2 > \tau_3$ with the frequency k, in a range where $N = 7$. Following the reasoning stated in the case of disordered media,

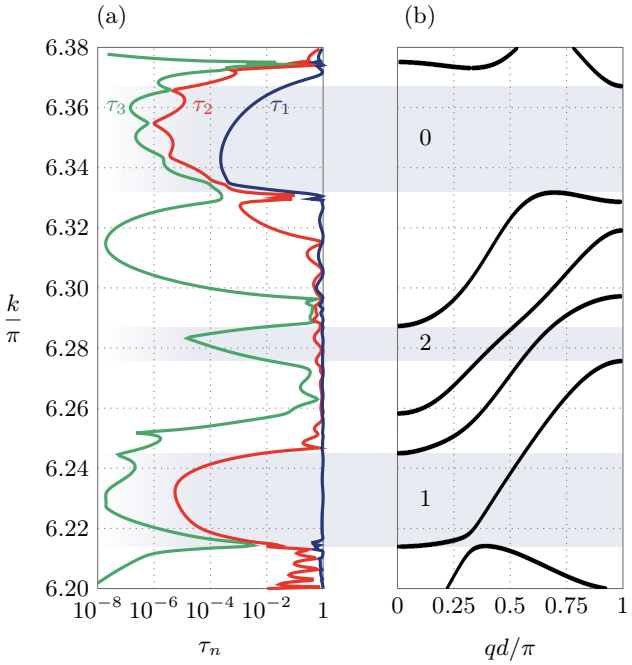

Figure 2.3 – (a) Spectrum of the first three TEVs $\tau_1 > \tau_2 > \tau_3$ of a 10-cell finite periodic waveguide ($M = 10$, $d = 2$), in the frequency range $k/\pi \in [6.20, 6.38]$. (b) Dispersion relation of the equivalent infinite periodic waveguide in the same range of frequency. The numbers in the right plot are the number of pair of right- and left-going propagating Bloch modes in the corresponding colored frequency interval. Numerics are performed using a mode-matching method (see App. 2.A for more details on the calculations).

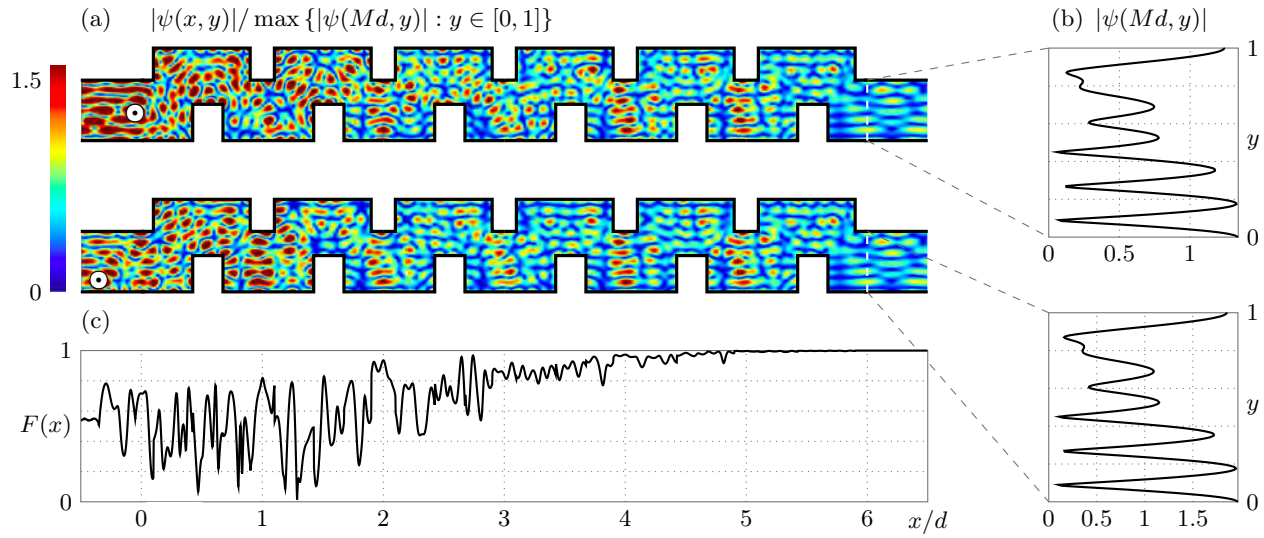

Figure 2.4 – (a) Wavefield (modulus) in a finite periodic waveguide ($M = 6$, $d = 2$), as generated by a point source located at two different positions ($\odot$), at a frequency, $k = 6.23\pi$, in a band with only one pair of right- and left-going propagating Bloch modes (see. Fig. 2.3). (b) Pattern of the transmitted field $|\psi(x = Md, y)|$, $y \in [0, 1]$. (c) Similarity function $F(x)$, as defined by Eq. (2.3). Numerics are performed using a finite element method (Comsol Multiphysics).

we can expect a freezing of the transmitted pattern if $\tau_1 \gg \tau_2$.

This condition is notably fulfilled in a frequency range around $k = 6.23\pi$, and the transmission through a 6-cell finite periodic waveguide at this frequency is illustrated in Fig. 2.4(a) with two examples, corresponding to two different positions of the point source generating the wavefield. While the excitation, hence the incident wave, is modified from one case to the other, no significant change in the transmitted field pattern can be detected, see Fig. 2.4(b). Only the overall amplitude of the transmitted wave remains dependent on the incidence conditions. Computing the wavefield in the whole waveguide allows us to go further than the only analysis of the transmitted pattern. We can indeed observe the progressive freezing of the wave pattern as we move away from the source. This can be quantified with the similarity function

$$F(x) = \frac{\int_0^1 \psi(x,y)\bar{\psi}'(x,y)\,\mathrm{d}y}{\sqrt{\int_0^1 |\psi(x,y)|^2\,\mathrm{d}y \int_0^1 |\psi'(x,y)|^2\,\mathrm{d}y}}, \tag{2.3}$$

which is a normalized scalar product ($0 \leq F \leq 1$) measuring the proportionality between the fields ψ and ψ' obtained with two different positions of the source. First low-valued

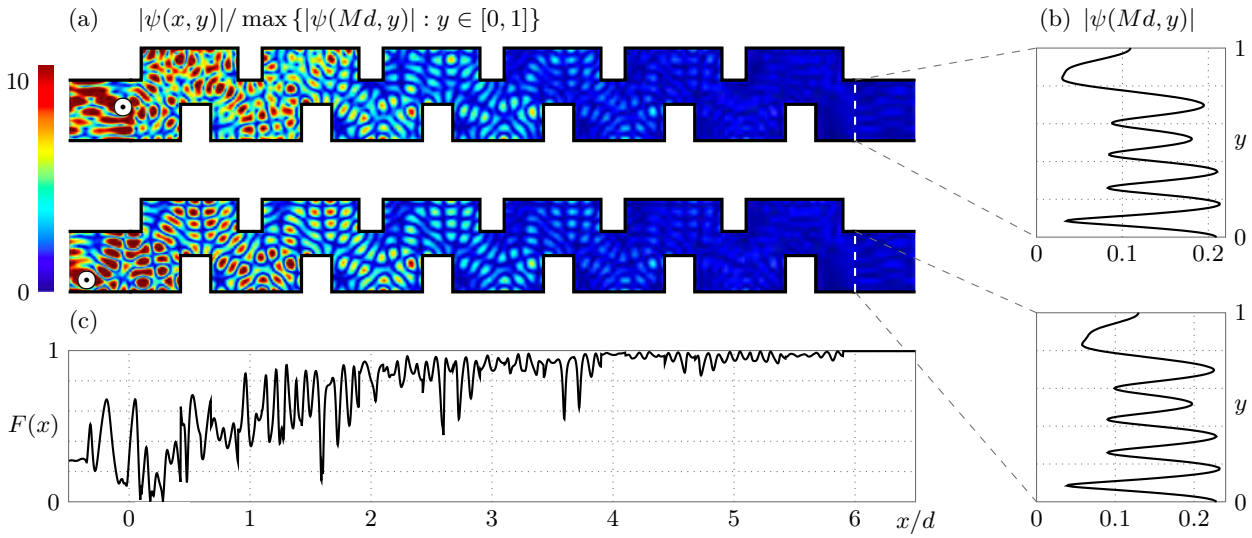

Figure 2.5 – (a) Wavefield (modulus) in a finite periodic waveguide ($M = 6$, $d = 2$), as generated by a point source located at two different positions ($\odot$), at a frequency, $k = 6.353\pi$, in a bandgap (see. Fig. 2.3). (b) Pattern of the transmitted field $|\psi(x = Md, y)|$, $y \in [0, 1]$. (c) Similarity function $F(x)$, as defined by Eq. (2.3). Numerics are performed using a finite element method (Comsol Multiphysics).

close to the source [Fig. 2.4(c)], $F(x)$ progressively increases towards 1, characterizing two similar patterns.

Another frequency range in which the condition $\tau_1 \gg \tau_2$ is satisfied is around $k = 6.35\pi$, see Fig. 2.3(a). As shown in Fig. 2.5, choosing different positions of the point source, we also observe, in this case, the freezing of the transmitted pattern [Fig. 2.5(b)]. Also, as in the preceding case, the evolution of the similarity function $F(x)$ reveals how the freezing of the wavefield is completed after 3 or 4 periods.

Figs. 2.4-2.5, though both show the invariance of the transmitted field pattern with the incidence conditions, display nevertheless visible differences that can be interpreted by analysis of the dispersion relation, see Fig. 2.3(b). Indeed, while the first frequency chosen, $k = 6.23\pi$, lies in a band where one pair of Bloch modes are propagating, the second frequency, $k = 6.353\pi$, lies in a bandgap. It follows that the wavefield amplitude is exponentially decreasing in this last case, whereas the wave is well transmitted through the waveguide in the first case. In this respect, this physical system differs significantly from an Anderson-localized medium in that it allows the field to be frozen while preserving a high transmission. Note that in the bandgap case, it would be possible to optimize the transmission by spatially shaping the incident wave [46].

The occurrence of bands with one or zero pair of propagating Bloch modes that are wide enough to observe the freezing on a reasonable - not too long - distance is, of course, highly dependent on the cell geometry. Targeting frequencies, or frequency intervals, at which the freezing occurs, would be possible by, *e.g.*, optimization processes, but even without this, configurations allowing for a broadband freezing can easily be found, as illustrated in the App. 2.B.

2.3 Algebric analysis

The two examples in Figs. 2.4-2.5 show how the freezing phenomenon appears as a consequence of the number of propagating Bloch modes, which itself correlates with the hierarchy of the first TEVs, as illustrated by Fig. 2.3. This can be further elucidated by a simple algebraic analysis of the scattering problem. The transmission matrix of the M-cell system reads

$$\mathsf{T} = \mathsf{T}^{(\mathrm{r})} \left(\mathbb{1} - \mathsf{\Lambda}^M \mathsf{R}^{(\mathrm{l})\prime} \mathsf{\Lambda}^M \mathsf{R}^{(\mathrm{r})} \right)^{-1} \mathsf{\Lambda}^M \mathsf{T}^{(\mathrm{l})}, \tag{2.4}$$

where $\mathsf{\Lambda}$ is the diagonal matrix of the eigenvalues of Bloch eigenvalues associated to the right-going modes and $\mathsf{T}^{(\mathrm{l})}$, $\mathsf{R}^{(\mathrm{r})}$, $\mathsf{R}^{(\mathrm{l})\prime}$ and $\mathsf{T}^{(\mathrm{r})}$ are elements of the scattering matrices of the left and right interfaces, mapping the Bloch modes to the lead propagating modes (see App. 2.C). The inverted matrix term in Eq. (2.24) accounts for the multiple internal reflections that the wave experiences before it is transmitted to the right lead. If, after possibly being reordered, the Bloch eigenvalues are such that the first one, Λ_1, is large compared with all others, then T can be approximated by the rank one matrix

$$\mathsf{T} \approx \tilde{\mathsf{T}} = \frac{\Lambda_1^M}{1 - \Lambda_1^{2M} \mathsf{R}_{11}^{(\mathrm{l})\prime} \mathsf{R}_{11}^{(\mathrm{r})}} \boldsymbol{T}_1^{(\mathrm{r})} \boldsymbol{T}_1^{(\mathrm{l})\mathsf{T}}, \tag{2.5}$$

with $\boldsymbol{T}_1^{(\mathrm{r})}$ (resp. $\boldsymbol{T}_1^{(\mathrm{l})\mathsf{T}}$) the first column (resp. row) of the transmission matrix of the right (resp. left) interface at $x = 0$ (resp. L, see App. 2.D). $\mathsf{R}_{11}^{(\mathrm{l})\prime}$ and $\mathsf{R}_{11}^{(\mathrm{r})}$ are reflection coefficients of the first mode at these interfaces. Thus, as soon as one pair of Bloch modes, whether propagating or evanescent, predominantly contributes to the solution in the periodic waveguide, with all others being rapidly damped ($|\Lambda_1^M| \gg |\Lambda_{n\geq 2}^M|$), then the pattern of the transmitted field $\boldsymbol{a}^+(Md) \approx \tilde{\mathsf{T}} \boldsymbol{a}^+(0)$ no longer depends on the incident wave $\boldsymbol{a}^+(0)$. Indeed, from Eq. (2.5), $\tilde{\mathsf{T}} \boldsymbol{a}^+(0) = D(\boldsymbol{T}_1^{(\mathrm{l})\mathsf{T}} \boldsymbol{a}^+(0)) \boldsymbol{T}_1^{(\mathrm{r})}$ is collinear with $\boldsymbol{T}_1^{(\mathrm{r})}$, whatever $\boldsymbol{a}^+(0)$, where $D = \Lambda_1^M / (1 - \Lambda_1^{2M} \mathsf{R}_{11}^{(\mathrm{l})\prime} \mathsf{R}_{11}^{(\mathrm{r})})$ is the form factor due to multiple

internal reflections in the periodic slab. Only the amplitude in front of the transmitted vector $\boldsymbol{T}_1^{(\mathrm{r})}$, through the product $\boldsymbol{T}_1^{(\mathrm{l})\mathsf{T}}\boldsymbol{a}^+(0)$, can still vary with the incident wave.

2.4 Wavefront shaping

Suppose, now, that two right-going Bloch modes are propagating in the periodic waveguide (an example of such a band is given in Fig. 2.3 near $k = 6.28\pi$). Then,

$$\boldsymbol{a}^+(Md) \approx (\boldsymbol{T}_1^{(\mathrm{l})\mathsf{T}}\boldsymbol{a}^+(0))\boldsymbol{u}_1 + (\boldsymbol{T}_2^{(\mathrm{l})\mathsf{T}}\boldsymbol{a}^+(0))\boldsymbol{u}_2 \tag{2.6}$$

where $\boldsymbol{u}_{1,2}$ are linear combinations of the first two columns of $\mathsf{T}^{(\mathrm{r})}$ (see App. 2.D) and $\boldsymbol{T}_1^{(\mathrm{l})\mathsf{T}}$ and $\boldsymbol{T}_2^{(\mathrm{l})\mathsf{T}}$ are the first two rows of $\mathsf{T}^{(\mathrm{l})}$. The transmitted field then reads as a linear combinations of $\boldsymbol{u}_1$ and $\boldsymbol{u}_2$ and its pattern will thus depend on the incident wave $\boldsymbol{a}^+(0)$. However, the transmission problem being now reduced to a rank-2 matrix, a freezing phenomenon can still be observed. Note that the coefficient of $\boldsymbol{u}_1$ (resp. $\boldsymbol{u}_2$) in Eq. (2.6) is the first (resp. second) component of $\mathsf{T}^{(\mathrm{l})}\boldsymbol{a}^+(0)$, that is, the amplitude with which the incident wave, when transmitted through the left interface, couples to the first (resp. second) propagating right-going Bloch mode. Therefore, any incident wave that does not couple to the first (resp. second) propagating right-going Bloch mode will give rise to a transmitted wave, the pattern of which is that of $\boldsymbol{u}_2$ (resp. $\boldsymbol{u}_1$). Fig. 2.6 illustrates this partial invariance of the transmitted field. Cases (a) and (b) show the wavefield for two different incident waves (left subplots), none of which couple to the first incident Bloch mode. The transmitted fields (right subplots), therefore, have an identical pattern. Now (c-d), if one choose two other incident waves, none of which couple to the second propagating Bloch mode, then the transmitted field also displays an invariant pattern, but which differs from that of the first two cases.

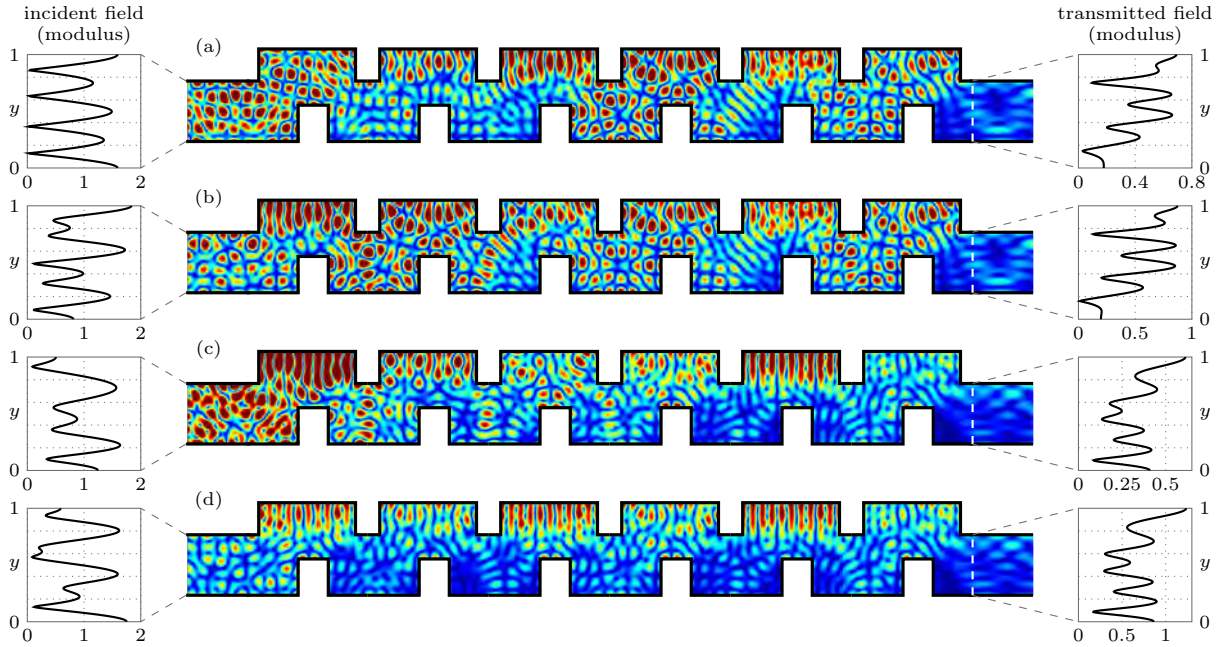

Figure 2.6 – Wavefield (modulus) in a finite periodic waveguide ($M = 6$, $d = 2$) at a frequency, $k = 6.284\pi$, in a band with two right-going propagating Bloch modes, see Fig. 2.3. (a-b) Fields resulting from two different incident waves in the left lead, none of which couples to the first right-going propagating Bloch mode in the periodic region. (c-d) Fields resulting from two different incident waves in the left lead, none of which couples to the second right-going propagating Bloch mode in the periodic region. Numerics are performed using a mode-matching method (see App. 2.A for more details on the calculations).

2.5 Conclusion

In conclusion, we have shown that the propagation through a periodic waveguide may result in the invariance of the transmitted speckle pattern with the incident wave. This property, that is usually observed in Anderson-localized disordered media, is here in contrast appearing due to the periodicity of the medium, as a consequence of the single-channel regime with a dominating transmission eigenvalue. The insensitivity to incidence condition is observed if at most one pair of right- and left-going Bloch modes is propagating in the finite periodic waveguide. This condition for freezing makes the periodic case significantly different from the disordered case in that it allows a non-weak transmission when the dominating mode is propagating. This should make it easier to experimentally evidence and characterize the transmission invariance.

APPENDIX

2.A Mode matching method

In addition to finite elements computations (performed with Comsol Multiphysics), a mode matching method is used in the paper to compute the dispersion relation of the periodic waveguide (Fig. 2 of the paper), as well as the scattering matrix and wavefield in the case of a M-cell finite periodic configuration (Fig. 5).

2.A.1 Dispersion relation

In order to get the dispersion relation, the first step is the calculation of the scattering matrix of a unit cell (Fig. 2.A.1). The cell is a piecewise constant waveguide element,

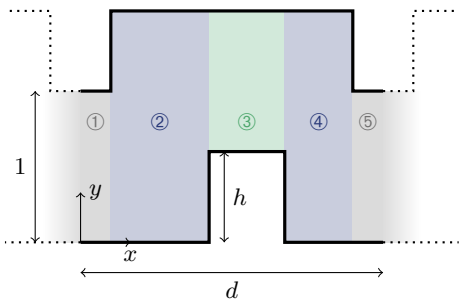

Figure 2.A.1 – Unit cell.

composed of five discontinuously connected segments with length $l^{(j)}$ and width $h^{(j)}$, $1 \leq j \leq 5$ (note that $l^{(5)} = l^{(1)}$, $h^{(5)} = h^{(1)} = 1$, $h^{(4)} = h^{(2)}$ and $h^{(3)} = h^{(2)} - th$). In each segment, a multimodal formulation of the wavefield is given as

$$\psi^{(j)}(x, y) = \boldsymbol{g}^{(j)\mathsf{T}}(y)(\boldsymbol{b}^{(j)+}(x) + \boldsymbol{b}^{(j)-}(x)), \tag{2.7}$$

with $\boldsymbol{b}^{(j)+}$ (resp. $\boldsymbol{b}^{(j)-}$) the vector of the modal coefficient of the right- (resp. left-) going wave and $\boldsymbol{g}^{(j)}$ the vector of the transverse eigenfunctions. Assuming Neumann conditions at the waveguide boundaries, as it is done in the numerics shown in Figs. 1-5 of the paper,

these eigenfunctions are

$$g_n^{(1)}(y) = g_n^{(5)}(y) = \sqrt{\epsilon_n}\cos(\gamma_n^{(1)}y), \tag{2.8a}$$

$$g_n^{(2)}(y) = g_n^{(4)}(y) = \sqrt{\epsilon_n/h^{(2)}}\cos(\gamma_n^{(2)}y), \tag{2.8b}$$

$$g_n^{(3)}(y) = \sqrt{\epsilon_n/h^{(3)}}\cos(\gamma_n^{(3)}(y-th)), \tag{2.8c}$$

with $\epsilon_0 = 1$ and $\epsilon_{n>0} = 2$ and $\gamma_n^{(j)} = n\pi/h^{(j)}$. The transmission matrix of each segment simply reads $\mathsf{T}^{(j)} = \exp(\mathsf{Y}_{\mathrm{c}}^{(j)}l^{(j)})$, with $\mathsf{Y}_{\mathrm{c}}^{(j)}$ the diagonal characteristic admittance matrix of the segment, given by $\mathsf{Y}_{\mathrm{c}n}^{(j)} = \mathrm{i}(k^2-\gamma_n^{(j)})^{1/2}$. The scattering matrix is then

$$\mathsf{S}^{(j)} = \begin{pmatrix} \mathbb{0} & \mathsf{T}^{(j)} \\ \mathsf{T}^{(j)} & \mathbb{0} \end{pmatrix}, \tag{2.9}$$

since no reflection occurs in the uniform segments. The scattering actually occurs at the discontinuous junctions and one accounts for it by rigorously writing the mode matching that results from the continuity conditions. Consider for example the junction between the segments ① and ②. Writing the continuity of the wavefield and of its x-derivative, as well as the Neumann condition on the upper vertical boundary, leads to (the values of $\boldsymbol{b}^{(1,2)\pm}$ below are taken at the junction abscissa)

$$\boldsymbol{b}^{(1)+} + \boldsymbol{b}^{(1)-} = \mathsf{F}(\boldsymbol{b}^{(2)+} + \boldsymbol{b}^{(2)-}), \tag{2.10a}$$

$$\mathsf{F}^{\mathsf{T}}\mathsf{Y}_{\mathrm{c}}^{(1)}(\boldsymbol{b}^{(1)+} - \boldsymbol{b}^{(1)-}) = \mathsf{Y}_{\mathrm{c}}^{(2)}(\boldsymbol{b}^{(2)+} - \boldsymbol{b}^{(2)-}), \tag{2.10b}$$

with F the mode-matching matrix:

$$\mathsf{F}_{mn} = \int_0^1 g_m^{(1)}(y)g_n^{(2)}(y)\,\mathrm{d}y. \tag{2.11}$$

One deduces that the S-matrix of the junction (1-2) is

$$\mathsf{S}^{(1-2)} = \begin{pmatrix} \mathbb{1} & -\mathsf{F} \\ \mathsf{F}^{\mathsf{T}}\mathsf{Y}_{\mathrm{c}}^{(1)} & \mathsf{Y}_{\mathrm{c}}^{(2)} \end{pmatrix}^{-1} \begin{pmatrix} -\mathbb{1} & \mathsf{F} \\ \mathsf{F}^{\mathsf{T}}\mathsf{Y}_{\mathrm{c}}^{(1)} & \mathsf{Y}_{\mathrm{c}}^{(2)} \end{pmatrix}. \tag{2.12}$$

Once the other junction-S-matrices obtained similarly, the scattering matrix of the whole unit cell can be computed by using iteratively the composition product, often referred to

as the Redheffer star-product [31]:

$$\mathsf{S} = \mathsf{S}^{(1)} \star \mathsf{S}^{(1-2)} \star \mathsf{S}^{(2)} \star \ldots \star \mathsf{S}^{(4-5)} \star \mathsf{S}^{(5)}. \tag{2.13}$$

Thus, taking $x = 0$ as the position of the left end of the cell,

$$\begin{pmatrix} \boldsymbol{b}^{(1)-}(0) \\ \boldsymbol{b}^{(5)+}(d) \end{pmatrix} = \mathsf{S} \begin{pmatrix} \boldsymbol{b}^{(1)+}(0) \\ \boldsymbol{b}^{(5)-}(d) \end{pmatrix} \tag{2.14}$$

Assuming now a periodic waveguide, the modal components above also fulfill the pseudo-periodic condition

$$\begin{cases} \boldsymbol{b}^{(5)+}(d) = e^{\mathrm{i}qd} \boldsymbol{b}^{(1)+}(0), \\ \boldsymbol{b}^{(5)-}(d) = e^{\mathrm{i}qd} \boldsymbol{b}^{(1)-}(0). \end{cases} \tag{2.15}$$

Then, writing S as

$$\mathsf{S} = \begin{pmatrix} \mathsf{R} & \mathsf{T}' \\ \mathsf{T} & \mathsf{R}' \end{pmatrix}, \tag{2.16}$$

the dispersion relation of the periodic waveguide can be obtained as the solutions (q, k) of

$$\det \left[\begin{pmatrix} \mathsf{T} & \mathsf{R}' \\ \mathbb{0} & \mathbb{1} \end{pmatrix} - e^{\mathrm{i}qd} \begin{pmatrix} \mathbb{1} & \mathbb{0} \\ \mathsf{R} & \mathsf{T}' \end{pmatrix} \right] = 0. \tag{2.17}$$

2.A.2 Wavefield

Consider, now, that the waveguide is composed of M cells, that is, of $5M$ waveguide segments as defined above. Labeling these segments from 1 to $5M$ and denoting $x^{(j)}$ the abscissa of their left end and $l^{(j)}$ their length, then the modal solutions in Eq. (4.14) are

$$\boldsymbol{b}^{(j)+}(x) = e^{\mathsf{Y}_{\mathrm{c}}^{(j)}(x - x^{(j)})} \boldsymbol{\mathcal{A}}^{(j)}, \tag{2.18a}$$

$$\boldsymbol{b}^{(j)-}(x) = e^{\mathsf{Y}_{\mathrm{c}}^{(j)}(x^{(j+1)} - x)} \mathcal{R}^{(j)} e^{\mathsf{Y}_{\mathrm{c}}^{(j)} l^{(j)}} \boldsymbol{\mathcal{A}}^{(j)}, \tag{2.18b}$$

where $\boldsymbol{\mathcal{A}}^{(j)}$ is the value of the right-going wave at the input end of the jth segment, and $\mathcal{R}^{(j)}$ is the reflection matrix at the output end: $\boldsymbol{b}^{(j)-}(x^{(j+1)}) = \mathcal{R}^{(j)} \boldsymbol{b}^{(j)-}(x^{(j+1)})$. Its value at the right-end of the M-cell waveguide is known: $\mathcal{R}^{(5M)} = \mathbb{0}$, since the waveguide ends in a semi-infinite lead, and it can be calculated iteratively in the other segments, using the continuity relations (4.18) [47]. Then, in a second step, the values $\boldsymbol{\mathcal{A}}^{(j)}$ can be obtained

iteratively from the known value $\boldsymbol{\mathcal{A}}^{(1)}$ - the incident field coming from the left lead.

2.A.3 Dimensions of the unit cell in the numerics

For both FEM and mode-matching computations shown in Figs. 2-5 of the paper, the dimensions of the unit cell are $d = 2$, $(l^{(1)}, l^{(2)}, l^{(3)}) = (0.1d, 0.365d, 0.25d)$, $h = 0.6$, and $h^{(2)} = 1.53$.

2.B Broadband "freezing"

In this section, we aim at finding a waveguide geometry that induces a freezing of the transmitted wave pattern over a broad frequency range by adjusting the height th, see Fig. 2.A.1. For the sake of simplicity, we restrict to geometries such that $h^{(2)} = 1 + th$,

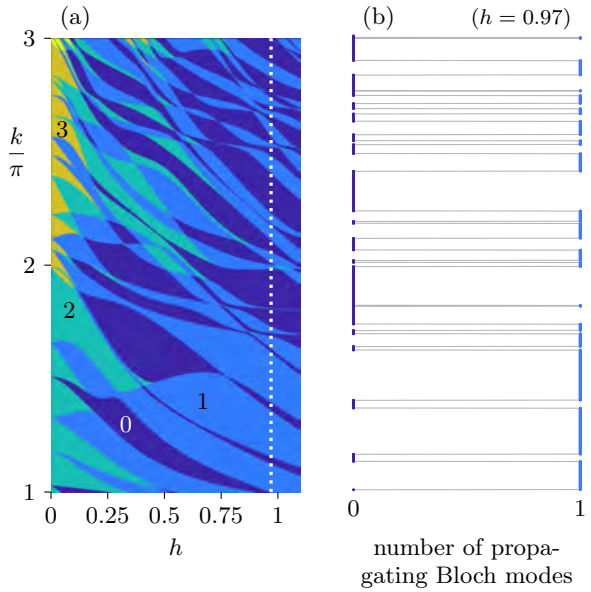

Figure 2.B.1 – (a) Number of propagating Bloch modes as a function of th (see Fig. 2.A.1) and of the frequency. The dimensions of cell are $d = 1.5$, $(l^{(1)}, l^{(2)}, l^{(3)}) = (0.1d, 0.365d, 0.25d)$, $h^{(2)} = 1 + th$. (b) Number of propagating Bloch modes as a function of the frequency, for $th = 0.97$ (the corresponding value of th is shown with a white dotted line in the left plot).

and we choose $d = 1.5$.

Fig. 2.B.1(a) shows the number of propagating Bloch modes in an infinite periodic waveguide, when varying th, in the frequency range $k/\pi \in [1, 3]$.

The occurence of frequency intervals with more that one propagating Bloch modes reduces when increasing th and, for, *e.g.*, $th = 0.97$, at most one Bloch mode can propagate over the considered range, see also Fig. 2.B.1(b). Therefore, we expect that, after being transmitted through a sufficient number of periods of this specific waveguide geometry, the field displays a "frozen" pattern, independent of the incident wave, over the whole frequency range. Fig. 2.B.2 shows that it is indeed the case.

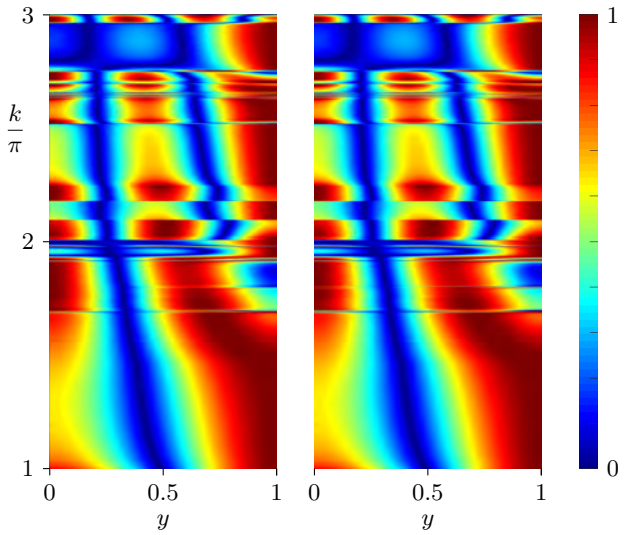

Figure 2.B.2 – Pattern of the transmitted field $|\psi(Md), y|$ over the frequency range $k \in [\pi, 3\pi]$, for two different incident waves. The waveguide is made of $M = 10$ cells with dimensions given Fig. 2.B.1's caption and $th = 0.97$. At each frequency, the amplitude is normalized so that its maximum value is 1 to facilitate pattern comparison.

2.C Transmission matrix of the finite M-cell periodic waveguide

Let H_c be the transfer matrix of a single cell (Fig. 2.A.1):

$$\begin{pmatrix} \boldsymbol{a}^+(d) \\ \boldsymbol{a}^-(d) \end{pmatrix} = \mathsf{H}_\mathrm{c} \begin{pmatrix} \boldsymbol{a}^+(0) \\ \boldsymbol{a}^-(0) \end{pmatrix}; \tag{2.19}$$

its eigendecomposition

$$\mathsf{H}_\mathrm{c} = \mathsf{Q} \begin{pmatrix} \Lambda & \mathbb{0} \\ \mathbb{0} & \Lambda^{-1} \end{pmatrix} \mathsf{Q}^{-1} \tag{2.20}$$

gives, in the basis (g_n), the Bloch modes of the periodic waveguide. With Λ the eigenvalues associated to the right-going Bloch modes, the transmission of waves through the M cells is characterized by the scattering matrix

$$\mathcal{S} = \begin{pmatrix} \mathbb{0} & \Lambda^M \\ \Lambda^M & \mathbb{0} \end{pmatrix}, \tag{2.21}$$

and the overall matrix of the M-cell system then reads as the composition

$$\mathsf{S} = \mathsf{S}^{(\mathrm{l})} \star \mathcal{S} \star \mathsf{S}^{(\mathrm{r})}, \tag{2.22}$$

where

$$\mathsf{S}_{\mathrm{l,r}} = \begin{pmatrix} \mathsf{R}^{(\mathrm{l,r})} & \mathsf{T}^{(\mathrm{l,r})\prime} \\ \mathsf{T}^{(\mathrm{l,r})} & \mathsf{R}^{(\mathrm{l,r})\prime} \end{pmatrix} \tag{2.23}$$

are the scattering matrices of the left and right interfaces, mapping the Bloch modes to the leads propagating modes (N). Thus, from Eqs. (2.22-2.25), we can write the transmission matrix as

$$\mathsf{T} = \mathsf{T}^{(\mathrm{r})} \left(\mathbb{1} - \Lambda^M \mathsf{R}^{(\mathrm{l})\prime} \Lambda^M \mathsf{R}^{(\mathrm{r})} \right)^{-1} \Lambda^M \mathsf{T}^{(\mathrm{l})}. \tag{2.24}$$

Note that the interface scattering matrices $\mathsf{S}_{\mathrm{l,r}}$ are completely known from the blocks Q_{1-4} of the eigenvector matrix Q of Eq. (2.20):

$$\mathsf{S}_{\mathrm{l}} = \begin{pmatrix} \mathsf{Q}_3 \mathsf{Q}_1^{-1} & \mathsf{Q}_4 - \mathsf{Q}_3 \mathsf{Q}_1^{-1} \mathsf{Q}_2 \\ \mathsf{Q}_1^{-1} & -\mathsf{Q}_1^{-1} \mathsf{Q}_2 \end{pmatrix}, \tag{2.25a}$$

$$\mathsf{S}_{\mathrm{r}} = \begin{pmatrix} -\mathsf{Q}_4^{-1} \mathsf{Q}_3 & \mathsf{Q}_4^{-1} \\ \mathsf{Q}_1 - \mathsf{Q}_2 \mathsf{Q}_4^{-1} \mathsf{Q}_3 & \mathsf{Q}_2 \mathsf{Q}_4^{-1} \end{pmatrix}. \tag{2.25b}$$

2.D Simplified expressions of T

If, after possibly being reordered, the Bloch eigenvalues are such that the first one, Λ_1, is large compared with all others, then the term $\Lambda^M \mathsf{R}^{(\mathrm{l})\prime} \Lambda^M \mathsf{R}^{(\mathrm{r})}$ in Eq. (2.24) can be approximated as

$$\Lambda^M \mathsf{R}^{(\mathrm{l})\prime} \Lambda^M \mathsf{R}^{(\mathrm{r})} \approx \Lambda_1^{2M} \mathsf{R}_{11}^{(\mathrm{l})\prime} \mathsf{A} \tag{2.26}$$

with A is a matrix whose first row is that of $\mathsf{R}^{(\mathrm{r})}$ and all the others are zero. A being a rank one matrix, we can use the Sherman-Morrison identity to calculate the inverse matrix

$$(\mathbb{1} - \Lambda_1^{2M} \mathsf{R}_{11}^{(\mathrm{l})\prime} \mathsf{A})^{-1} = \mathbb{1} + \frac{\Lambda_1^{2M} \mathsf{R}_{11}^{(\mathrm{l})\prime} \mathsf{A}}{1 - \Lambda_1^{2M} \mathsf{R}_{11}^{(\mathrm{l})\prime} \mathsf{R}_{11}^{(\mathrm{r})}}. \tag{2.27}$$

It follows that the transmission matrix (2.24) can be approximated by the rank one matrix

$$\mathsf{T} \approx \tilde{\mathsf{T}} = \frac{\Lambda_1^M}{1 - \Lambda_1^{2M} \mathsf{R}_{11}^{(\mathrm{l})\prime} \mathsf{R}_{11}^{(\mathrm{r})}} \boldsymbol{T}_1^{(\mathrm{r})} \boldsymbol{T}_1^{(\mathrm{l})\mathsf{T}}, \tag{2.28}$$

with $\boldsymbol{T}_1^{(\mathrm{r})}$ the first column of $\mathsf{T}^{(\mathrm{r})}$ and $\boldsymbol{T}_1^{(\mathrm{l})\mathsf{T}}$ the first row of $\mathsf{T}^{(\mathrm{l})}$.

If the Bloch eigenvalues are such that the first two, Λ_1 and Λ_2, are large compared with all others, then a similar analysis, with notably the use of the Woodbury matrix identity that generalizes the Sherman-Morrison identity, allows us to approximate the term $\left(\mathbb{1} - \mathsf{\Lambda}^M \mathsf{R}^{(\mathrm{l})\prime} \mathsf{\Lambda}^M \mathsf{R}^{(\mathrm{r})}\right)^{-1} \mathsf{\Lambda}^M$ in Eq. (2.24) by

$$\left(\mathbb{1} - \mathsf{\Lambda}^M \mathsf{R}^{(\mathrm{l})\prime} \mathsf{\Lambda}^M \mathsf{R}^{(\mathrm{r})}\right)^{-1} \mathsf{\Lambda}^M \approx \begin{pmatrix} \mathsf{P} & \mathbb{0} \\ \mathbb{0} & \mathbb{0} \end{pmatrix} \tag{2.29}$$

where P is a 2×2 matrix dependent on the eigenvalues $\Lambda_{1,2}^M$ and on the first 2×2 blocks of the reflection matrices $\mathsf{R}^{(\mathrm{l})\prime}$ and $\mathsf{R}^{(\mathrm{r})}$:

$$\mathsf{P} = \lambda \rho^{(\mathrm{l})} \lambda (\mathbb{1}_2 + \rho^{(\mathrm{r})} \lambda \rho^{(\mathrm{l})} \lambda)^{-1} \rho^{(\mathrm{r})} \lambda, \tag{2.30}$$

with

$$\lambda = \begin{pmatrix} \Lambda_1^M & 0 \\ 0 & \Lambda_2^M \end{pmatrix}, \tag{2.31a}$$

$$\rho^{(\mathrm{l})} = \begin{pmatrix} \mathsf{R}_{11}^{(\mathrm{l})\prime} & \mathsf{R}_{12}^{(\mathrm{l})\prime} \\ \mathsf{R}_{21}^{(\mathrm{l})\prime} & \mathsf{R}_{22}^{(\mathrm{l})\prime} \end{pmatrix}, \tag{2.31b}$$

$$\rho^{(\mathrm{r})} = \begin{pmatrix} \mathsf{R}_{11}^{(\mathrm{r})} & \mathsf{R}_{12}^{(\mathrm{r})} \\ \mathsf{R}_{21}^{(\mathrm{r})} & \mathsf{R}_{22}^{(\mathrm{r})} \end{pmatrix}. \tag{2.31c}$$

Then, the transmission matrix can be approximated by

$$\mathsf{T} \approx \tilde{\mathsf{T}} = \boldsymbol{u}_1 \boldsymbol{T}_1^{(\mathrm{l})\mathsf{T}} + \boldsymbol{u}_2 \boldsymbol{T}_2^{(\mathrm{l})\mathsf{T}}, \tag{2.32}$$

with

$$\boldsymbol{u}_1 = \mathsf{P}_{11} \boldsymbol{T}_1^{(\mathrm{r})} + \mathsf{P}_{21} \boldsymbol{T}_2^{(\mathrm{r})}, \tag{2.33a}$$

$$\boldsymbol{u}_2 = \mathsf{P}_{12} \boldsymbol{T}_1^{(\mathrm{r})} + \mathsf{P}_{22} \boldsymbol{T}_2^{(\mathrm{r})}, \tag{2.33b}$$

and where $\boldsymbol{T}_1^{(\mathrm{r})}$ and $\boldsymbol{T}_2^{(\mathrm{r})}$ are the first two columns of $\mathsf{T}^{(\mathrm{r})}$ and $\boldsymbol{T}_1^{(\mathrm{l})\mathsf{T}}$ and $\boldsymbol{T}_2^{(\mathrm{l})\mathsf{T}}$ the first two rows of $\mathsf{T}^{(\mathrm{l})}$.

Chapter 3

Experimental observation of the speckle pattern invariance in periodic waveguides

3.1 Introduction

The invariance of the transmitted speckle pattern to incidence conditions is known in disordered media in the localized regime [7, 38–40]. This phenomenon, which we refer to as the "freezing of the transmitted pattern", is a consequence of the single-channel regime in disordered media [2, 4, 8, 28].

In Chap. 2, we demonstrated that the invariance of the transmitted speckle pattern is not exclusively associated with the disorder; it can also be observed in regular-periodic media. Through numerical simulations, we showed that insensitivity to incidence conditions is observed when at most one right-going Bloch mode propagates in the finite periodic waveguide. The periodic case is notably distinct from the disordered case, as it enables freezing with a non-weak transmission.

In this chapter, we aim to provide experimental observations of the invariance of the transmitted pattern in a finite periodic acoustic waveguide. First, we introduce our experimental setup. We then recall the similarity function already defined in Chap. 2, which, once derived from the experimental results, allows us to identify the frequency region where the freezing phenomenon occurs. Finally, we present the pattern of the acoustic field for several incidence conditions corresponding to frequencies located in bands with zero, one, or two propagating Bloch modes.

3.2 Experimental setup

Our experimental setup consists in a M-cell d-periodic acoustic waveguide, with $M = 5$ and $d = 255$ mm (Fig. 3.1). It is constructed by using a periodic arrangement of PVC

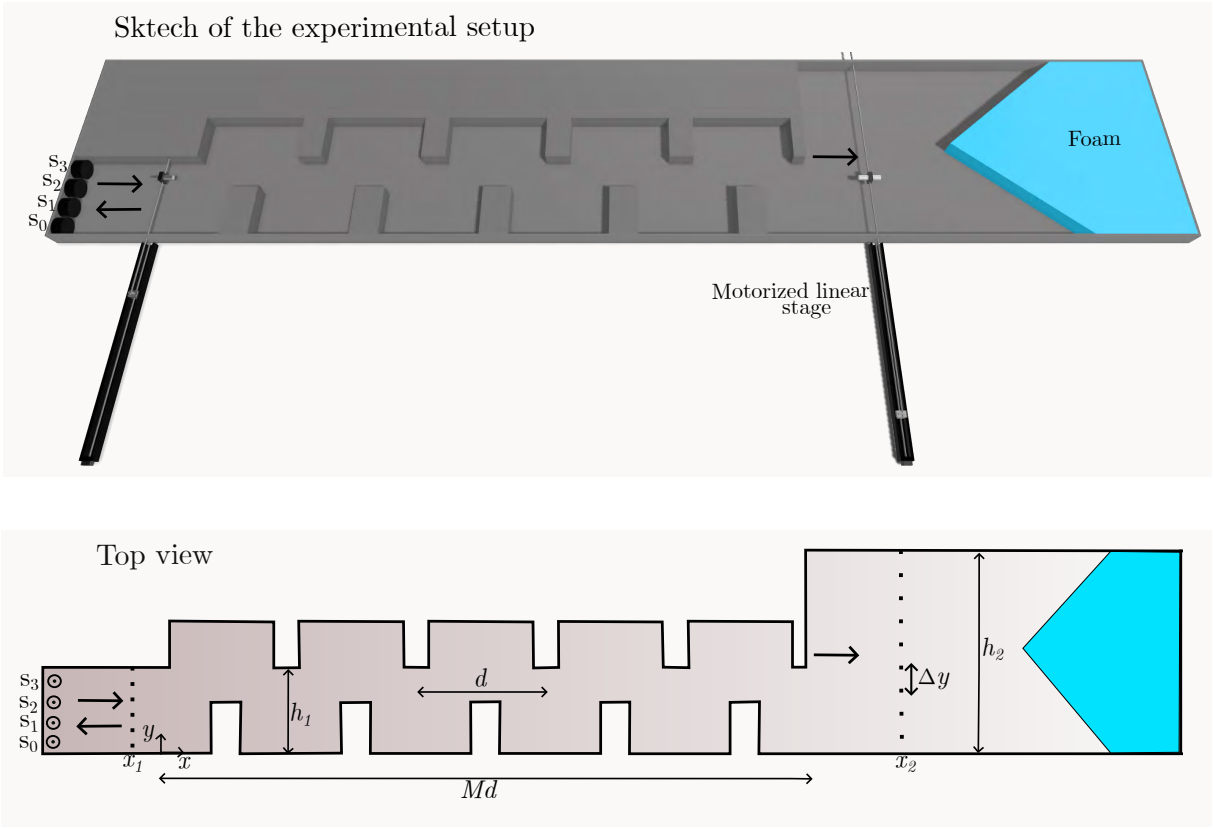

Figure 3.1 – Sketch and top view of the experimental setup. The top plate in the sketch is removed to see the interior of the waveguide. The scattering region, defined as $x \in [0, Md]$, is composed of a finite periodic waveguide ($M = 5$, $d = 255$ mm). Four acoustic sources, denoted as s_0, s_1, s_2, and s_3, are positioned at the left end of the waveguide with a width of $h_1 = 170$ mm. The positions of the microphones used to measure the pressure field along the y direction are labeled as x_1 and x_2. The right end of the waveguide, with a width of $h_2 = 400$ mm, is made of a foam block of triangular shape.

blocks. We assume that all the block boundaries are rigid and perfectly reflecting. The cell is a piecewise constant waveguide element composed of five discontinuously connected segments. The dimensions of the segments from the left end of the unit cell are $0.1d \times h_1$, $0.32d \times 1.53h_1$, $0.23d \times 0.93h_1$, $0.25d \times 1.53h_1$ and $0.1d \times h_1$. The left waveguide having a width of $h_1 = 170$ mm is assumed to support N_1 propagating modes, with a first cut-off frequency $f_c \approx 1$ kHz. Four identical high speakers are mounted at the left end of the

waveguide. They are equally spaced along the y-direction, with a diameter of 40 mm, and operate within the frequency range $f \in [3, 20]$ kHz. N_2 are propagating modes in the output section. The right end of the waveguide with height $h_2 = 400$ mm, is anechoic thanks to a foam block of triangular shape [5]. Two microphones with sensitivities of 1.16 mV/Pa and 1.65 mV/Pa and diameters of $\frac{1}{4}''$ are positioned at $x = x_1$ and $x = x_2$ on a rod connected to a motorized linear stage. This setup allows for the measurement of the pressure field at multiple points along the y-direction, evaluated at $\Delta y = 5$ mm intervals. The waveguide height along the z-direction is $h_z = 15$ mm, resulting in a cutoff frequency of approximately 11.50 kHz. Our study focuses on a frequency range from 3.50 kHz to 4 kHz, allowing us to treat the waveguide as effectively 2D, the field being uniform in the z-direction.

3.3 Freezing characterization

The freezing of the transmitted pattern can be characterized by determining the transmission eigenvalues ($\tau_1 > \tau_2 > ... > \tau_{N_1}$) of the M-cell periodic waveguide; freezing occurs when $\tau_1 \gg \tau_2$. This method requires finding the transmission matrix T [5, 48] with dimensions $N_2 \times N_1$. To determine T N_1 different source conditions would be necessary with the measurement of the pressure field in four different cross sections to separate the left and right going waves on both sides of the scattering regions. Instead, we used a simpler approach to characterize the freezing. It consists in measuring the similarity between the transmitted pattern $\psi_j(x_2, y)$ generated by the source s_j, with $j = 0, 1, 2, 3$, and the reference transmitted pattern $\psi_0(x_2, y)$ generated by the source s_0. This method requires only one microphone to measure the profile of the transmitted acoustic field at $x_2 > Md$, and it is independent of the number of propagating modes N_1. We define the similarity function as follows:

$$F_j = \frac{|\int_0^{h_2} \psi_0(x_2, y)\psi_j^*(x_2, y)\,\mathrm{d}y|}{\sqrt{\int_0^{h_2} |\psi_0(x_2, y)|^2\,\mathrm{d}y \int_0^{h_2} |\psi_j(x_2, y)|^2\,\mathrm{d}y}}. \tag{3.1}$$

The similarity function F_j is a normalized scalar product. $F_j = 1$ if the profiles of the acoustic field are identical, $F_j < 1$ otherwise, as a consequence of the Cauchy-Schwarz inequality [50].

Following the reasoning made in the theoretical case, we can expect freezing of the transmitted pattern if at most one Bloch mode is propagating. Fig. 3.2(a) shows the

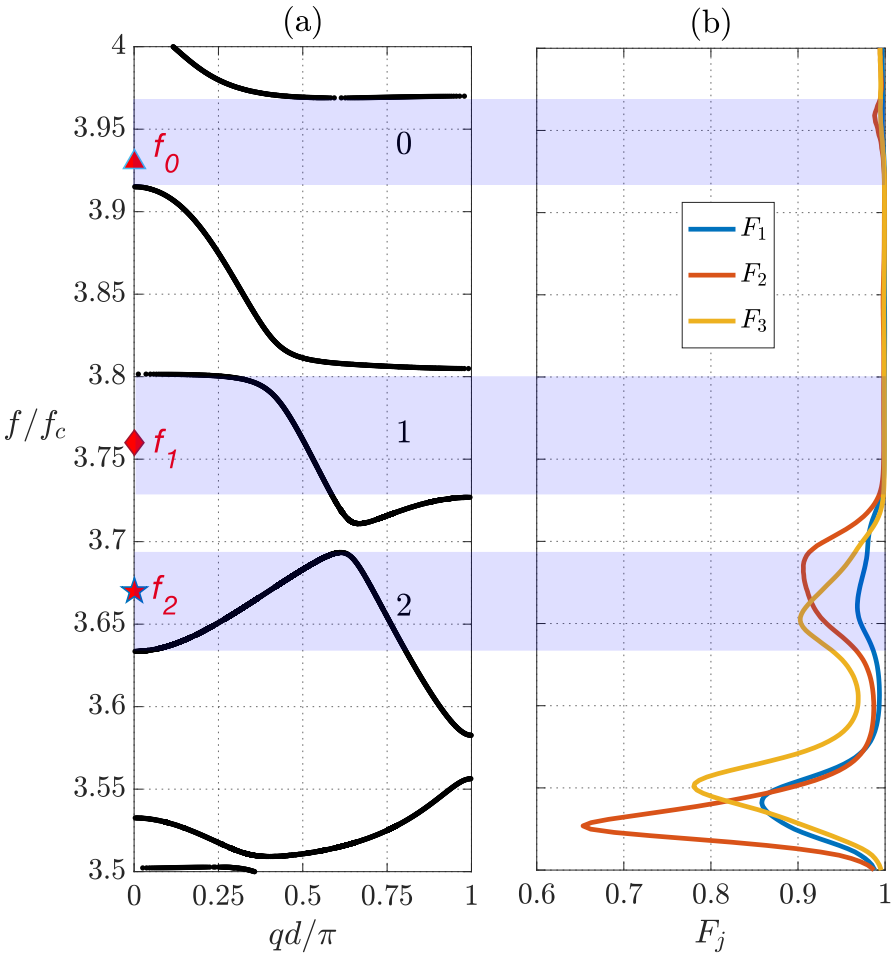

Figure 3.2 – (a) Theoretical dispersion relation of an infinite periodic waveguide in the frequency range $f/f_c \in [3.5, 4]$. The numbers in the left plot are the number of right-going propagating Bloch modes in the corresponding colored frequency interval. The red-filled triangle (f_0), diamond (f_1), and star (f_2) represent the frequencies of excitation used to show the experimental pattern of the pressure field in Figs. 3.3, 3.4 and 3.5 respectively. Numerics are performed using a mode matching method; for more details on the calculations, refer to Chap. 2 and [47, 49]. (b) Experimental results: spectrum of the similarity functions F_1, F_2, and F_3 as defined in Eq. (3.1), in the same frequency range.

theoretical dispersion relation of the periodic medium, calculated through a numerical simulation, in a frequency range such that $N_1 = 4$ and $N_2 \in [8, 9]$. Comparing the theoretical dispersion relation (Fig. 3.2(a)), to the spectrum of the similarity functions F_1, F_2 and F_3, derived from experimental results (Fig. 3.2(b)), we observed that the similarity functions tend to unity for two different regions: the first region corresponds to

a bandgap, the second region corresponds to a band with one propagating Bloch mode. The similarity functions are different than unity for the regions that correspond to a band with two propagating Bloch modes.

3.4 Experimental observation: pattern of pressure field

3.4.1 Insensitivity of the transmitted pattern to source position

Consider first an excitation frequency, $f_0 = 3.93$, corresponding to a bandgap in the periodic medium: no Bloch mode is propagating. At this frequency, all similarity functions, F_1, F_2, and F_3, are close to unity (Fig. 3.2(b)). An experimental observation of the insensitivity to source position with a low transmitted amplitude is shown in Fig. 3.3. We sequentially excite the acoustic sources s_j, and each time, we measure the pressure field at $x = x_1$ and $x = x_2$ along the y-axis with $\Delta y = 5$mm interval. While the excitation and, consequently, the pattern of the near field ($|\psi_j(x_1, y)|$) differ, no significant change in the pattern of the transmitted field ($|\psi_j(x_2, y)|$) can be detected, confirming our numerical studies. A significant decrease in amplitude is observed, with the average amplitude of the transmitted field being two orders of magnitude lower than the average field at $x = x_1$.

Let us consider the same experiment as the bandgap case, but with an excitation frequency, $f_1 = 3.76$, corresponding to a band with one propagating Bloch mode in the periodic medium. At this frequency, all the similarity functions are also near to 1 (Fig. 3.2(b)). Results are shown in Fig. 3.4. As in the bandgap case, while the profile of the pressure field, before the scattering region $x = x_1 < 0$, is quite different, the profile of the transmitted pressure field ($x = x_2 > Md$) is frozen. A smaller decrease in amplitude is observed compared to the bandgap case, with the average amplitude of the transmitted field being one order of magnitude lower than the average field at $x = x_1$.

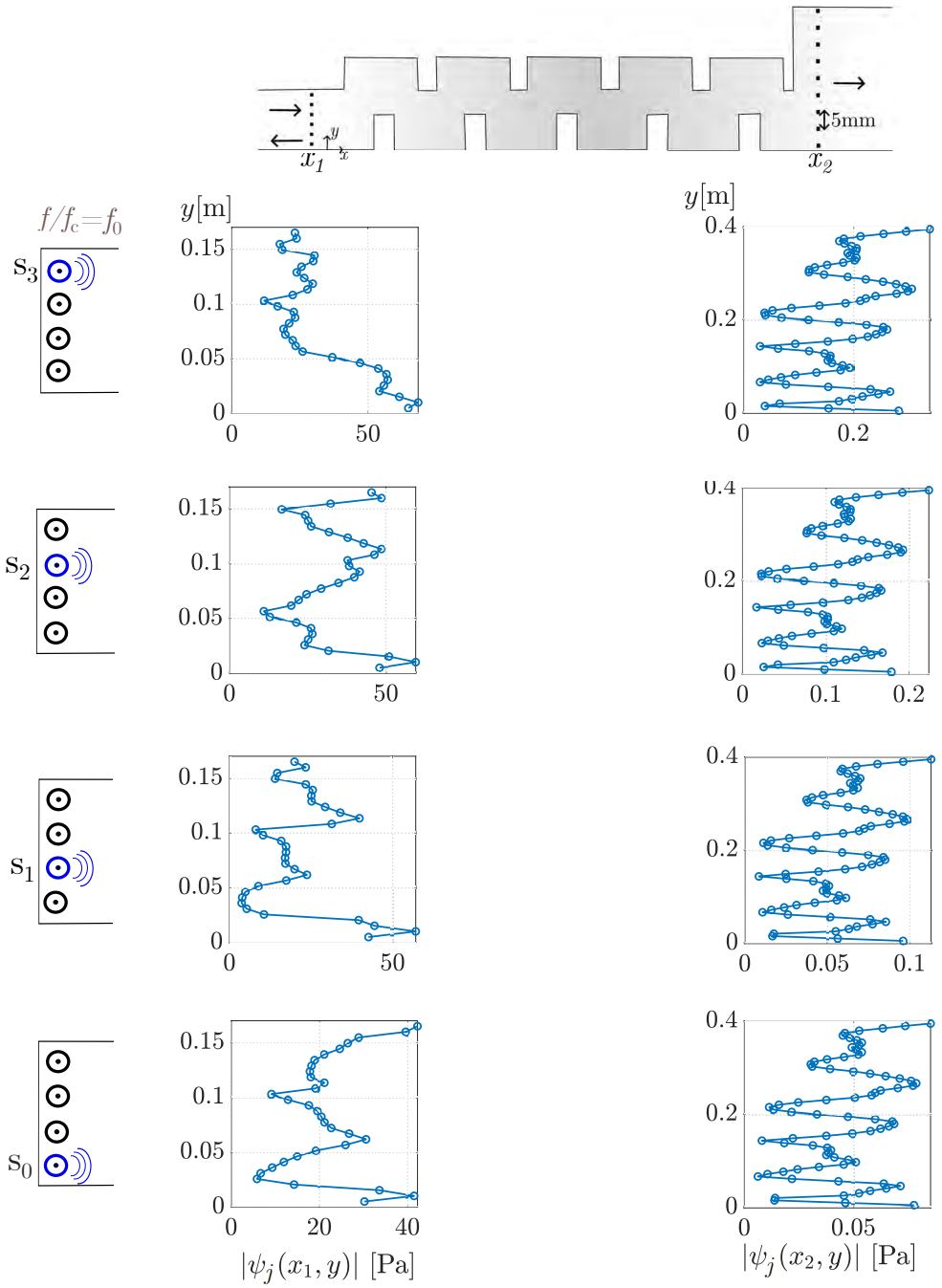

Figure 3.3 – Freezing. Experimental patterns of the pressure fields $|\psi_j(x,y)|$ at $x = x_1$ and $x = x_2$, with $j = 0, 1, 2, 3$, as generated by the sources s_j at 4 different positions, at a frequency, $f_0 = 3.93$, in a bandgap (see. Fig 3.2).

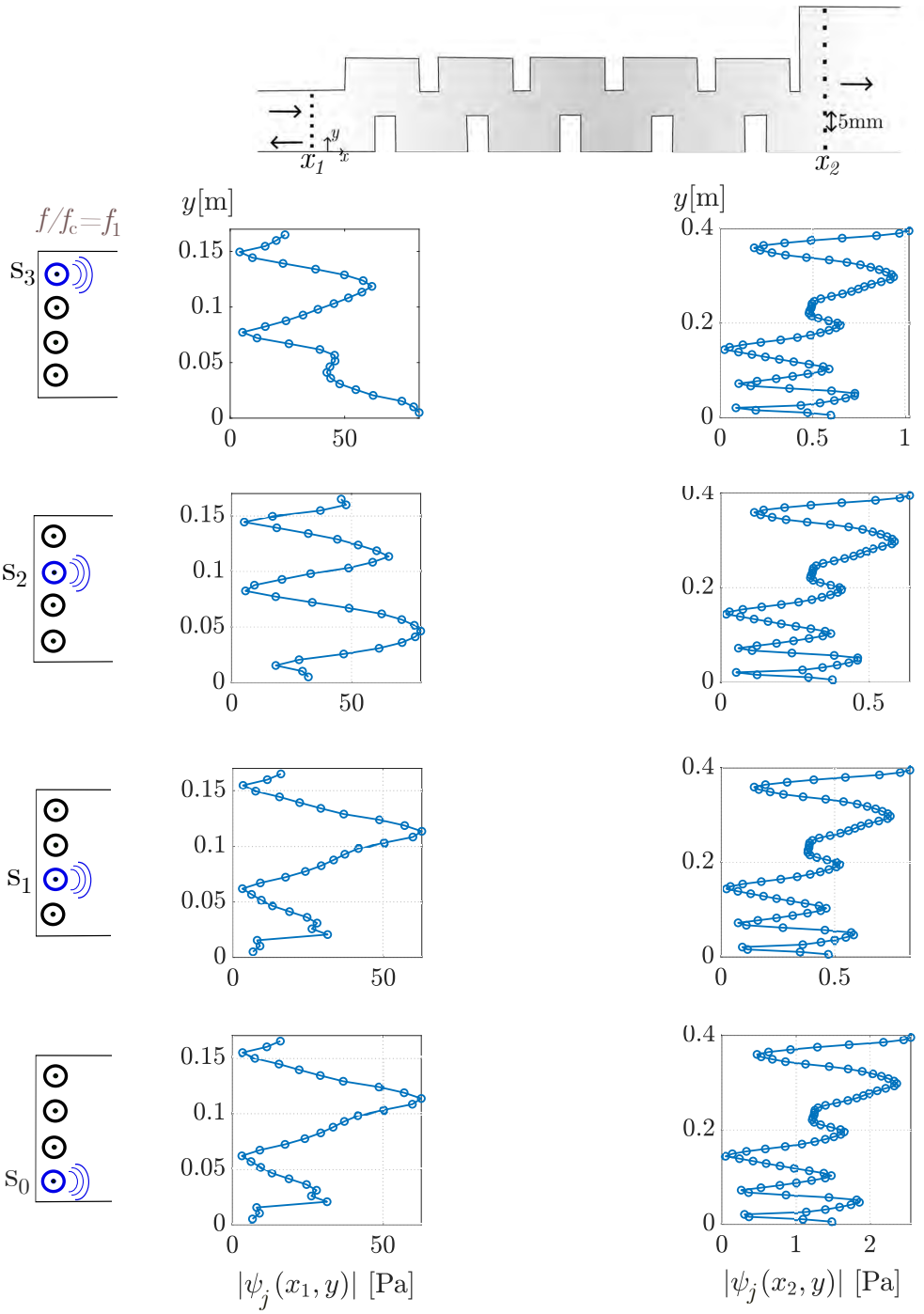

Figure 3.4 – Freezing. Experimental patterns of the pressure fields $|\psi_j(x,y)|$ at $x = x_1$ and $x = x_2$, with $j = 0, 1, 2, 3$, as generated by the sources s_j located at 4 different positions, at a frequency $f_1 = 3.76$ in a band with one propagating Bloch mode (see. Fig 3.2).

3.4.2 Sensitivity of the transmitted pattern to source position

Let us consider the same experiment as discussed in the preceding subsection; we sequentially excite the acoustic sources s_j, and each time we measure the pressure field at $x = x_1$ and $x = x_2$ along the y-axis with $\Delta y = 5$mm interval. We consider an excitation

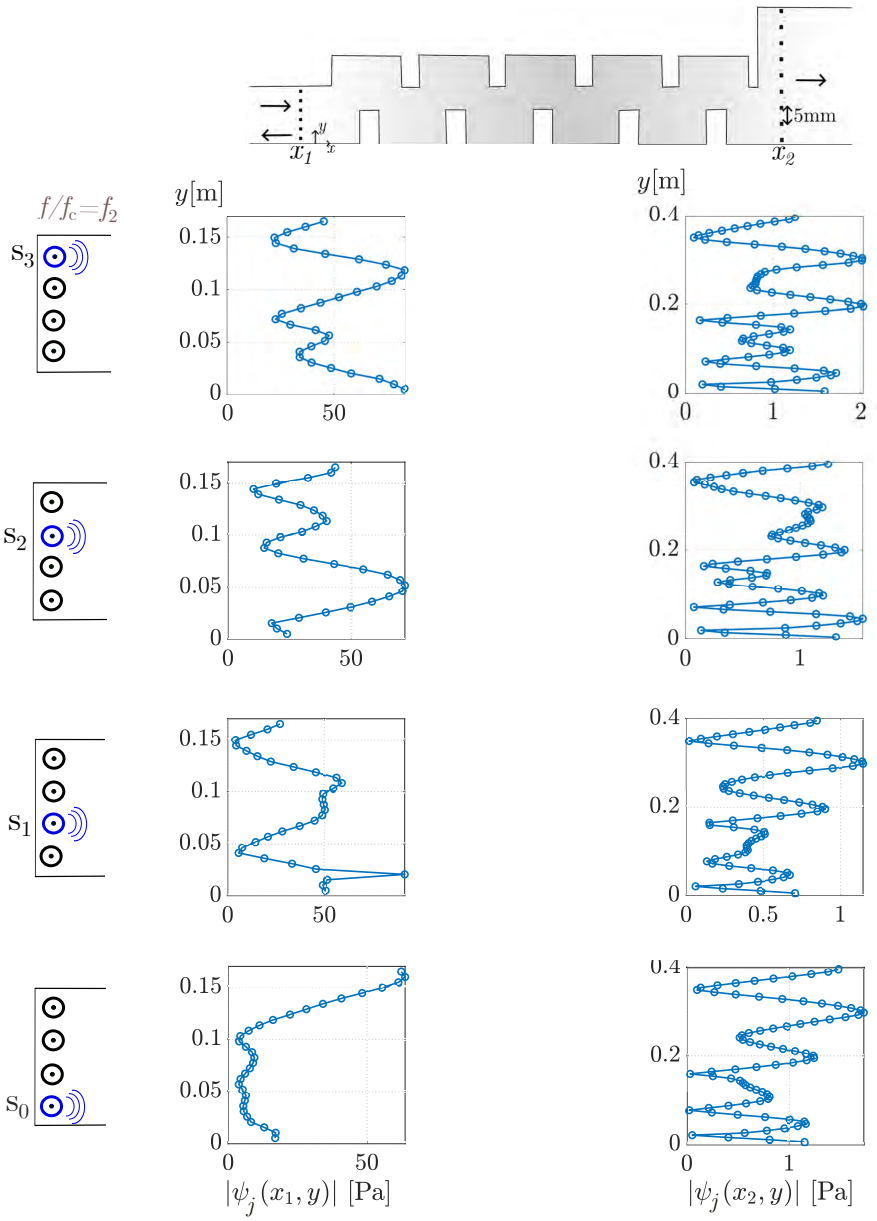

Figure 3.5 – Non-freezing. Experimental patterns of the pressure fields $|\psi_j(x,y)|$ at $x = x_1$ and $x = x_2$, with $j = 0, 1, 2, 3$, as generated by the sources s_0, s_1, s_2 and, s_3 at 4 different positions, at a frequency $f_2 = 3.67$ in a band with two propagating Bloch modes (see. Fig 3.2).

frequency, $f_2 = 3.67$, in a band with two propagating Bloch modes in the periodic medium. At this frequency, all the similarity functions are different than 1 (Fig. 3.2(b)). Fig. 3.5 shows that for different types of excitation, the pattern of the pressure field before the scattering region and after the scattering region are quite different. The pattern of the transmitted field is sensitive to the source position.

3.4.3 Rigid boundary condition at the right end of the periodic waveguide

We have seen in Chap. 2 and in the preceding subsections that the pattern of the transmitted field remains insensitive to the incidence conditions if the frequency of excitation is within a bandgap or a band with one propagating Bloch mode. We can expect

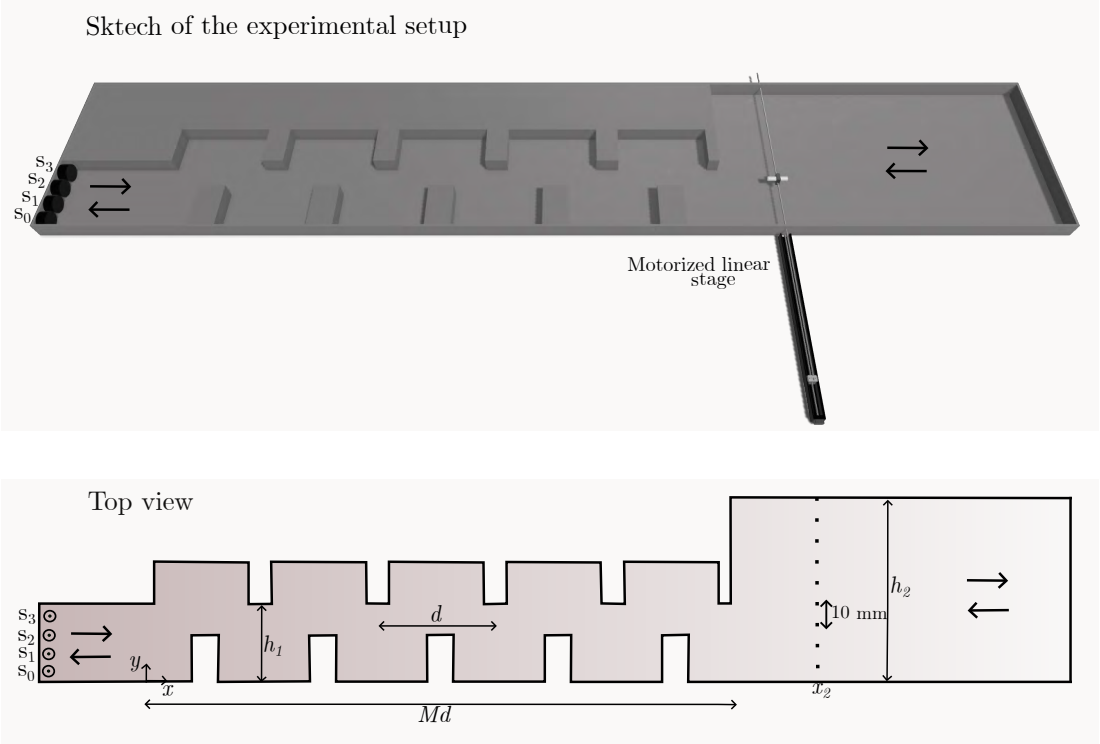

Figure 3.6 – Sketch and top view of the modified experimental setup. The top plate in the sketch is removed to see the interior of the periodic waveguide ($M = 5$, $d = 255$ mm). Four acoustic sources, denoted as s_0, s_1, s_2, and s_3, are positioned at the left end of the waveguide with a width of $h_1 = 170$ mm. The position of the microphone used to measure the pressure field along the y direction is labeled as x_2. The right end of the waveguide, with a width of $h_2 = 400$ mm is closed.

that by changing the right-end boundary conditions, from absorbing (Fig. 3.1) to a rigid boundary (Fig. 3.6), the pattern of the total field at $x = x_2$ remains insensitive to the incidence conditions as shown in (Fig. 3.7).

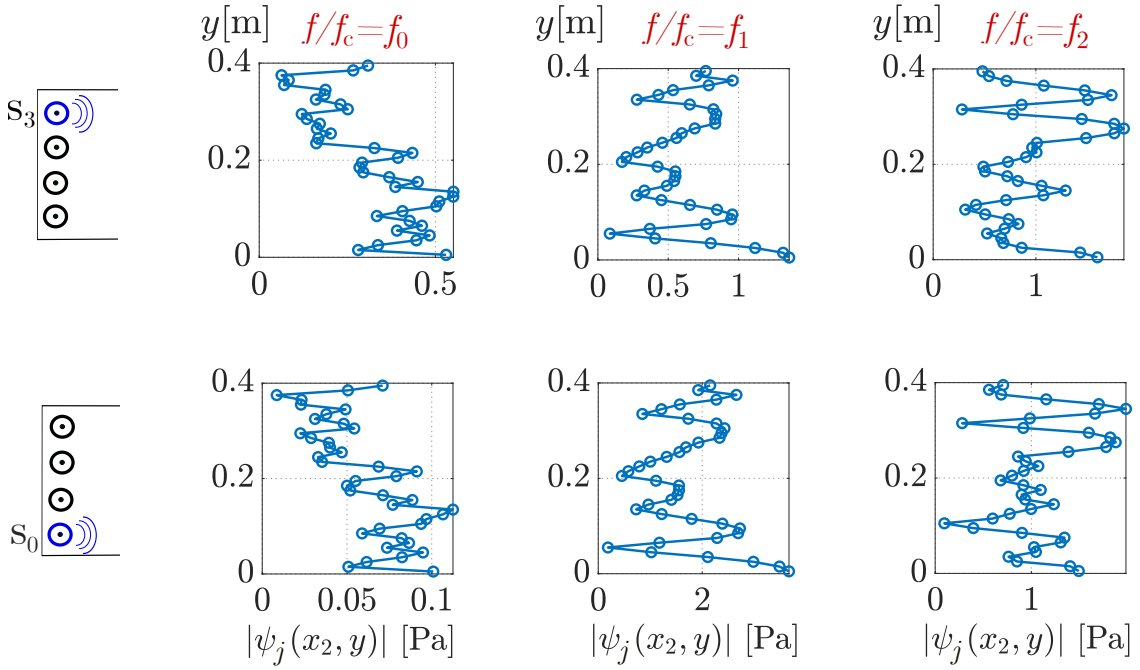

Figure 3.7 – Experimental patterns of the pressure fields $|\psi_0(x_2, y)|$ and $|\psi_3(x_2, y)|$, as generated by 2 sources s_0 and s_3 at two different positions. At a frequency $f_0 = 3.93$ in a bandgap, at a frequency $f_1 = 3.76$ in a band with one propagating Bloch mode, and at a frequency $f_2 = 3.67$ in a band with two propagating Bloch modes.

3.5 Conclusion

In conclusion, our experimental observations reveal that a periodic waveguide can exhibit a transmission property similar to the single-channel regime observed in Anderson-localized disordered media. It results in the invariance of the transmitted speckle pattern with the incident wave. Consistent with the theoretical studies, the insensitivity to incidence condition is observed if at most one Bloch mode propagates in the finite periodic waveguide.

Chapter 4

Invariance of the transmitted pattern in gratings

4.1 Introduction

In Chapters 2 and 3 we showed numerically and experimentally that the invariance of the transmitted wave pattern to incidence conditions (freezing of the transmitted pattern) can be observed in quasi-1D finite periodic waveguides if at most one Bloch mode is propagating; the first transmission eigenvalue dominates all the others, thus a single channel dominates the transmission. We can therefore wonder about the fate of this property in the case of scattering by a grating having a finite periodic structure in the direction of propagating (Fig. 4.1). This is the purpose of this chapter.

To do so, we need to illuminate the grating with different incidence conditions. The simplest way would be to send a plane wave and vary its angle of incidence θ_0. However, the band structure of the system a priori depends on θ_0, hence the conditions of invariance of the transmitted pattern. Changing θ_0 may thus prevent us from observing the freezing. An alternative way, while keeping a plane wave as the source, is to insert a grating with the same periodicity before the grating of interest (Fig. 4.1 (a)). Then by modifying this first grating (by, e.g., rotating the scatterers as in Fig. 4.1 (b)), we can control and change the incident wave on the grating of interest, while keeping θ_0 constant.

In this chapter, we start with a general overview of the scattering by a grating and present the solution of the wave equation in a multimodal formulation. We invite the readers to refer to [51–55] for more details on the theoretical aspect of gratings. We illustrate the field with the simple case of grating made of rigid rectangular scatterers. Then, we analyze the Figure shown in Fig. 4.1 and show that, indeed, such grating can freeze the transmitted wave. Moreover, this particular configuration is made of horizontal structured waveguides that are not connected along the transverse direction, it appears that the frequency bands in which freezing is observed do not depend on θ_0. The frozen

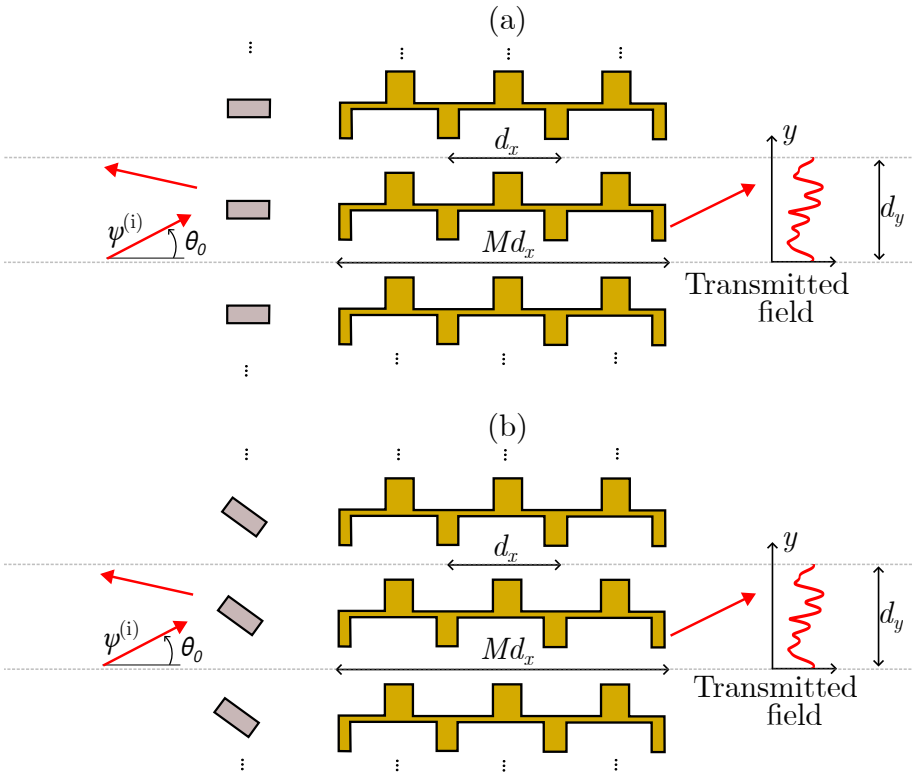

Figure 4.1 – Invariance of the transmitted speckle pattern with the incidence conditions on a grating (here displayed in yellow). To obtain different conditions of incidence, the incident plane wave $\psi^{(i)}$, shown in red with a fixed angle θ_0, is first scattered by a grating (in gray) in various configurations. Both gratings have the same d_y periodicity along the transverse direction y.

pattern will, however, not be the same when changing θ_0. As opposed to this "closed" configuration (unconnected horizontal waveguides), we study in the next section an "open" configuration, where the waveguides are connected in the transverse direction. in this new configuration, the dependence of the freezing condition on the angle of incidence clearly appears, making this grating a more versatile device to control the freezing.

4.2 Scattering by a grating: generalities

We aim to solve the scattering problem of an incident plane wave by a grating, here made of scatterers located within a region $0 \leq x \leq L_s$ (Fig. 4.2 (a)). The grating is d_y-periodic along the transverse direction y. The solution of the problem, namely the wave

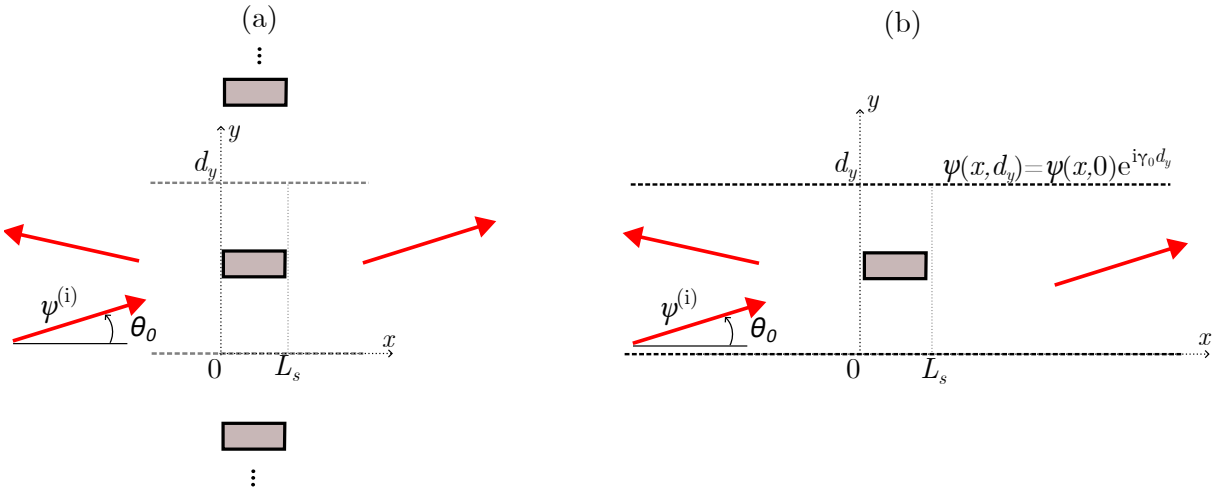

Figure 4.2 – (a) Grating made of rectangular scatterers with d_y periodicity along the vertical direction y. The grating is illuminated by an incident plane wave $\psi^{(i)}$ with an incident angle θ_0. (b) A single period of height d_y is considered with pseudo-periodic boundary conditions.

field ψ, satisfies the Helmholtz equation,

$$(\Delta + k^2)\psi(x, y) = 0, \tag{4.1}$$

with k the wavenumber. The wave field corresponds to the sum of an incident wave $\psi^{(i)}$ and a scattered wave. The incident wave $\psi^{(i)}$ is a plane wave:

$$\psi^{(i)}(x < 0, y) = \frac{e^{i(\alpha_0 x + \gamma_0 y)}}{\sqrt{d_y}}, \tag{4.2}$$

with $\alpha_0 = k\cos\theta_0$ and $\gamma_0 = k\sin\theta_0$ the horizontal and vertical component of the wavevector $\mathbf{k}$ ($|\mathbf{k}|^2 = \alpha_0^2 + \gamma_0^2 = k^2$) and $\theta_0 \in]\frac{-\pi}{2}, \frac{\pi}{2}[$ the incident angle.

Due to the d_y-periodicity of the grating in the transverse direction y, the problem can be solved in a single period of height d_y (Fig. 4.2 (b)). Therefore, in the two semi-infinite regions $(x, y) \in]-\infty, 0] \times [0, d_y]$ and $(x, y) \in [L_s, +\infty[\times[0, d_y]$, the field satisfies

the Helmholtz equation (Eq. 4.1), and the pseudo-periodic boundary conditions,

$$\begin{cases} \psi(x, y = d_y) = \mathrm{e}^{\mathrm{i}\gamma_0 d_y}\psi(x, y = 0), \\ \partial_y\psi(x, y = d_y) = \mathrm{e}^{\mathrm{i}\gamma_0 d_y}\partial_y\psi(x, y = 0). \end{cases} \tag{4.3}$$

For the following, a multimodal method is presented to solve Eqs. (4.1) and (4.3).
The field is now decomposed as a pseudo-Fourier series,

$$\psi(x, y) = \sum_n a_n(x)g_n(y), \tag{4.4}$$

where a_n are the modal amplitudes and g_n the transverse functions

$$g_n = \frac{\mathrm{e}^{\mathrm{i}\gamma_n y}}{\sqrt{d_y}}, \tag{4.5}$$

with $\gamma_n = \gamma_0 + n2\pi/d_y$, $n \in \mathbb{Z}$. These functions form an orthogonal basis satisfying the relations,

$$(g_n, g_m) = \delta_{nm} \quad \text{and} \quad (g_n', g_m') = \gamma_n^2\delta_{nm}, \tag{4.6}$$

with $(f_1, f_2) = \int_0^{d_y} f_1 f_2^* \, \mathrm{d}y$ the scalar product.
By projecting the Helmholtz equation onto the basis of the g_n functions, we obtain the second-order equation,

$$a_n''(x) + \alpha_n^2 a_n(x) = 0, \tag{4.7}$$

where

$$\alpha_n = \sqrt{k^2 - \gamma_n^2} \tag{4.8}$$

is the longitudinal wave number associated with mode n. Eq. (4.8) separates the N propagating modes for which $\alpha_n \in \mathbb{R}^+$ and the evanescent modes for which $\alpha_n \in \mathrm{i}\mathbb{R}^+$. The solution of the second-order equation (Eq. (4.7)) reads as a sum of right-going ($\mathrm{e}^{\mathrm{i}\alpha_n x}$) and left-going ($\mathrm{e}^{-\mathrm{i}\alpha_n x}$) waves. Thus, with an incident wave $\psi^{(\mathrm{i})}$ coming from the left, the field in the two semi-infinite regions $(x, y) \in]-\infty, 0] \times [0, d_y]$ and $(x, y) \in [L_s, +\infty[\times[0, d_y]$ reads as,

$$\psi(x,y) = \begin{cases} \dfrac{1}{\sqrt{d_y}} \left(\mathrm{e}^{\mathrm{i}(\alpha_0 x + \gamma_0 y)} + \sum\limits_n c_n^- \mathrm{e}^{\mathrm{i}(\alpha_n x + \gamma_n y)} \right), & \text{for } \mathrm{x} \leq 0 \\ \dfrac{1}{\sqrt{d_y}} \sum\limits_n d_n^+ \mathrm{e}^{\mathrm{i}(\alpha_n (x - L_s) + \gamma_n y)}, & \text{for } \mathrm{x} \geq L_s, \end{cases} \tag{4.9}$$

with c_n^- (resp. d_n^+) the modal amplitude of the reflected (resp. transmitted) wave. If we restrict the above series to the N propagating modes and define the $N \times 1$ vectors $\boldsymbol{g} \equiv (g_n)$, $\boldsymbol{a}^+(0) \equiv (\delta_{n0})$, $\boldsymbol{a}^-(0) \equiv (c_n^-)$ and $\boldsymbol{a}^+(L_s) \equiv (d_n^+)$, at both ends of the scattering region, Eq. (4.9) can be rewritten as,

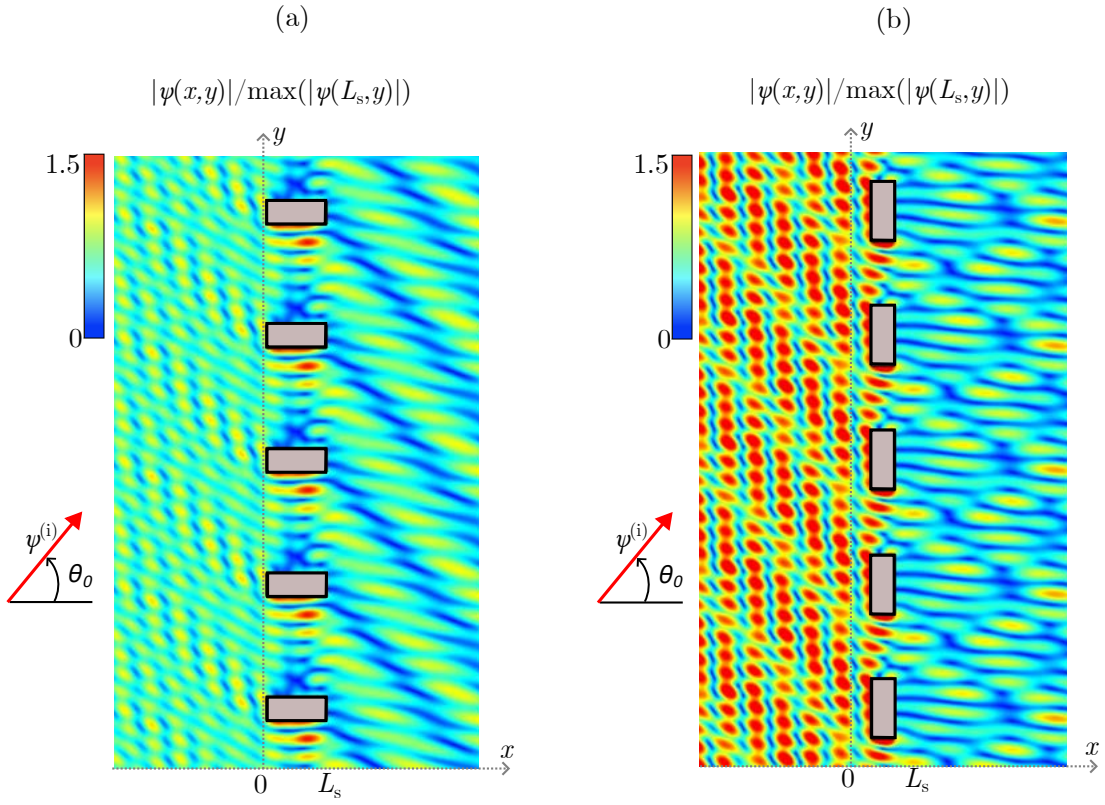

Figure 4.3 – Sensitivity of the transmitted field pattern to the orientation of the scatterers. Wavefield modulus in a grating made of rigid rectangular scatterers with a periodicity of $d_y = 1.65$. An incident plane wave illuminates the grating at a frequency $kd_y/2\pi = 4$ and an angle of incidence $\theta_0 = 1$ rad, where the number of propagating modes $N = 8$. (a) The dimensions of the rectangular scatterers are 0.8×0.32. (b) The rectangular scatterers in (a) are rotated by 90 degrees. Numerics are performed using a finite element method (Comsol Multiphysics).

$$\begin{aligned} \psi(0,y) &= \boldsymbol{g}^{\mathsf{T}}(y)\,(\mathbb{1}+\mathsf{R})\,\boldsymbol{a}^{+}(0), \\ \psi(L_s,y) &= \boldsymbol{g}^{\mathsf{T}}(y)\mathsf{T}\boldsymbol{a}^{+}(0), \end{aligned} \tag{4.10}$$

where R (resp. T) is the reflection (resp. transmission) matrix with dimensions $N \times N$. It relates the modal amplitudes of the reflected (resp. transmitted) wave to modal amplitudes of the incident wave, namely $\boldsymbol{a}^{-}(0) = \mathsf{R}\boldsymbol{a}^{+}(0)$ (resp. $\boldsymbol{a}^{+}(L_s) = \mathsf{T}\boldsymbol{a}^{+}(0)$).

Fig. 4.3 shows the total field in a grating with both horizontal and vertical orientations of the rigid scatterers. It highlights the sensitivity of the transmitted field pattern to the change in the orientation of the scatterers. Therefore, modifying the orientation of the scatterers leads to different modal amplitudes of the transmitted field, such that if T, T' are their corresponding transmission matrices, the vector $\mathsf{T}\boldsymbol{a}^{+}(0)$ is not parallel to $\mathsf{T}'\boldsymbol{a}^{+}(0)$. Note that, for simplicity, we have only modified the orientation of rectangular scatterers, but modifying their shapes would produce the same effect. Now, we are able to send various incident waves on the grating of interest (the yellow one in Fig. 4.1).

4.3 Freezing with a "closed" grating

Consider first the above defined "closed" grating as shown in Fig. 4.4. The closed grating is made of structured horizontal waveguides with Neumann boundary conditions at their boundaries, which are not connected along the vertical direction y. The structured waveguides are d_x-periodic along the x-direction and consist of a finite number M of unit cells. The system is illuminated by an incident plane wave $\psi^{(\mathrm{i})}$ given by Eq. (4.1). The wave field satisfies the Helmholtz equation. The problem can be solved by considering a single period of height d_y with pseudo-periodic boundary conditions (Eq. (4.3)). Upon considering only the N propagating modes, the solution at both ends of the yellow grating is

$$\begin{aligned} \psi(0,y) &= \boldsymbol{g}^{\mathsf{T}}(y)\left(\boldsymbol{a}^{+}(0)+\boldsymbol{a}^{-}(0)\right), \\ \psi(Md_x,y) &= \boldsymbol{g}^{\mathsf{T}}(y)\boldsymbol{a}^{+}(Md_x). \end{aligned} \tag{4.11}$$

Let T be the transmission matrix of the closed grating; it relates the modal amplitude of the transmitted wave $\boldsymbol{a}^{+}(Md_x)$ to the modal amplitude of the incoming wave $\boldsymbol{a}^{+}(0)$,

$$\boldsymbol{a}^{+}(Md_x) = \mathsf{T}\boldsymbol{a}^{+}(0). \tag{4.12}$$

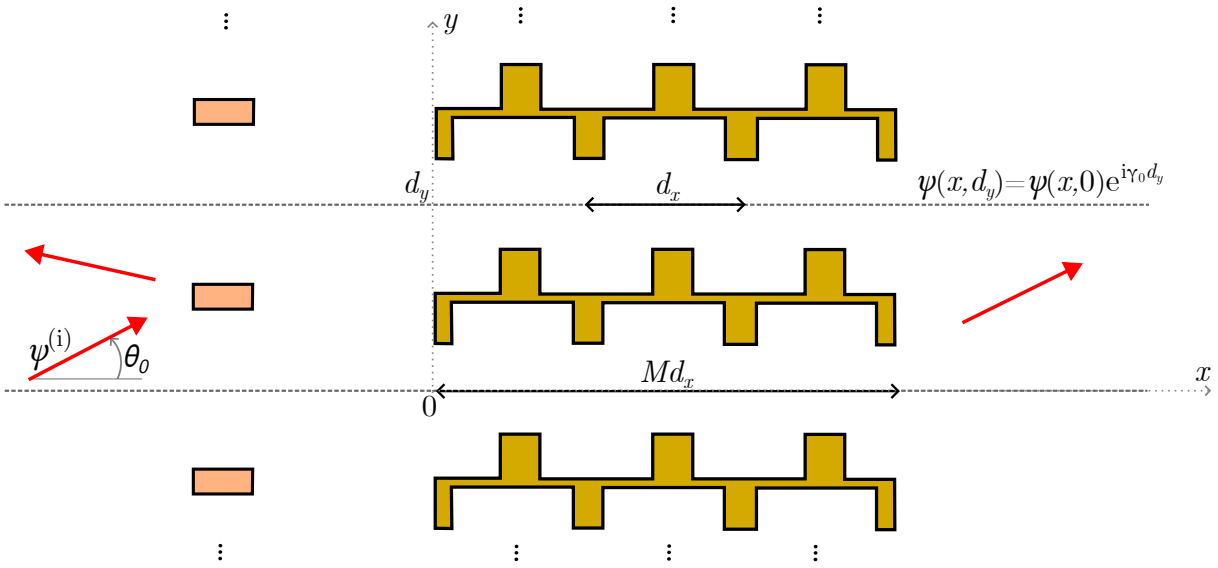

Figure 4.4 – "Closed" grating made of structured horizontal waveguides, which are not connected along the transverse direction y.

As we did in Chapter 2 to get the relation dispersion, we consider the infinite d_x-periodic equivalent of the grating shown in Fig. 4.4. Because horizontal waveguides are not connected, finding the relation of dispersion of this periodic system is equivalent to solving that of one infinite rigid periodic waveguide. As a consequence, the dispersion relation $k = \mathrm{f}(\mathbf{q})$, $\mathbf{q}$ the Bloch wave vector, is actually independent on the vertical component q_y (App. 4.B), hence on the incidence angle θ_0. The dispersion relation $k = \mathrm{f}(q_x)$ is shown in Fig. 4.5(a) in a frequency range where we can observe bands with zero, one, or two propagating Bloch modes.

Fig. 4.5(b) and (c) show the variations of the three largest transmission eigenvalues (TEVs), $\tau_1 > \tau_2 > \tau_3$, of the transmission matrix T, for two different values of θ_0, with the frequency k. In this frequency range $N = 8$. These plots show that the TEVs are weakly dependent on θ_0, and their ratii follow the band structure regardless of the incident angle θ_0. Typically, for any given θ_0, we have $\tau_1 \gg \tau_2$ for a frequency that corresponds to bandgap or a band with one propagating Bloch mode.

Following the reason stated in the periodic waveguides (Chapters 2 and 3), we can expect a freezing of the transmitted pattern in closed grating for any given angle of incidence θ_0 if the frequency of the incident wave $\psi^{(i)}$ corresponds to a bandgap or to a band with one propagating Bloch mode.

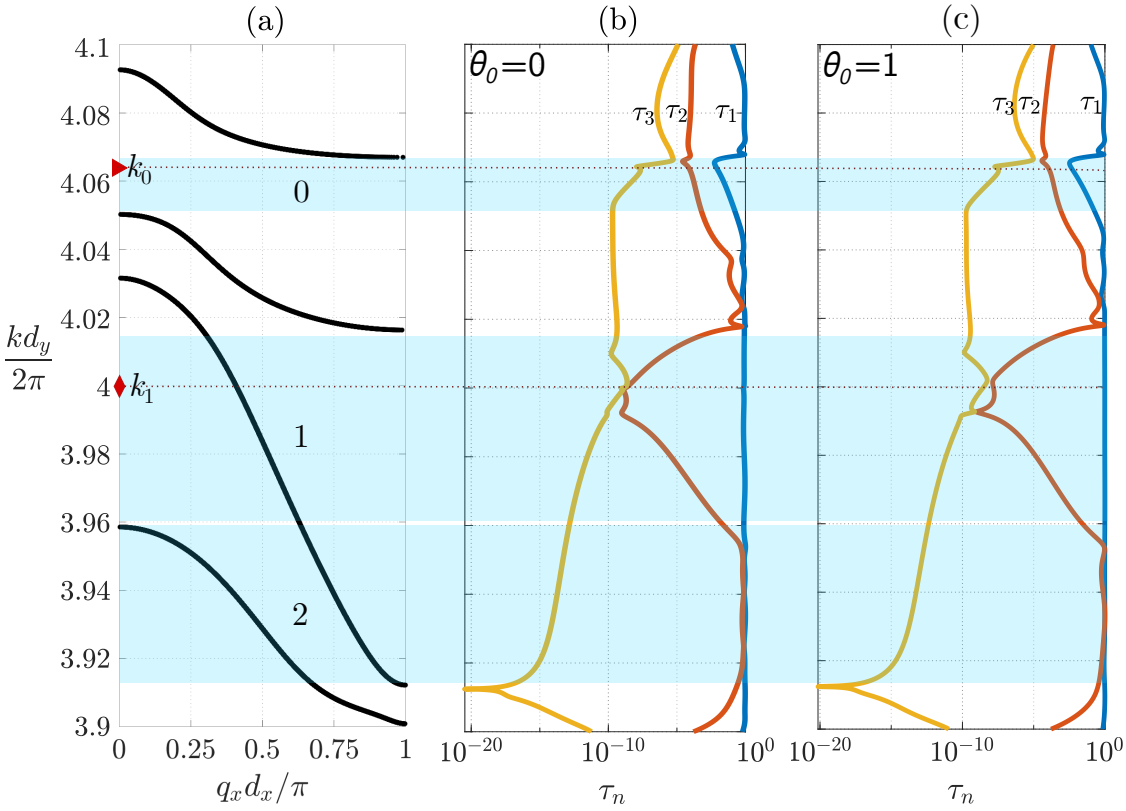

Figure 4.5 – (a) Dispersion relation of the infinite d_x-periodic waveguides with Neumann boundary conditions in the frequency range $kd_y/2\pi \in [3.9, 4.1]$. The numbers denote the number of right-going propagating Bloch modes in the corresponding colored frequency intervals. The red-filled triangle and diamond represent the frequencies $k_0 = 4.067$ and $k_1 = 4$ of the incident wave used to simulate the wavefield in Figs. (4.6) and (4.7), respectively. (b) and (c) Spectrum of the first three TEVs ($\tau_1 > \tau_2 > \tau_3$), for $\theta_0 = 0$ and $\theta_0 = 1$ rad, respectively, of the closed gratings ($M = 5$, $d_x = 2$, $d_y = 1.65$), in the same range of frequency. Numerics are performed using a mode-matching method (see App. 4.A for more details on the calculations).

The freezing of the transmitted pattern corresponds to the insensitivity to the modal amplitudes of the incoming wave on the closed grating ($\boldsymbol{a}^+(0)$), and hence to the change in the orientation of the gray rectangular scatterers. The frozen pattern is not the same for two different θ_0 (Fig. 4.C.1).

A numerical experiment of such freezing is shown in Fig. 4.6. A plane wave illuminates the closed grating at an angle of incidence $\theta_0 = 1$ rad and at a frequency $k_0 = 4.067$ that corresponds to a bandgap (Fig. 4.6 (a)). We then introduce a grating of rectangular scatterers with three different orientations (Figs. 4.6 (b)-(d)). Comparing all the configu-

rations allows us to observe the strong sensitivity of the wave pattern to the orientation of the scatterers for $x \leq 0$. Moreover, we observe a progressive freezing of the wave pattern as we move away from $x = 0$ and a complete freezing of the transmitted speckle pattern for $x \geq 0Md_x$. Only the evanescent amplitude of the transmitted wave remains dependent on the orientation of the scatterers. Numerics are performed using a finite element method (Comsol Multiphysics), although the admittance matrix method could also be employed [56–59]. It is important to note that the pattern of the transmitted field remains insensitive to any modifications made to the scatterers placed before the aforementioned closed grating, such as changing their shapes and or their dimensions.

Let us now consider the same numerical experiment as in the bandgap case, with the same angle $\theta_0 = 1$ rad, but at a frequency $k_1 = 4$ of the incident wave, which corresponds to a band with one propagating Bloch mode, see Fig. 4.7. We observe the same qualitative behavior as in the bandgap case: a strong sensitivity to the orientation of the rectangular scatterers for $x \leq 0$ and a progressive evolution of the spatial field towards an identical pattern. Only the amplitude that is no longer evanescent becomes finite and remains dependent on the orientation of the scatterers.

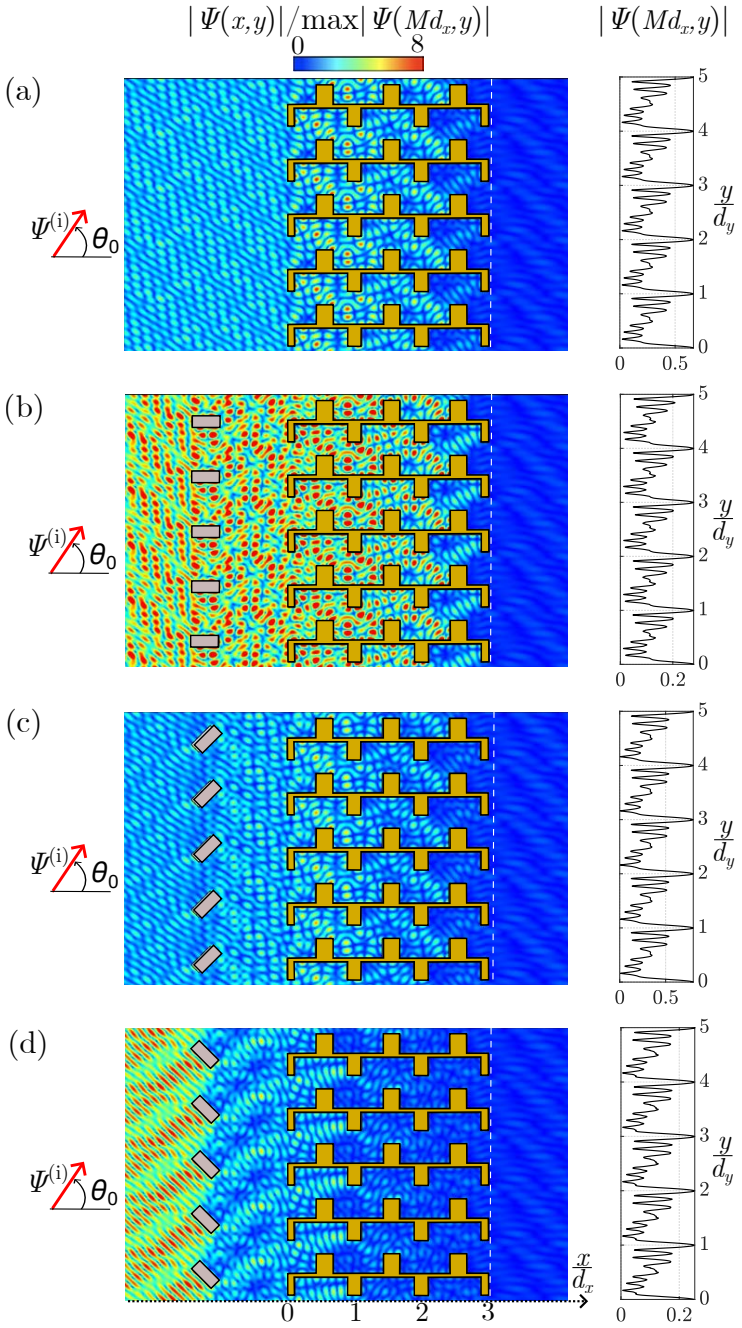

Figure 4.6 – Freezing. (a) Wavefield modulus in closed grating ($M = 3$, $d_x = 2$, $d_y = 1.65$). This grating is illuminated by a plane wave under an incident angle $\theta_0 = 1$ rad and at a frequency $k_0 = 4.067$ corresponding to a bandgap (see Fig. 4.5). (b)-(d) Adding a grating of rectangular scatterers with three different orientations. The right figures correspond to the pattern of the transmitted field $\psi(x = Md_x, y)$. Numerics are performed using a finite element method (Comsol Multiphysics).

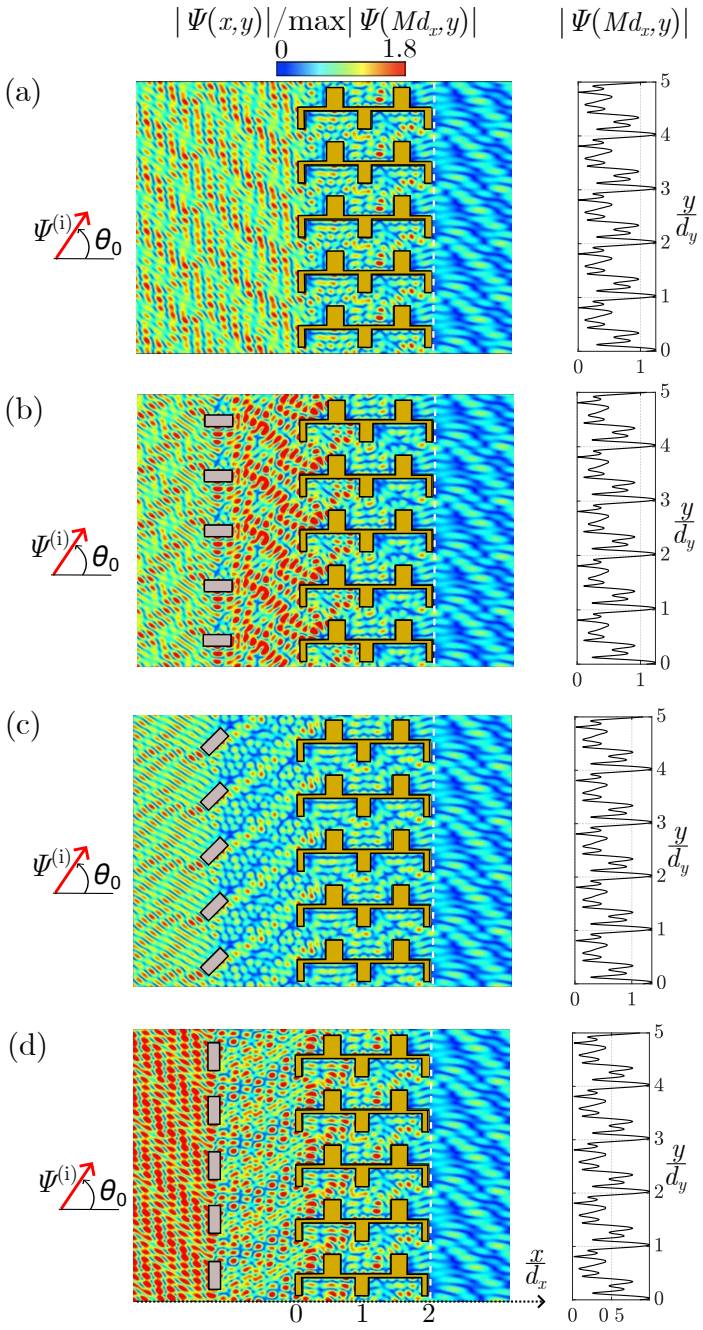

Figure 4.7 – Freezing. (a) Wavefield modulus in closed grating ($M = 2$, $d_x = 2$, $d_y = 1.65$). This grating is illuminated by a plane wave under an incident angle $\theta_0 = 1$ rad and at a frequency $k_1 = 4$ corresponding to a band with one propagating Bloch mode (see Fig. 4.5). (b)-(d) Adding a grating of rectangular scatterers with three different orientations. The right figures correspond to the pattern of the transmitted field $\psi(x = Md_x, y)$. Numerics are performed using a finite element method (Comsol Multiphysics).

4.4 Freezing with an "open" grating

Consider now the "open" grating as shown in Fig. 4.8. The open grating is made of

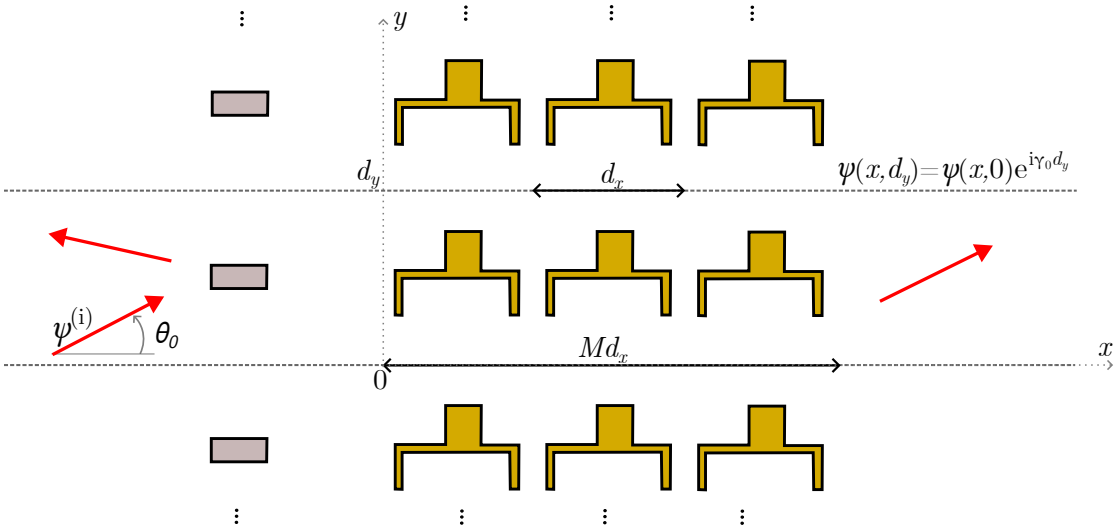

Figure 4.8 – "Open" grating made of structured horizontal waveguides, which are connected along the vertical direction y.

structured horizontal waveguides with Neumann boundary conditions at their boundaries, which are connected along the vertical direction y. The structured waveguides are d_x-periodic along the x-direction and consist of a finite number M of unit cells.

Analog to what we treated in the past sections, at both ends of the open gratings, the solution of the wave equation can be written as a multimodal formulation, see (Eq. 4.11). Let T be the transmission matrix of the open gratings.

As we did in the past section, to get the dispersion relation we consider the infinite d_x-periodic equivalent of the grating shown in Fig. 4.8. Since horizontal waveguides are now connected, the dispersion relation $k = \mathrm{f}(\mathbf{q})$ is now dependent on the vertical component q_y (App. 4.B), hence on the incidence angle θ_0. Figs. 4.9 show the dispersion relation $k = \mathrm{f}(q_x)$ and the spectrum of TEVs for two different θ_0 in a frequency range where $N = 7$. These figures show that the number of propagating Bloch modes and the TEVs depend on the choice of the frequency and θ_0. Therefore, the freezing of the transmitted field depends on the choice of k and θ_0 (App. 4.C). For a given θ_0, the frequency k should correspond to a bandgap or to a band with one propagating Bloch mode. Thus, if we illuminate the system with an incident plane wave at an angle of incidence θ_0, with a frequency in a bandgap or in a band with one propagating Bloch mode, we can expect

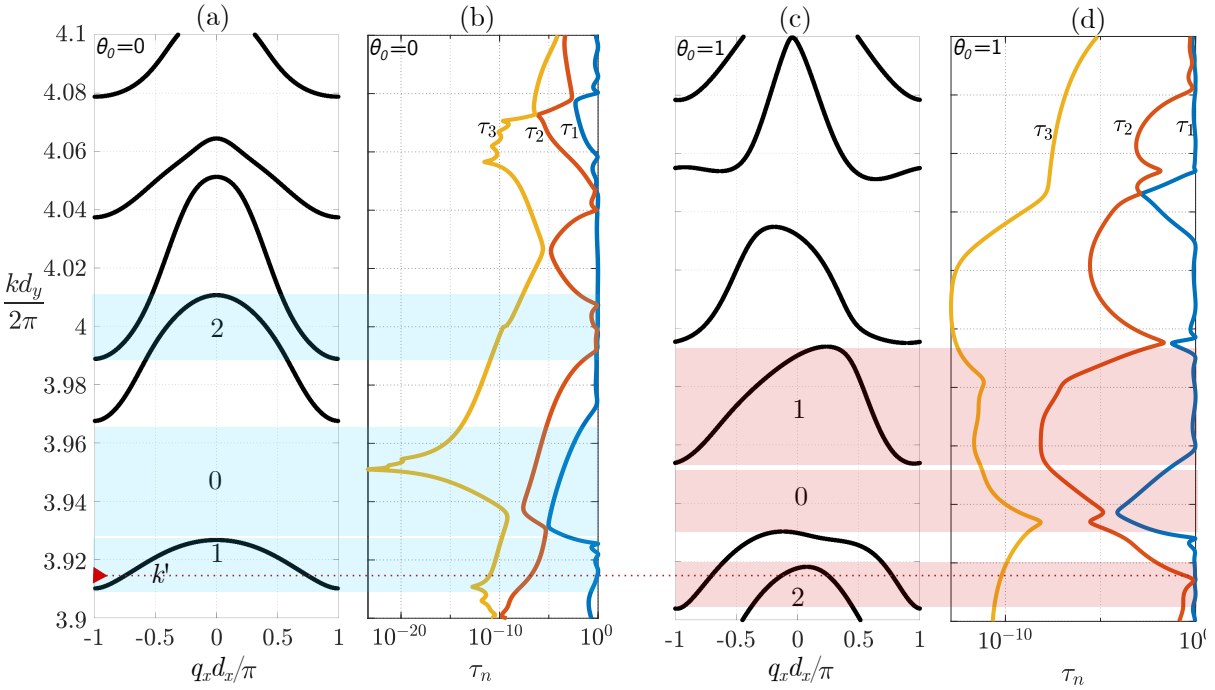

Figure 4.9 – (a) Dispersion relation of the equivalent structured waveguides in Fig. 4.8 which are infinite along the horizontal direction ($d_x = 2$, $d_y = 1.65$), in the frequency range $kd_y/2\pi \in [3.9, 4.1]$ for $\theta_0 = 0$. (b) Spectrum of the first three TEVs ($\tau_1 > \tau_2 > \tau_3$) of the open grating with $M = 5$, in the same frequency range, and for the same value of θ_0. (c) and (d) Dispersion relation and spectrum of the three TEVs for $\theta_0 = 1$ rad, respectively. The numbers indicate the number of propagating Bloch modes in the corresponding colored frequency intervals. The red-filled triangle represents the frequency $k' = 3.914$ of the incident wave used to simulate the wavefield in Figs. 4.10 and 4.11. Numerics are performed using a mode-matching method (see App. 4.A for more details on the calculations).

the transmitted speckle pattern to be insensitive to the orientation of the rectangular scatterers.

A numerical experiment of such insensitivity to the orientation of the scatterers is shown in Fig. 4.10. A plane wave illuminates the open grating with an incidence angle $\theta_0 = 0$ and at a frequency $k' = 3.914$ that corresponds to a band with one propagating Bloch mode (Fig. 4.10 (a)). We then introduce a grating of rectangular scatterers with three different orientations (Figs. 4.10 (b)-(d)). Comparing all the configurations allows us to observe the strong sensitivity of the wave pattern to the orientation of the scatterers for $x \leq 0$. We observe a progressive freezing of the wave pattern as we move away from $x = 0$ and a complete freezing of the transmitted speckle pattern for $x \geq Md_x$.

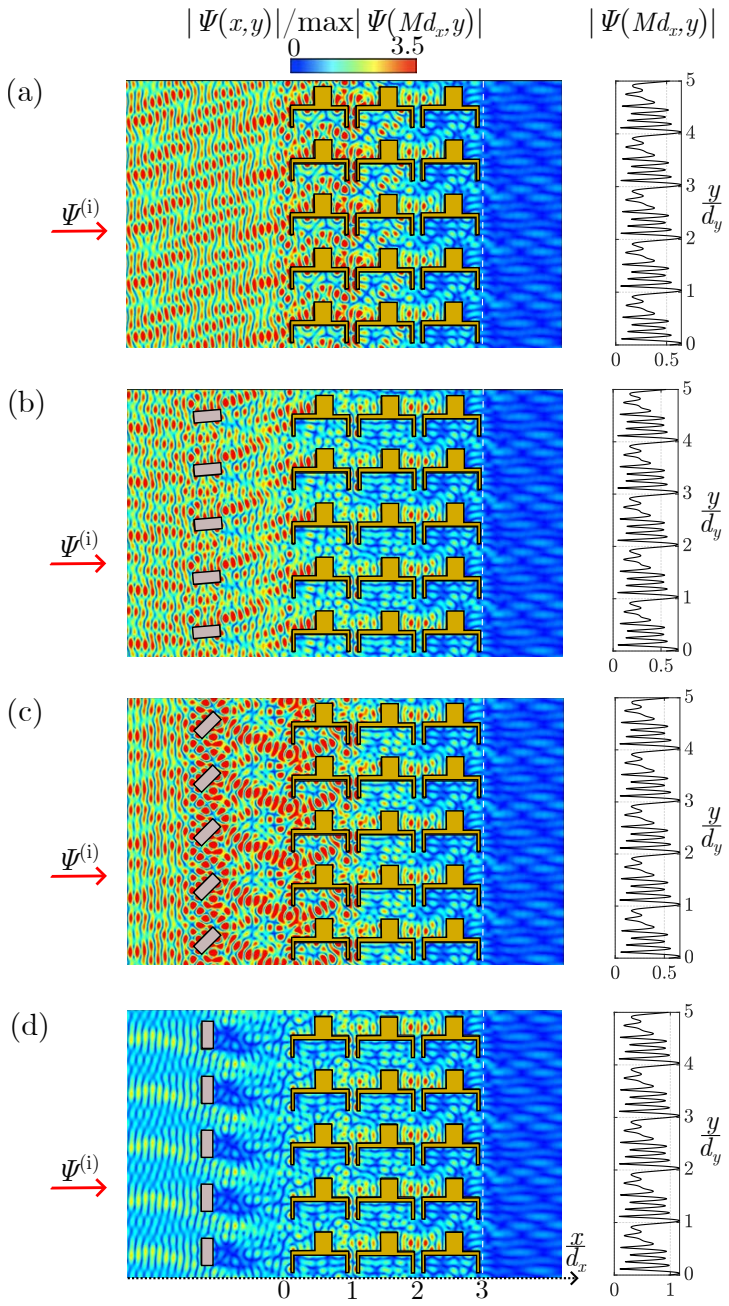

Figure 4.10 – Freezing. (a) Wavefield modulus in open grating ($M = 3$, $d_x = 2$, $d_y = 1.65$). The system is illuminated by an incident plane wave with an angle of incidence $\theta_0 = 0$ and at a frequency $k' = 3.914$ that corresponds to a band with one propagating Bloch mode (see Figs. 4.9). (b)-(d) Adding a grating of rectangular scatterers with three different orientations. The right figures correspond to the pattern of the transmitted field $\psi(x = Md_x, y)$. Numerics are performed using a finite element method (Comsol Multiphysics).

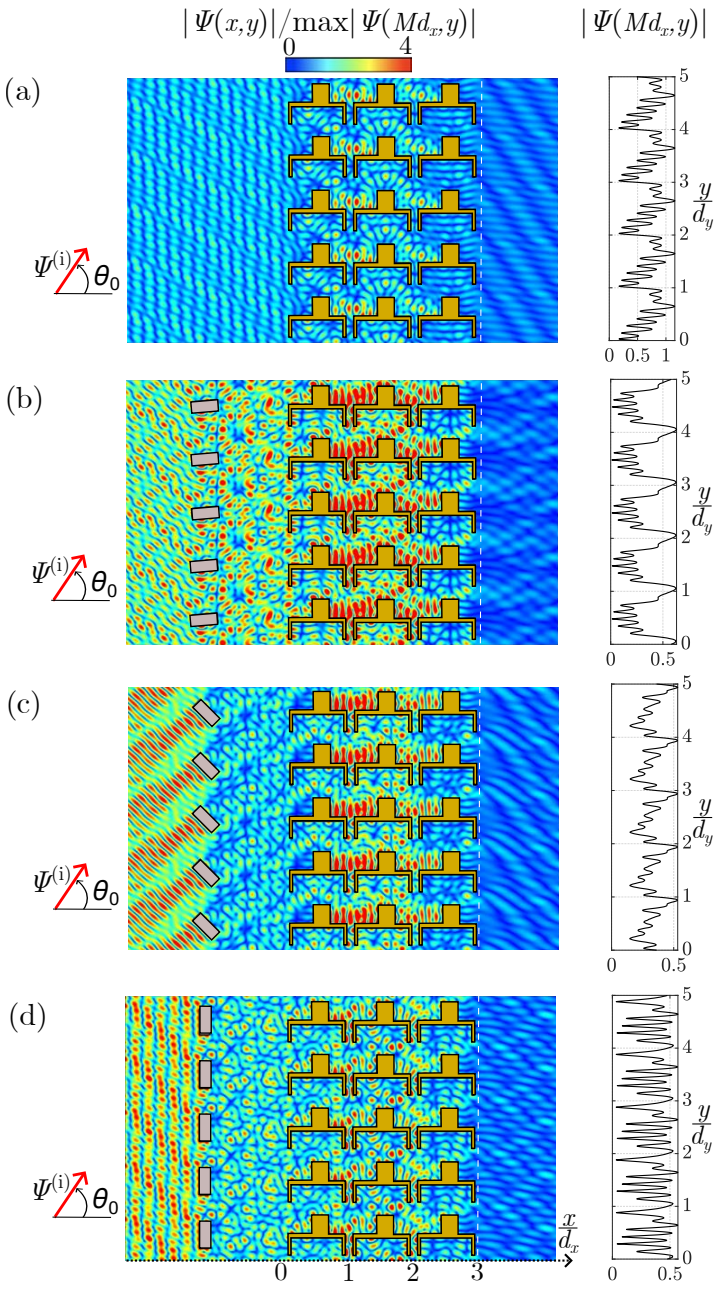

Figure 4.11 – Non-freezing. (a) Wavefield modulus in open grating ($M = 3$, $d_x = 2$, $d_y = 1.65$). The system is illuminated by an incident plane wave with an angle of incidence $\theta_0 = 1$ rad and at a frequency $k' = 3.914$ that corresponds to a band with two propagating Bloch modes (see Figs. 4.9). (b)-(d) Adding a grating of rectangular scatterers with three different orientations. The right figures correspond to the pattern of the transmitted field $\psi(x = Md_x, y)$. Numerics are performed using a finite element method (Comsol Multiphysics).

Let us now consider the same numerical experiment as the previous one and the same previous frequency of excitation $k' = 3.914$ but with an incident angle $\theta_0 = 1$ rad. At this given incident angle, the excitation frequency k' corresponds to a band with two propagating Bloch modes. Comparing all the configurations in Fig. 4.11 allows us to observe the strong sensitivity of the wave pattern to the orientation of the scatterers in the entire system.

4.5 Conclusion

In conclusion, we have shown that "closed" grating, which is made of structured horizontal waveguides that are not connected in the vertical direction, share transmission properties reminiscent of the single-channel regime observed in disordered and periodic waveguides. This results in the invariance of the transmitted speckle pattern to the orientation of the rectangular scatterers, hence to the incident wave on the closed gratings. This freezing of the transmitted pattern is observed if the frequency of the incident wave corresponds to a bandgap or a band with one propagating Bloch mode at any given incident angle. We have also shown that the freezing of the transmitted pattern can also be obtained in "open" grating, which is made of structured horizontal waveguides that are connected in the vertical direction if the frequency of the incident wave also corresponds to a bandgap or a band with one propagating Bloch mode but for a specific range of incident angle.

APPENDIX

4.A Mode matching method

A mode matching method is used in this chapter to compute the dispersion relation ($k = \mathrm{f}(q_x)$) and the TEVs given in Figs. 4.5 and 4.9. In order to get the dispersion relation in Fig. 4.5 (a), the first step is to calculate the scattering matrix S of a unit cell (Fig. 4.A.1

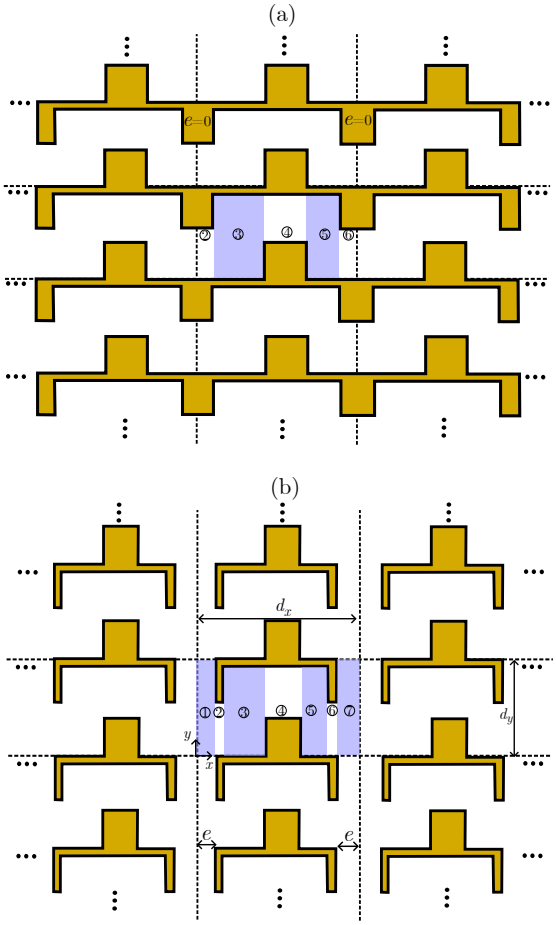

Figure 4.A.1 – (a) Infinite periodic waveguides that are not connected along the vertical direction, $e = 0$. (b) Infinite periodic waveguides that are connected along the vertical direction, $e \neq 0$. In a unit cell, the continuous lines represent Neumann boundary conditions, and the dashed lines represent pseudo-periodic boundary conditions.

(a)), which corresponds to the unit cell of a periodic waveguide with Neumann boundary conditions. The calculation is detailed the App. 2.A.

For a given θ_0, the TEVs in Fig. 4.5 (b) and (c) can be obtained by calculating the scattering matrix S_t of the closed grating made of M-finite d_x-periodic waveguides,

$$\mathsf{S}_t = \mathsf{S}^{(1-2)} \star \mathsf{S}_M \star \mathsf{S}^{(6-7)}, \tag{4.13}$$

where $\mathsf{S}^{(1-2)}$ is given by Eq. (4.20), S_M is the scattering matrix of the M-finite d_x-periodic waveguide which can be computed by using M times the composition product [31] of the scattering matrix S and $\mathsf{S}^{(6-7)}$ can be can be calcuted similarly to $\mathsf{S}^{(1-2)}$ as we will see in the following. From this, we can deduce the transmission matrix given by Eq. (4.12) and consequently the TEVs.

To obtain the dispersion relation in Fig. 4.9 (a) and (c). The first step is to calculate the scattering matrix S of a unit cell (Fig. 4.A.1 (b)). The cell is a piecewise constant waveguide element with different boundary conditions (Neumann for the continuous lines and periodic for the dashed lines), composed of seven discontinuously connected segments with length $l^{(j)}$ and width $h^{(j)}$, $1 \leq j \leq 7$ (note that $l^{(7)} = l^{(1)} = e$, $h^{(7)} = h^{(1)} = d_y$, $l^{(6)} = l^{(2)} = 0.1d_x - e$, $h^{(6)} = h^{(2)} = 1$, $h^{(5)} = h^{(3)}$ and $th = h^{(3)} - h^{(4)}$).
For this structure the dimensions of the unit cell are $d_x = 2$, $d_y = 1.65$, $e = 0.0625d_x$, $(h^{(3)}, h^{(4)}) = (1.53, 0.58)$ and $(l^{(3)}, l^{(4)}, l^{(5)}) = (0.325, 0.25, 0.225)d_x$. The main difference with the structure given in Fig. 4.A.1 (a) lies in the value of $e = 0$.

In each segment, a multimodal formulation of the wavefield is given as,

$$\psi^{(j)}(x, y) = \boldsymbol{g}^{(j)^{\mathsf{T}}}(y)(\boldsymbol{a}^{(j)+}(x) + \boldsymbol{a}^{(j)-}(x)), \tag{4.14}$$

with $\boldsymbol{a}^{(j)+}(x)$ (resp. $\boldsymbol{a}^{(j)-}(x)$) the vector of the modal coefficient of the right- (resp. left-) going wave and $\boldsymbol{g}^{(j)}$ the vector of the transverse eigenfunctions. These eigenfunctions are,

$$g_n^{(1)}(y) = g_n^{(7)}(y) = \frac{\mathrm{e}^{\mathrm{i}\gamma_n^{(1)}y}}{\sqrt{d_y}}, \tag{4.15a}$$

$$g_n^{(2)}(y) = g_n^{(6)}(y) = \sqrt{\epsilon_n}\cos\left(\gamma_n^{(2)}y\right), \tag{4.15b}$$

$$g_n^{(3)}(y) = g_n^{(5)}(y) = \sqrt{\epsilon_n/h^{(2)}}\cos\left(\gamma_n^{(3)}y\right), \tag{4.15c}$$

$$g_n^{(4)}(y) = \sqrt{\epsilon_n/h^{(4)}}\cos\left(\gamma_n^{(4)}(y-th)\right), \tag{4.15d}$$

with $\epsilon_0 = 1$, $\epsilon_{n>0} = 2$ and

$$\gamma_n^{(1)} = \gamma_0 + n2\pi/d_y, \tag{4.16a}$$

$$\gamma_n^{(2)} = n\pi, \tag{4.16b}$$

$$\gamma_n^{(3)} = n\pi/h^{(3)}, \tag{4.16c}$$

$$\gamma_n^{(4)} = n\pi/h^{(4)}, \tag{4.16d}$$

$$\tag{4.16e}$$

with $\gamma_0 = k\sin(\theta_0)$. The transmission matrix of each segment simply reads $\mathsf{T}^{(j)} = \exp\left(\mathsf{Y}_{\mathrm{c}}^{(j)}l^{(j)}\right)$, with $\mathsf{Y}_{\mathrm{c}}^{(j)}$ the diagonal characteristic admittance matrix of the segment, given by $\mathsf{Y}_{cn}^{(j)} = \mathrm{i}(k^2 - \gamma_n^{(j)})^{1/2}$. The scattering matrix is then

$$\mathsf{S}^{(j)} = \begin{pmatrix} \mathbb{0} & \mathsf{T}^{(j)} \\ \mathsf{T}^{(j)} & \mathbb{0} \end{pmatrix}, \tag{4.17}$$

since no reflection occurs in the uniform segments. The scattering actually occurs at the discontinuous junctions, and one accounts for it by rigorously writing the mode matching that results from the continuity conditions. Consider, for example, the junction between the segments ① and ②. Writing the continuity of the wavefield and of its x-derivative, leads to (the values of $\boldsymbol{b}^{(1,2)\pm}$ below are taken at the junction abscissa)

$$\mathsf{F}(\boldsymbol{a}^{(1)+} + \boldsymbol{a}^{(1)-}) = (\boldsymbol{a}^{(2)+} + \boldsymbol{a}^{(2)-}), \tag{4.18a}$$

$$\mathsf{Y}_{\mathrm{c}}^{(1)}(\boldsymbol{a}^{(1)+} - \boldsymbol{a}^{(1)-}) = \mathsf{F}^{\mathsf{T}}\mathsf{Y}_{\mathrm{c}}^{(2)}(\boldsymbol{a}^{(2)+} - \boldsymbol{a}^{(2)-}), \tag{4.18b}$$

with F the mode-matching matrix:

$$\mathsf{F}_{mn} = \int_0^1 g_m^{(1)}(y) g_n^{(2)}(y)\,\mathrm{d}y. \tag{4.19}$$

One deduces that the S-matrix of the junction (1-2) is

$$\mathsf{S}^{(1-2)} = \begin{pmatrix} \mathsf{F} & -\mathbb{1} \\ \mathsf{Y}_{\mathrm{c}}^{(2)} & \mathsf{F}^{\mathsf{T}}\mathsf{Y}_{\mathrm{c}}^{(1)} \end{pmatrix}^{-1} \begin{pmatrix} -\mathsf{F} & \mathbb{1} \\ \mathsf{Y}_{\mathrm{c}}^{(2)} & \mathsf{F}^{\mathsf{T}}\mathsf{Y}_{\mathrm{c}}^{(1)} \end{pmatrix}. \tag{4.20}$$

Once the other junction-S-matrices obtained similarly, the scattering matrix of the whole unit cell can be computed by using iteratively the composition product, often referred to as the Redheffer star-product [31]:

$$\mathsf{S} = \mathsf{S}^{(1)} \star \mathsf{S}^{(1-2)} \star \mathsf{S}^{(2)} \star \ldots \star \mathsf{S}^{(6-7)} \star \mathsf{S}^{(7)}. \tag{4.21}$$

Thus, taking $x = 0$ as the position of the left end of the cell,

$$\begin{pmatrix} \boldsymbol{a}^{(1)-}(0) \\ \boldsymbol{a}^{(7)+}(d_x) \end{pmatrix} = \mathsf{S} \begin{pmatrix} \boldsymbol{a}^{(1)+}(0) \\ \boldsymbol{a}^{(7)-}(d_x) \end{pmatrix} \tag{4.22}$$

Assuming now a periodicity along the x-direction, the modal components above also fulfill the pseudo-periodic condition

$$\begin{cases} \boldsymbol{a}^{(7)+}(d_x) = e^{\mathrm{i}q_x d_x} \boldsymbol{a}^{(1)+}(0), \\ \boldsymbol{a}^{(7)-}(d_x) = e^{\mathrm{i}q_x d_x} \boldsymbol{a}^{(1)-}(0). \end{cases} \tag{4.23}$$

Then, writing S as

$$\mathsf{S} = \begin{pmatrix} \mathsf{R} & \mathsf{T}' \\ \mathsf{T} & \mathsf{R}' \end{pmatrix}, \tag{4.24}$$

for a given θ_0, the dispersion relation can be obtained as the solutions (q_x, k) of

$$\det \left[\begin{pmatrix} \mathsf{T} & \mathsf{R}' \\ \mathbb{0} & \mathbb{1} \end{pmatrix} - e^{\mathrm{i}q_x d_x} \begin{pmatrix} \mathbb{1} & \mathbb{0} \\ \mathsf{R} & \mathsf{T}' \end{pmatrix} \right] = 0. \tag{4.25}$$

For a given θ_0, the scattering matrix of the M-finite open gratings can be computed by using M times the composition product [31] of the scattering matrix S. From this, we

can deduce the transmission matrix, and thus the TEVs.

4.B Dispersion relation

Fig. 4.B.1(a) shows the dispersion relation $k = \mathrm{f}(q_y)$ of the infinite periodic waveguides which are not connected in the vertical direction. It shows that the dispersion relation corresponds to flat bands. While the dispersion relation of the infinite periodic waveguides connected in the vertical direction (Fig. 4.B.1(b)) corresponds to bands with zero, one, and two propagating Bloch modes.

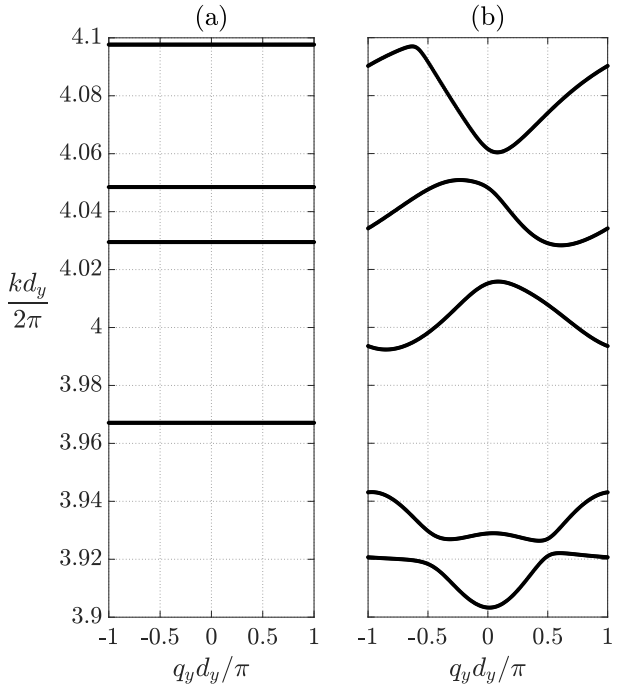

Figure 4.B.1 – (a) Dispersion relation of the infinite periodic waveguides which are not connected in the vertical direction (Fig. 4.B.1(a)) for $q_x d_x/\pi = 1/6$. (b) Dispersion relation of the infinite periodic waveguides which are connected in the vertical direction (Fig. 4.B.1(b)) for the same value of q_x. The periodicities along both directions are $d_x = 2$ and $d_y = 1.65$. Numerics are performed using a finite element method (Comsol Multiphysics).

4.C Closed grating

Fig. 4.C.1 (a) and (b) show the freezing of the transmitted pattern with an incident plane wave at a frequency $k_1 = 4$ corresponding to a band with one propagating Bloch mode and with an angle of incidence $\theta_0 = \pi/12$. Fig. 4.C.1 (c) and (d) also show the freezing of the transmitted pattern at the same frequency $k_1 = 4$ but with a different angle of incidence $\theta_0 = \pi/4$. The patterns of Fig. 4.C.1 (a) and (c) are different.

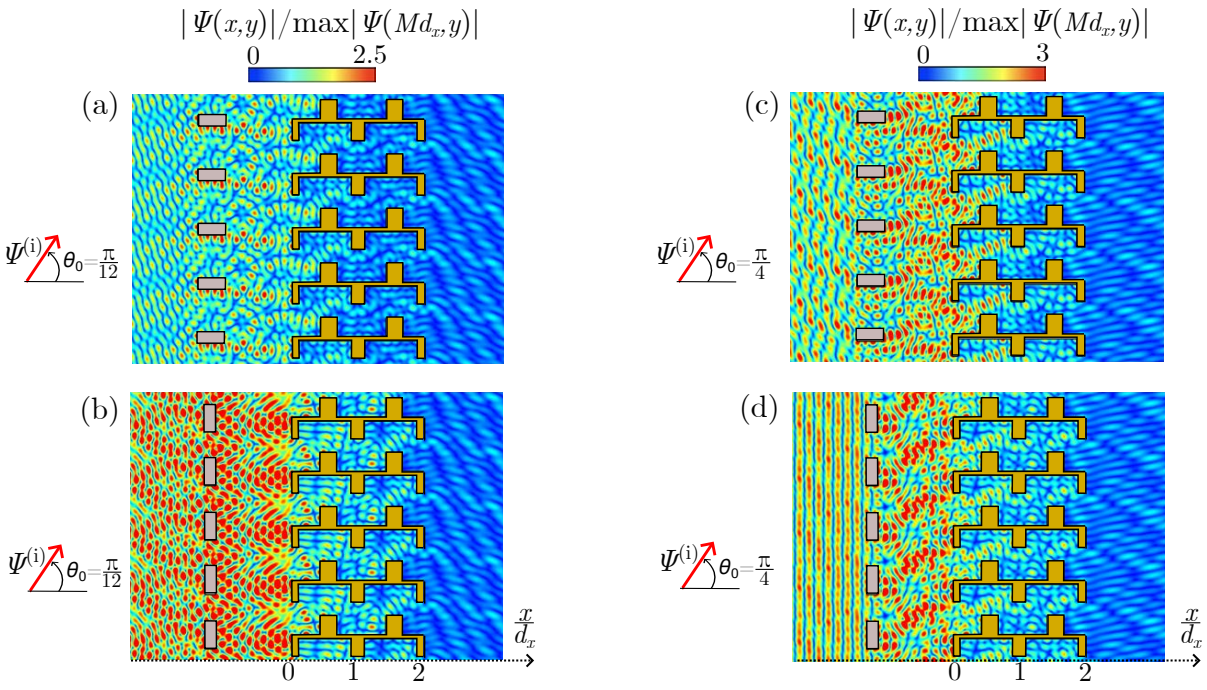

Figure 4.C.1 – Wavefield modulus in closed grating ($M = 2$, $d_x = 2$, $d_y = 1.65$) for two different orientations of the rectangular scatterers. The gratings are illuminated by a plane wave at a frequency $k_1 = 4$ corresponding to a band with one propagating Bloch mode (see Fig. 4.5). (a) and (b) Freezing with an angle of incidence $\theta_0 = \pi/12$. (c) and (d) Freezing with an angle of incidence $\theta_0 = \pi/4$. Numerics are performed using a finite element method (Comsol Multiphysics).

Chapter 5

Enhanced transmission through an opaque barrier in a periodic waveguide

5.1 Introduction

In the previous chapters, we have shown that the freezing phenomenon is not intrinsically related to the localized regime in disordered media and can also be observed in periodic media. In this chapter, we show that another intriguing phenomenon observed

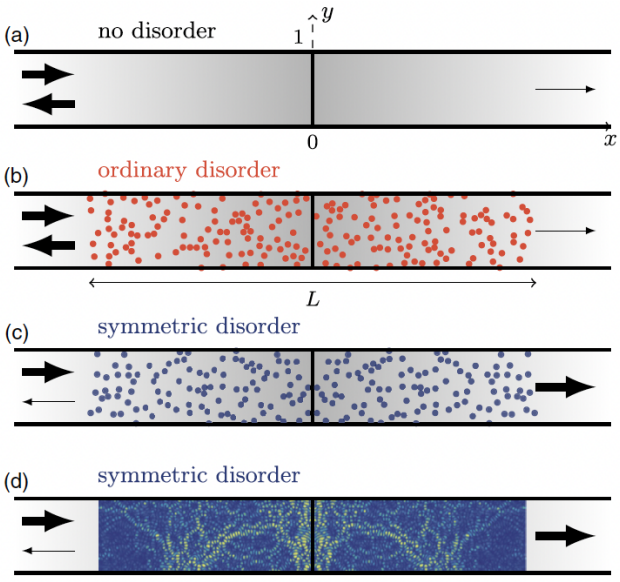

Figure 5.1 – Sketches of the studied scattering systems. (a) Opaque barrier in 2D waveguide with unitary width. (b) Same as (a), with randomly distributed scatterers on both sides of the barrier. (c) Same as (b), but with a left-right symmetry of the scatterers position. (d) Typical open eigenchannel in the symmetrical case, as sketched in (c). Source: E. Chéron et al. [60].

by E. Chéron et al. [60] in the diffusive regime in disordered media can also be observed in periodic media. We begin with a short reminder of this latter result. This intriguing phenomenon corresponds to a significant and broadband enhancement of the transmission through an opaque barrier when placed between symmetric diffusive disordered slabs as shown in Fig. 5.1. It is induced by multiple scattering interferences, which are inherent to the diffusive transport of waves. One of their results is shown in Fig. 5.2. They com-

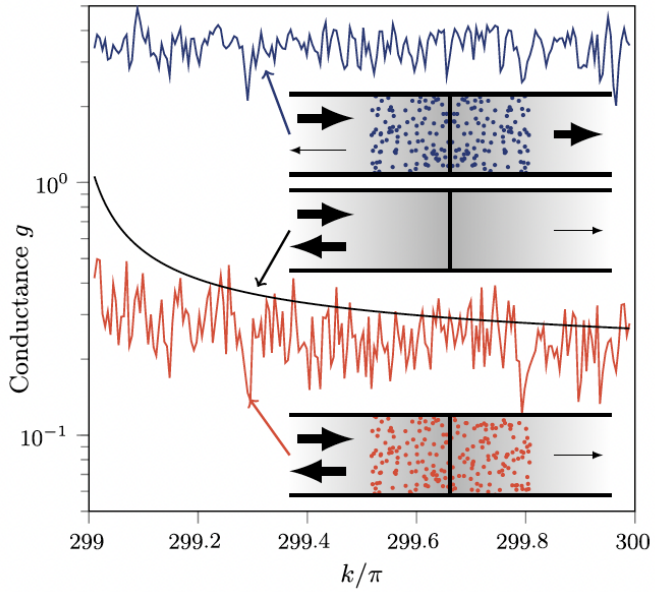

Figure 5.2 – Enhanced transmission through an opaque barrier when it is placed in the middle of a left-right symmetric disordered waveguide. Spectrum of the conductance in the frequency range $k/\pi \in]299, 300[$ with k the wavenumber. The waveguide supports $N = 300$ propagating modes. Three configurations are considered. Black: the barrier alone. Red: the barrier, in the middle of a disordered slab with length $L = 5$ and $l = 0.14$ the mean free path, $l \ll L \ll Nl$. Blue: the barrier, in the middle of a left-right symmetric disorder slab for the same L and l. In the last two cases, the conductance is not averaged and comes from a single realization of the disorder. Source: E. Chéron et al.[60].

pared the spectrum of the conductance g for three different configurations. Recall that the conductance characterizes the total transmission (Eq. (5.5)). They plotted the spectrum of the conductance of the barrier alone. Then, as expected, when the barrier is placed in the middle of an ordinary disorder, the conductance decreases in amplitude. Finally, when the barrier is placed in the middle of left-right symmetric disorder, the conductance increases, and there is a broadband enhancement in transmission compared to the barrier alone, here for all the frequencies in a range $k/\pi \in]299, 300[$ with k the wavenumber.

The authors [60] have constructed a scaling model that can predict the behavior of the averaged conductance $\langle g \rangle$ (the average is over multiple configurations of the disorder) as a function of the length L of the disordered slab and the transmittance of barrier alone. It is based on the semi-classical description of the conductance through a double quantum-dot by Whitney et al. [61], and it uses the statistical properties of the conductance in the diffusive regime, which obeys Ohm's law,

$$\langle g \rangle = \frac{Nl}{L+1}. \tag{5.1}$$

This surprising phenomenon was experimentally evidenced in a microwave experiment when an aluminum bar was placed in the middle of a left-right symmetric disordered system [48]. The phenomenon of the enhanced transmission induced by the mirror symmetry has also been studied when a barrier is placed in the middle of left-right symmetric chaotic cavities [61], where the authors showed that a huge conductance peak is caused by the symmetry in double quantum dots of chaotic shape.

In this chapter, we show that this phenomenon can also be observed in symmetric periodic waveguides, as shown in Fig. 5.3.

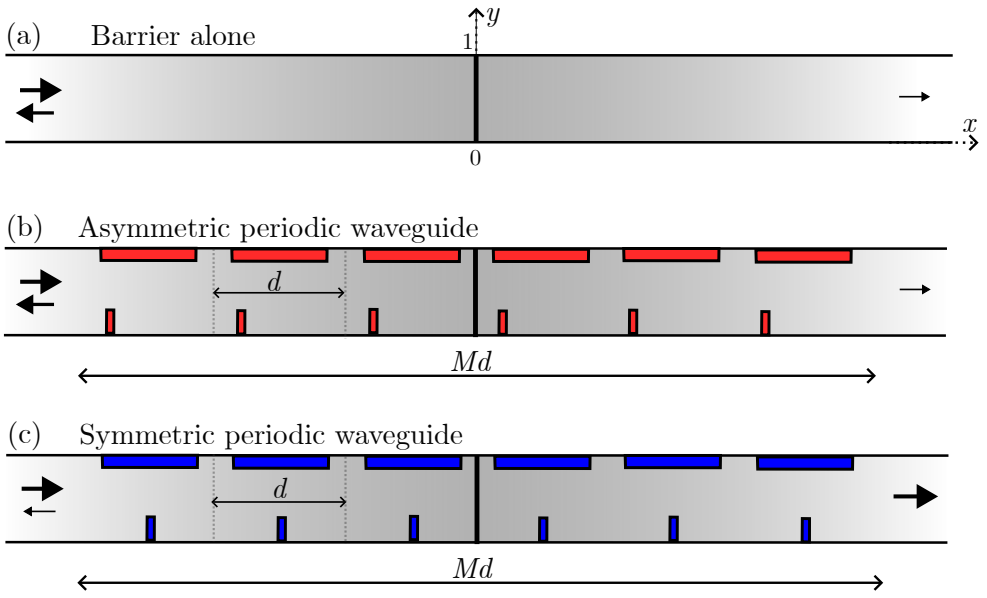

Figure 5.3 – Sketches of studied scattering systems. a) Opaque barrier in a 2D waveguide. (b) Opaque barrier in the middle of an asymmetric finite d-periodic waveguide composed of M unit cells. (c) Same as (b), with a symmetric finite periodic waveguide.

To do this, we will first give a brief explanation of the barrier model, which allows us to define barrier transmittance. We will also recall the definition of conductance, which characterizes the transmission through a complex medium. After that, we will compare the transmission for three different cases: barrier alone, barrier in the center of an asymmetric periodic waveguide, and finally, barrier in the center of a symmetric periodic waveguide. Then, we will continue our studies to optimize the transmission enhancement by observing the evolution of the conductance as a function of the barrier transmittance and as a function of the length of the symmetric periodic waveguide. For these studies, the barrier is placed in the center of the system. Finally, we will study the sensitivity of the transmission enhancement to symmetry defects.

5.2 Conductance enhancement

Let us consider the barrier alone placed at $x = 0$ in an infinite waveguide with rigid boundary conditions at $y = 0$ et $y = 1$ as shown in Fig. 5.3 (a). We are solving the Helmholtz equation

$$(\Delta + k^2)\psi(x, y) = 0, \tag{5.2}$$

with k the wavenumber. We assume that the waveguide supports N propagating modes, $N = E(k/\pi) + 1$, with E the greatest integer function. Let W_{tr} be the conductance of the barrier. It depends on the frequency and a parameter α representing the " strength" of the barrier since the barrier is defined by the following interface condition,

$$\begin{cases} [\partial_x \psi(x)]_0 = 0, \\ [\psi(x)]_0 = \alpha \partial_x \psi(0), \end{cases} \tag{5.3}$$

where the jump of the function f at $x = 0$ is defined by $[f(x)]_0 = \lim_{h\to 0} f(h) - f(-h)$. As the positive real parameter α increases from zero to infinity the barrier changes from fully transparent to fully opaque. We invite the reader to refer to [60] for more details on the barrier model. In reduced form, the transmittance is given by:

$$\tau(\alpha) = W_{tr}/N, \tag{5.4}$$

and it is upper bounded by $\tau(\alpha = 0) = 1$ (the barrier is transparent), and it drops rapidly as α increases.

Let us consider the case when the barrier is placed in the middle of a finite d-periodic

waveguide composed of M unit cells as shown in Fig. 5.3 (b) and (c). Let T be the transmission matrix and g be the dimensionless conductance of the medium; it measures the total transmission due to the contribution of the transmission of all incoming transverse modes

$$g = \mathrm{Tr}\left(\mathsf{T}\mathsf{T}^{\dagger}\right) = \sum_{n,m=1}^{N} |T_{nm}|^2 \,. \tag{5.5}$$

Fig. 5.4 shows the spectrum of the conductance g of the three cases in Fig. 5.3. It

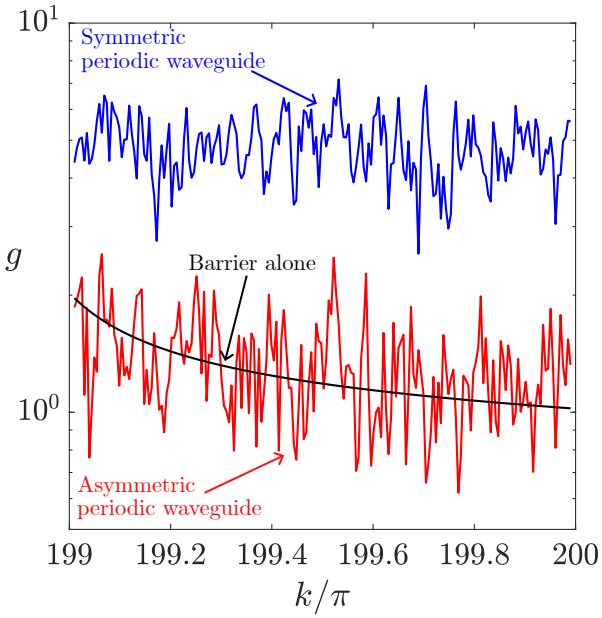

Figure 5.4 – Enhanced transmission through an opaque barrier when it is placed in the middle of a symmetric periodic waveguide. The conductance g is plotted in the frequency range $k/\pi \in [199,\ 200]$ where $N = 200$. Three configurations are considered. Black: the barrier alone, with a "strength" parameter $\alpha = 0.08$. Red: the barrier in the middle of an asymmetric periodic waveguide ($M = 12$, $d = 2$). Blue: the barrier in the middle of a symmetric periodic waveguide (same M and d).

shows that when the barrier is in the middle of an asymmetric periodic waveguide, the conductance is of the same order of magnitude as the barrier alone. But when the barrier is in the middle of a symmetric periodic waveguide, there is indeed an enhancement of the transmission compared to the transmission of the barrier alone, similar to the phenomenon observed in the disordered waveguide (Fig. 5.2). The averaged conductance $\langle g \rangle \simeq 5$ is 4 times the averaged conductance of the barrier $\langle W_{tr} \rangle = 1.25$. Here, we averaged over the corresponding frequency range $k/\pi \in]199, 200[$ where $N = 200$.

Let us now take a closer look at the symmetry-induced conductance enhancement and how it can be modified by varying the average barrier transmittance $\langle\tau\rangle$ (varying α) and the length of the two symmetric periodic waveguides Md. Fig. 5.5 shows the variation of the average conductance with M for different values of the average transmittance of the barrier. The averaging is done over the frequency ranges $k/\pi \in]N-1, N[$ with $N = 200$.

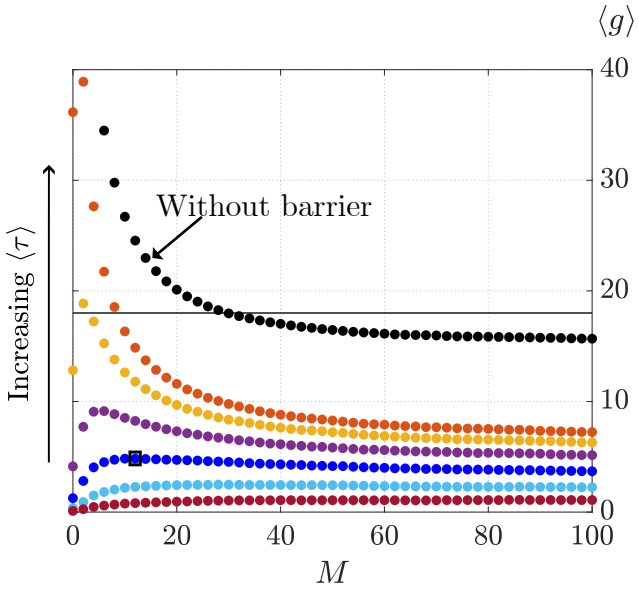

Figure 5.5 – Average conductance $\langle g\rangle$ of the symmetric periodic waveguide as a function of the number of unit cells M, for different values of the barrier mean transmittance $\langle\tau\rangle$ (different values of α). The barrier is always located in the center of the symmetric periodic waveguide. The black filled circle corresponds to the configuration without barrier ($\langle\tau\rangle = \tau = 1$). The black horizontal line corresponds to the average number of propagating Bloch modes $\langle N_B\rangle \simeq 18$ of the equivalent infinite periodic waveguide (without barrier). The conductance, the barrier transmittance, and the number of propagating Bloch modes are averaged over a frequency range $k/\pi \in]199, 200[$ where $N = 200$. The configuration used to obtain Fig. 5.4 is indicated by the black rectangle.

Generally, starting from the value of the barrier average conductance,

$$\langle g\left(M = 0, \langle\tau\rangle\right)\rangle = N\langle\tau\rangle, \tag{5.6}$$

the average conductance increases, reaches a maximum value g_{opt} corresponding to an optimal number of unit cells surrounding the barrier, then decreases, and finally $\langle g\left(M = 100, \langle\tau\rangle\right)\rangle$ tends to a finite value g_{100} for $M = 100$. Here, we have stopped the numerical calculations at $M = 100$, but even for $M > 100$, the mean value of the conductance tends to a finite

value.

Fig. 5.5 also shows that by increasing the transmittance of the barrier, the overall level of conductance will increase, where the upper black-colored data is the case without a barrier. The average conductance (without barrier) decreases from the initial value

$$g\left(M=0,\tau=1\right)=N, \tag{5.7}$$

and eventually tending to a finite value

$$\langle g\left(M=100,\tau=1\right)\rangle \simeq N_B=18, \tag{5.8}$$

where N_B is the number of propagating Bloch modes of the equivalent infinite d-periodic waveguide (without barrier).

Comparing the periodic case with the disordered case [60], where the conductance is averaged over several realizations of the disorder, the same qualitative behavior is observed, but while in the periodic case, in the limit of long length $M \gg 1$, the conductance tends to a finite value g_{100} for different values of the barrier transmittance, in the disordered case, in the case of long length $L \gg l$, the conductance is expected to vanish $g(L \to \infty) = 0$. Thus, in the periodic case, we can expect an enhancement of the transmission even in the long length limit, as shown in Fig. 5.6 (a). It shows the average conductance g_{100} over different frequency ranges $k/\pi \in]N-1, N[$ as a function of the barrier transmittance $\langle\tau\rangle$, where a noticeable threshold, $\langle\tau\rangle < \tau_{100}$, is required to achieve a transmission enhancement in the limit of long length periodic waveguides.

We also observed the evolution of the maximum value of the average conductance $\langle g\left(M,\langle\tau\rangle\right)\rangle = g_{opt}$ over different frequency ranges $k/\pi \in]N-1, N[$ as a function of the barrier transmittance $\langle\tau\rangle$ (Fig. 5.6 (b)). We also noticed a threshold, $\langle\tau\rangle < \tau_{opt}$, required to obtain a transmission enhancement, as it has been observed in the disordered case.

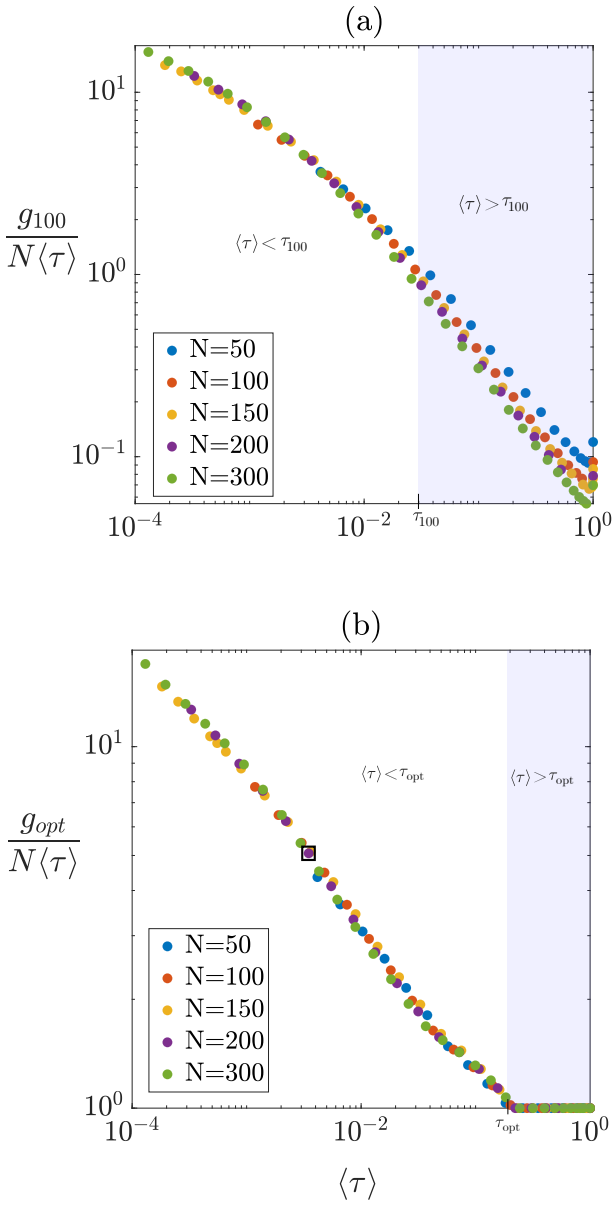

Figure 5.6 – (a) Average conductance g_{100} of a 100-cell symmetric periodic waveguide over different frequency range $k/\pi \in]N-1, N[$ as function of the average barrier transmittance $\langle\tau\rangle$. τ_{100} indicates the threshold in order to get an enhancement in transmission in the limit of long-length periodic waveguides. The barrier is in the center. (b) Maximum value of the averaged conductance g_{opt} over different frequency range $k/\pi \in]N-1, N[$ as function of the average barrier transmittance $\langle\tau\rangle$. τ_{opt} indicates the threshold in order to get an enhancement in transmission. The black rectangle indicates the configuration used to get Fig. 5.4.

5.3 Symmetry breaking

5.3.1 Shifted scatterer

The sensitivity of the enhanced transmission due to symmetry breaking has been studied in disordered waveguides [62, 63] and in double quantum dots [64, 65]. Here, we study this sensitivity in a finite d-periodic waveguide, where the symmetry is broken by shifting a scatterer from its original position for two configurations, as shown in Fig. 5.7.

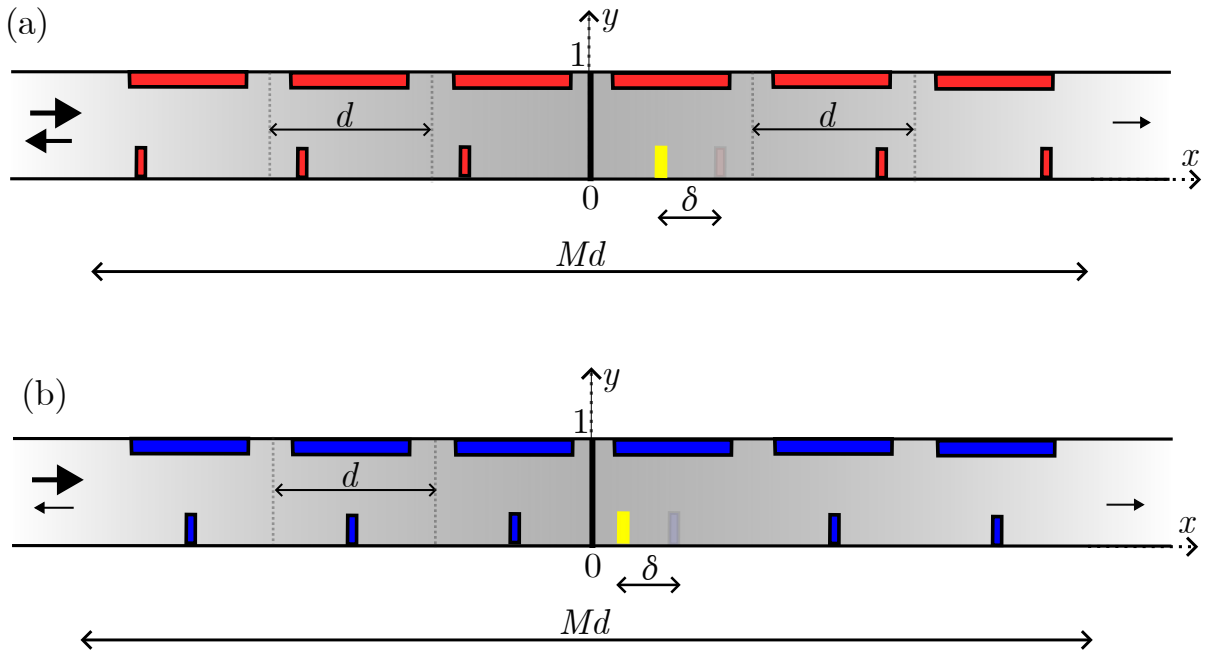

Figure 5.7 – Barrier in the middle of two symmetric finite d-periodic waveguides. (a) The unit cell is asymmetric. (b) The unit cell is symmetric. For both cases, the symmetry breaking is done by shifting the scatterer by a distance δ. The shifted scatterer is displayed in yellow.

Fig. 5.8 shows that, for both configurations, the average conductance decreases rapidly when the defect is close to the barrier and increases as the defect moves away from the barrier.

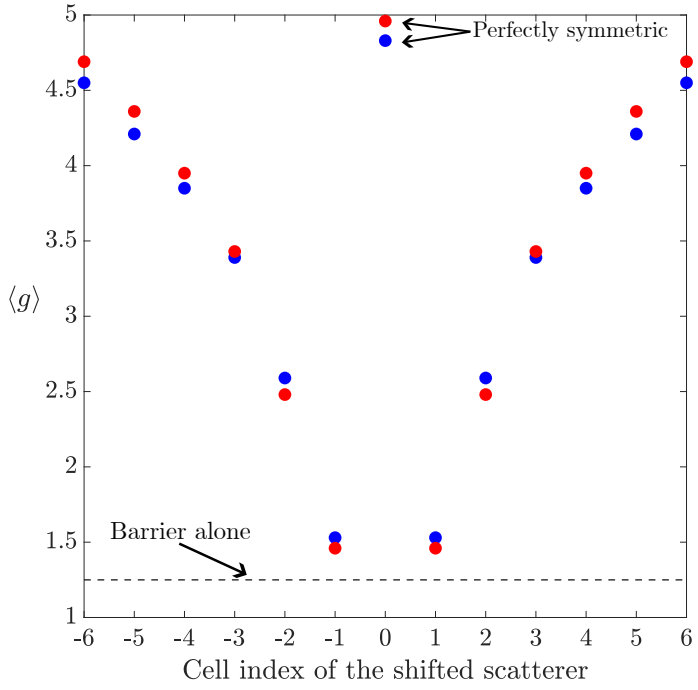

Figure 5.8 – Average conductance as a function of the cell index of the shifted scatterer for $N = 200$. No scatterer is shifted for the zero index: perfect symmetry. The black dashed line corresponds to the average conductance of the barrier alone $\langle W_{tr} \rangle$ with $\alpha = 0.08$. The red-filled dots correspond to the configuration in Fig. 5.7(a), where $M = 12$ and $d = 2$. The blue-filled dots correspond to the configuration in Fig. 5.7(b) for the same values of M and d.

5.3.2 Shifted Barrier

To get insight into the effect of the defect of symmetry, we have also studied the case where the symmetry is broken by shifting the barrier from its original position in the symmetric periodic waveguide as shown in Fig. 5.9.

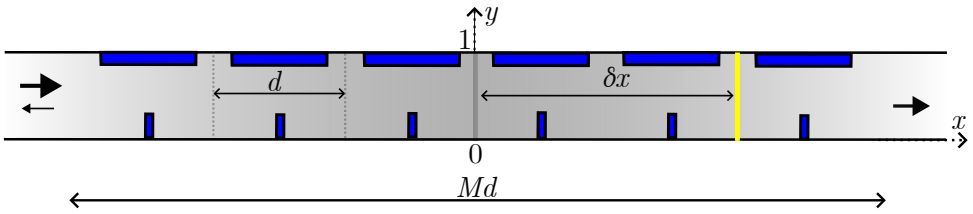

Figure 5.9 – Shifting the barrier by a distance δx from its original position at $x = 0$. The shifted barrier is displayed in yellow. The barrier is located in a finite d-periodic waveguide made of M symmetric unit cells.

Fig. 5.10 shows that there is an enhancement in transmission every $\delta x = md/2$ with m an integer due to the d_y periodicity of the waveguide and due to the symmetry of the unit cell. These functions decrease in amplitude as the barrier approaches

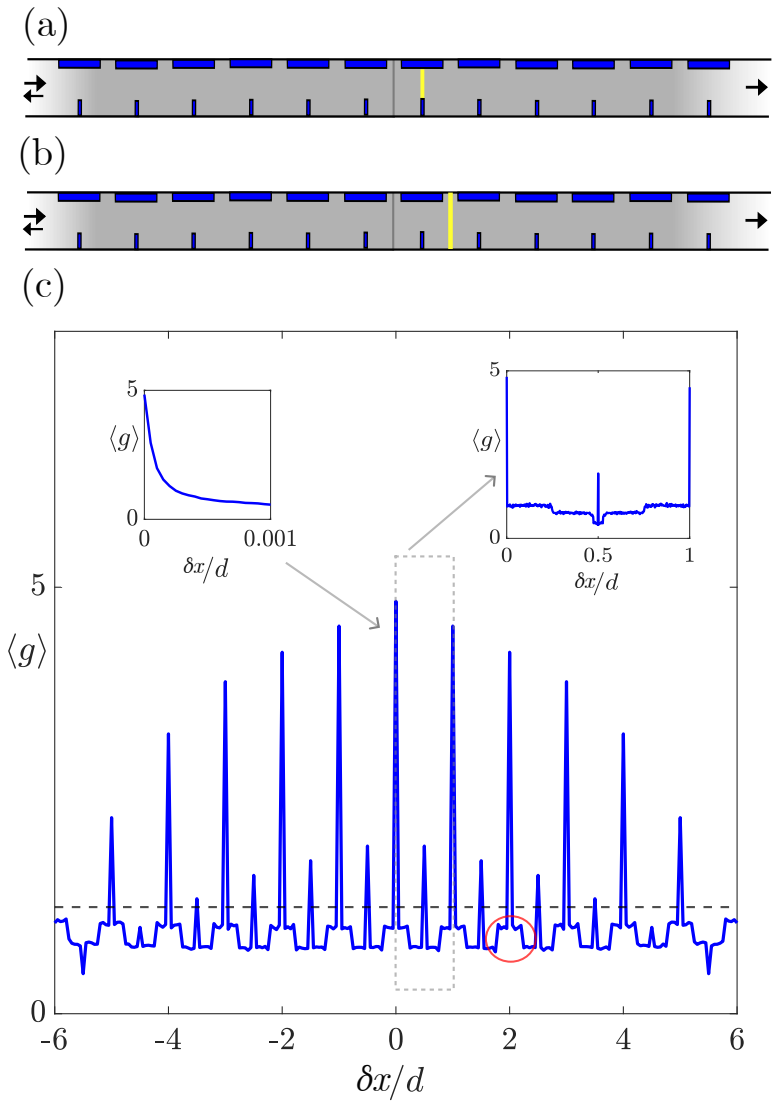

Figure 5.10 – Enhanced transmission through an opaque barrier when it is shifted by $\delta x = md/2$, with m an integer, from the center of symmetry $x = 0$ of the finite periodic waveguide with $M = 12$, $d = 2$.(a) The barrier is shifted by $\delta x = d/2$. (b) The barrier is shifted by $\delta x = d$. (c) Average conductance $\langle g \rangle$ as a function of δx for $N = 200$. Insets: Zoom on a region where $\delta x/d \in [0, \lambda/10]$ where λ is the wavelength, and zoom on a region where $\delta x/d \in [0, 1]$. The black dashed horizontal line represents the average conductance of the barrier alone ($\langle W_{tr} \rangle = 1.25$) with strength parameter $\alpha = 0.08$ and for $N = 200$.

from the left (resp. right) end of the finite periodic waveguide, namely from $\delta x = -M/2$ (resp. $\delta x = M/2$). Otherwise, there is no enhancement in transmission due to the sub-wavelength sensitivity to the barrier position, as has been shown in the disordered waveguide (Fig. 5.11). Note that the periodic jump in the average conductance (red circle in

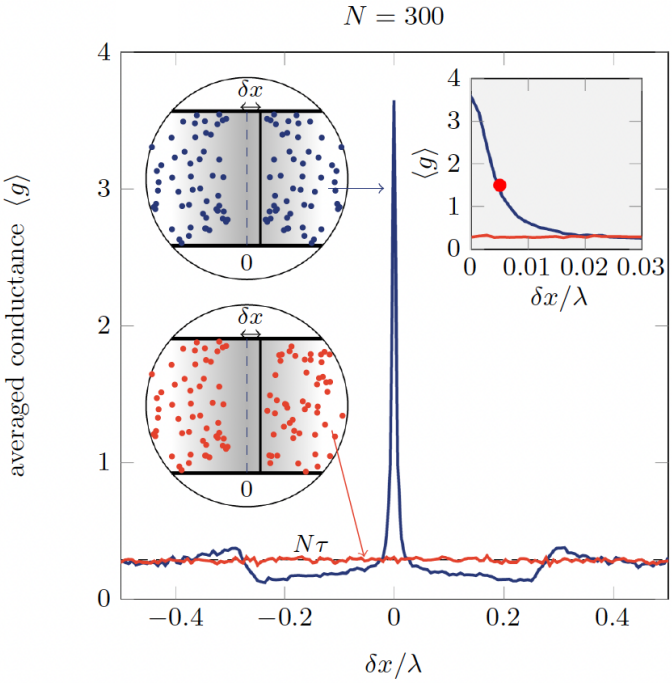

Figure 5.11 – Subwavelength sensitivity to symmetry defects in disordered waveguide. Decrease in conductance when shifting the barrier by a distance δx from the symmetry axis at $N = 300$. Ordinary disorder (red). Symmetric disorder (blue). Source: E. Chéron et al. [63].

Fig. 5.10) occurs when the width of the waveguide varies, which is due to the decrease in transmittance of the barrier alone for the same strength parameter α.

An example of transmission enhancement for $\delta x = 3d$ is shown in Fig. 5.12. It shows that there is a small decrease in amplitude compared to the case where $\delta x = 0$.

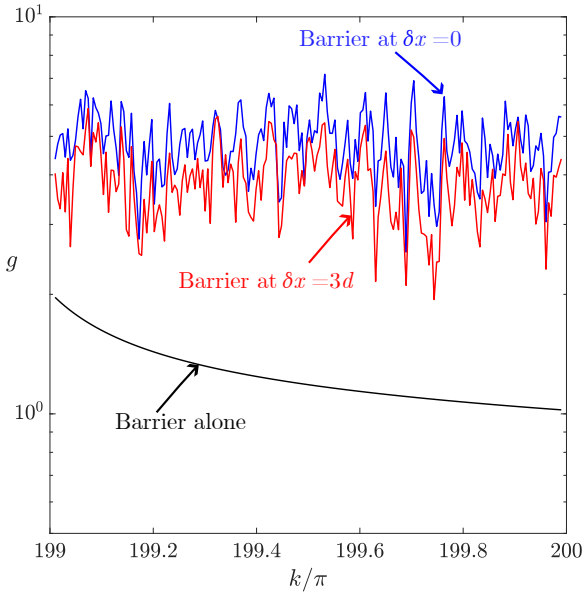

Figure 5.12 – Spectrum of the conductance at $N = 200$ with $\alpha = 0.08$. Small decrease in conductance when shifting the barrier a distance $\delta x = 3d$ from the symmetry axis in a finite periodic waveguide composed of $M = 12$ symmetric unit cells.

5.4 Conclusion

We have shown that the phenomenon of enhanced transmission when an opaque barrier is placed in the center of spatially symmetric scatterers can also be observed in a periodic waveguide. The periodic waveguide differs from the disordered waveguide as it allows transmission enhancement even in the long length limit $M \gg 1$. We have also shown that the enhancement in the transmission is sensitive to symmetry defects, but due to the periodicity, for some symmetry defects (for example, shifting the barrier in a periodic waveguide with a symmetric unit cell), there is an enhancement in transmission for $\delta x = md/2$. Otherwise, there is no enhancement in transmission due to the subwavelength sensitivity to the barrier position as in the disordered case.

General conclusions and perspectives

In this manuscript, we have first studied the invariance of transmitted speckle patterns to incident conditions. This phenomenon, which we often refer to as "freezing" of the transmitted pattern, was first shown in disordered media. Therefore, in the introductory chapter, we give a general overview of the different transport regimes in these media, highlighting the difference between the diffusive and the localized regime. In the diffusive regime, the transmission is carried by multiple transmission eigenchannels (eigenvectors of $\mathsf{T}\mathsf{T}^\dagger$), changing the incidence conditions will lead to different linear combinations of these channels, the complex transmitted pattern is thus sensitive to these changes. In contrast, in the localized regime, also known as the single-channel regime, since the transmission is dominated by a single transmission eigenchannel, the transmitted speckle pattern is insensitive to incidence conditions, only the amplitude which decays exponentially as a function of the length of the disordered media, remains dependent.

In the second chapter, we showed that the single-channel regime is not only associated with disordered media but can also be observed in other complex media, typically periodic waveguides. We showed that the single-channel regime corresponds to a frequency within a bandgap or a band with a propagating Bloch mode of the periodic medium. By numerical computation of the wavefield in a finite periodic waveguide, we have shown that the transmitted pattern is insensitive to the source position, and hence to the incidence conditions, when the excitation frequency corresponds to at most one propagating Bloch mode. The periodic case differs from the disordered case in that it allows freezing of the transmitted pattern with one propagating Bloch mode and hence non-exponentially weak transmission.

Moreover, in the third chapter, we presented an experimental observation of the frozen pattern of the transmitted pressure field in a finite periodic waveguide. This observation is made under the conditions discussed in the second chapter; the excitation frequency is within a bandgap or a band with a propagating Bloch mode. We have also observed that the pattern of the output pressure remains insensitive to the source positions when the

output boundary condition is changed from absorbing to rigid.

Furthermore, in the fourth chapter, we showed that the freezing of the transmitted pattern is not intrinsically related to periodic waveguides and can also be observed in gratings with finite periodic structures in the propagation direction. While the grating is illuminated by a plane wave with incident angle θ_0, we added another grating made of rectangular scatterers with different orientations to change the incident conditions on the grating of interest. Both gratings have the same periodicity d_y along the transverse direction. We showed that in the case of a so-called "closed" grating, a grating of finite periodic waveguides that cannot communicate along the transverse direction, the pattern of the transmitted field is insensitive to the orientations of the rectangular scatterers if for any given θ_0 the frequency of the incident plane wave satisfies the freezing conditions, namely at most one propagating Bloch mode in the direction of propagation of the equivalent infinite periodic waveguides. The pattern of the frozen field depends on θ_0. While in the case of the so-called "open" grating, a grating of finite periodic waveguides that can communicate along the transverse direction, the freezing conditions depend on the choice of frequency and the angle of incidence θ_0.

Finally, in the fifth chapter, we have shown that another surprising phenomenon—a significant and broadband enhancement of transmission through an opaque barrier when placed between symmetric diffusive disordered waveguides—can also be observed in periodic media. We showed that when the barrier is in the middle of a finite symmetric periodic waveguide, the transmission is four times that of the barrier alone. We also observed that for a long length limit (a large number of M unit cells), there is also an enhancement in transmission. We also studied the case of symmetry breaking, typically when the barrier is shifted by δx from its original position, the center of the finite symmetric periodic waveguide, where we showed that due to the d-periodicity and due to the symmetry of the unit cell, there is recurrent enhancement in transmission when $\delta x = \frac{md}{2}$ with integer m.

Perspectives

In this thesis, we have initiated several aspects of wave propagation in periodic media. We present some preliminary ideas and results that provide perspectives and avenues of research for future studies.

Rare events: non-freezing in bandgap

The freezing phenomenon is a characteristic of the single-channel regime, namely, when the first transmission eigenvalue is much larger than the second one($\tau_1 \gg \tau_2$). We have shown in Chap. 2 that this condition corresponds to a frequency within the bandgap or to a band with one propagating Bloch mode of the periodic medium. However, for some rare events that occur only in the bandgap, we have observed that $\tau_1 \simeq \tau_2$ (Fig. 5.13 (a) and (b)), thus the transmitted pattern is sensitive to the incidence conditions. We propose for future studies to characterize these rare events, which also occur in the localized regime in the disordered waveguide as shown in Fig. 5.13 (c).

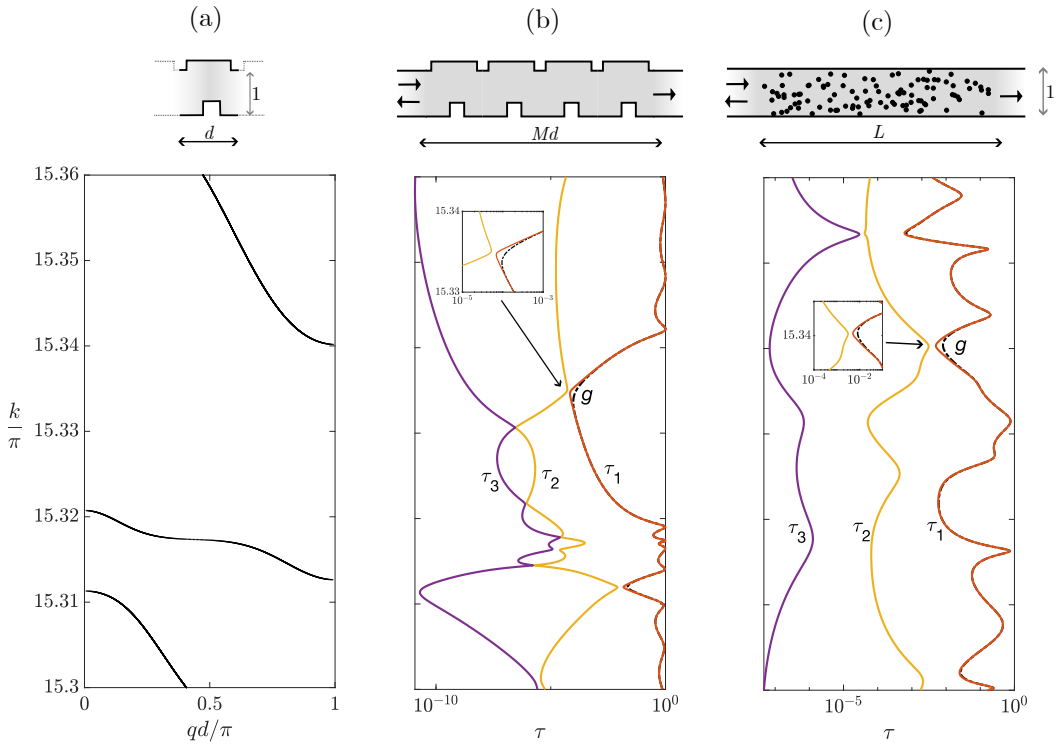

Figure 5.13 – (a) Dispersion relation of the infinite d-periodic waveguide ($d = 1.5$) in the frequency range $k/\pi \in [15.3, 15.36]$. (b) Spectrum of the conductance g (black dashed line) and the transmission eigenvalues (colored solid lines) of the equivalent finite periodic waveguide ($M = 10$) in the same frequency range. Inset: Zoom on a region where $\tau_1 \simeq \tau_2$. (c) Spectrum of the conductance g (black dashed line) and the transmission eigenvalues (colored solid lines) of the disordered waveguide in the localized regime, $s = L/l \simeq 34 > N = 16$, where l is the mean free path and N is the number of propagating modes outside the scattering region, and in the same frequency range as in (a) and (b). Inset: Zoom on a region where $\tau_1 \simeq \tau_2$.

Effects of losses

In certain experimental contexts, losses are unavoidable and can complicate the visualization of phenomena. In acoustic waveguides, such losses can arise from various mechanisms, such as the background medium, and viscous and thermal losses at the hard walls which are particularly pronounced in narrow waveguides. Thus, it is crucial to account for these losses not only to accurately describe and interpret experiments but also because they can significantly affect the transmission characteristics of the medium. Therefore, as a second perspective, we propose to study the robustness of both phenomena discussed in this thesis in a periodic medium, namely the insensitivity of the transmitted field to incident conditions and the transmission enhancement induced by the symmetry, when absorption is introduced.

Unidirectional freezing

In this thesis, we showed that for a given excitation frequency, if there is only one right-going propagating Bloch mode in a finite periodic waveguide, the transmitted pattern at the right end of the waveguide is insensitive to the incidence conditions. Since our system is reciprocal, for the same excitation frequency, if we send two different incident waves from the right end of the waveguide, the transmitted wave pattern at the left end will also remain unchanged. Freezing is bidirectional. But what if the reciprocity of the system is broken? Thus, we can imagine a new periodic configuration where only one Bloch mode propagates to the right while two Bloch modes propagate to the left. In this case, the freezing of the transmitted field will depend on the direction of the incident wave. A possible way to break reciprocity within the periodic waveguide is to use the thermoacoustic effect through this new configuration shown in Fig. 5.14. It corresponds to a finite periodic thermoacoustic waveguide [66–70], where the interaction of an acoustic wave in narrow channels submitted to a temperature gradient leads to a break in reciprocity. Finally, we proposed a third perspective to study unidirectional freezing in thermo-acoustic periodic waveguides.

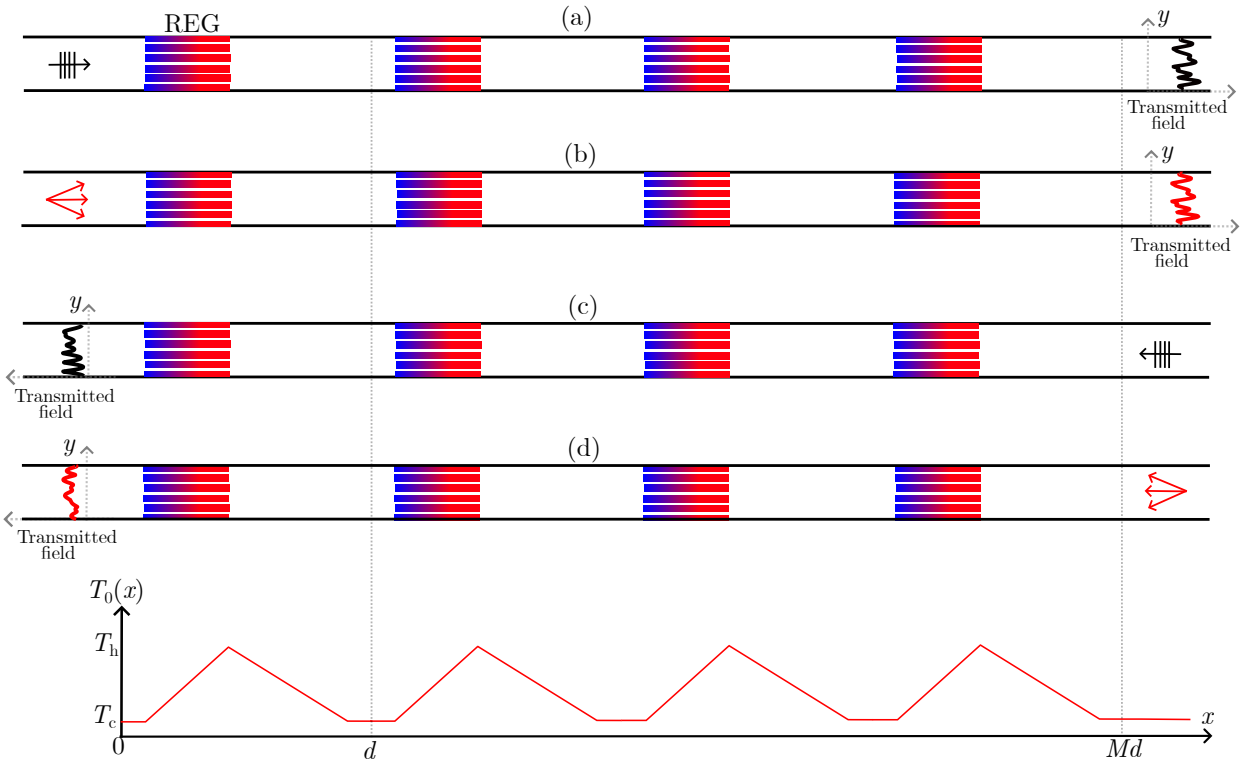

Figure 5.14 – Unidirectional freezing. Typical schematic of a finite d-periodic thermoacoustic waveguide composed of M unit cells. The unit cell consists of a regenerator (REG), also called a stack, which consists of narrow channels. A temperature gradient is imposed on the REG, $\Delta T_0 = T_h - T_c$, where T_c is the ambient temperature. (a) and (b) Two different incident conditions are imposed at the left end of the waveguide. The pattern of the transmitted field is insensitive to the incident conditions. (c) and (d) Two different incident conditions are imposed at the right end of the waveguide. The transmitted field pattern is sensitive to the incident conditions.

BIBLIOGRAPHY

[1] John D Joannopoulos, Steven G Johnson, Joshua N Winn, and Robert D Meade. Molding the flow of light. *Princet. Univ. Press. Princeton, NJ [ua]*, 2008.

[2] E. Akkermans and G. Montambaux. *Mesoscopic physics of electrons and photons*. Cambridge University Press, 2007.

[3] A García-Martín and J Sáenz. Statistical properties of wave transport through surface-disordered waveguides. *Waves in Random and Complex Media*, 15(2):229–268, 2005.

[4] S. Rotter and S. Gigan. Light fields in complex media: Mesoscopic scattering meets wave control. *Rev. Mod. Phys.*, 89:015005, 2017.

[5] É. Chéron, J.-P. Groby, V. Pagneux, S. Félix, and V. Romero-García. Experimental characterization of rigid scatterer hyperuniform distributions for audible acoustics. *Phys. Rev. B*, 106:064206, 2022.

[6] Olivier Leseur. *Diffusion, localisation et absorption de lumière en milieux désordonnés. Impact des corrélations spatiales du désordre*. PhD thesis, Université Pierre et Marie Curie-Paris VI, 2016.

[7] Z. Shi and A. Z. Genack. Transmission eigenvalues and the bare conductance in the crossover to anderson localization. *Phys. Rev. Lett.*, 108:043901, 2012.

[8] P. Sheng. *Introduction to Wave Scattering, Localization, and Mesoscopic Phenomena*. Academic Press, 1995.

[9] P. W. Anderson. Absence of diffusion in certain random lattices. *Phys. Rev.*, 109:1492, 1958.

[10] Patrick A Lee and TV Ramakrishnan. Disordered electronic systems. *Reviews of modern physics*, 57(2):287, 1985.

[11] Richard L Weaver. Anderson localization of ultrasound. *Wave motion*, 12(2):129–142, 1990.

[12] Hefei Hu, A Strybulevych, JH Page, Sergey E Skipetrov, and Bart A van Tiggelen. Localization of ultrasound in a three-dimensional elastic network. *Nature Physics*, 4(12):945–948, 2008.

[13] AA Chabanov, M Stoytchev, and AZ Genack. Statistical signatures of photon localization. *Nature*, 404(6780):850–853, 2000.

[14] Diederik S Wiersma, Paolo Bartolini, Ad Lagendijk, and Roberto Righini. Localization of light in a disordered medium. *Nature*, 390(6661):671–673, 1997.

[15] Georg Maret, Tilo Sperling, Wolfgang Bührer, Andreas Lubatsch, Regine Frank, and Christof M Aegerter. Inelastic scattering puts in question recent claims of anderson localization of light. *Nature Photonics*, 7(12):934–935, 2013.

[16] A. Peña, A. Girschik, F. Libisch, S. Rotter, and A. A. Chabanov. The single-channel regime of transport through random media. *Nature Commun.*, 5:3488, 2014.

[17] V Pagneux and A Maurel. Scattering matrix properties with evanescent modes for waveguides in fluids and solids. *The Journal of the Acoustical Society of America*, 116(4):1913–1920, 2004.

[18] R Carminati, JJ Saenz, J-J Greffet, and M Nieto-Vesperinas. Reciprocity, unitarity, and time-reversal symmetry of the s matrix of fields containing evanescent components. *Physical review A*, 62(1):012712, 2000.

[19] Rolf Landauer. Spatial variation of currents and fields due to localized scatterers in metallic conduction. *IBM Journal of research and development*, 1(3):223–231, 1957.

[20] Y. Imry and R. Landauer. Conductance viewed as transmission. *Rev. Mod. Phys.*, 71:S306, 1999.

[21] CWJ Beenakker and B Rajaei. Exact solution for the distribution of transmission eigenvalues in a disordered wire and comparison with random-matrix theory. *Physical Review B*, 49(11):7499, 1994.

[22] O. N. Dorokhov. Transmission coefficient and the localization length of an electron in N bound disordered chains. *JETP Lett.*, 36:318, 1982.

[23] O. N. Dorokhov. On the coexistence of localized and extended electronic states in the metallic phase. *Solid State Commun.*, 51:381, 1984.

[24] Y. Imry. Active transmission channels and universal conductance fluctuations. *Europhys. Lett.*, 1:249, 1986.

[25] P. A. Mello, P. Pereyra, and N. Kumar. Macroscopic approach to multichannel disordered conductors. *Ann. Phys.*, 181:290, 1988.

[26] P. A. Mello and J.-L. Pichard. Maximum-entropy approaches to quantum electronic transport. *Phys. Rev. B*, 40:5276, 1989.

[27] A. D. Stone, P. A. Mello, K. Muttalib, and J.-L. Pichard. *Random matrix theory and maximum entropy models for disordered conductors, in Mesoscopic Phenomena in Solids, edited by B. L. Altschuler, P. A. Lee and R. A. Webb*, chapter 9. North Holland, Amsterdam, 1991.

[28] C. W. J. Beenakker. Random-matrix theory of quantum transport. *Rev. Mod. Phys.*, 69:731, 1997.

[29] AMS Mace and JT Chalker. Effects of spin-orbit interactions in disordered conductors: A random-matrix approach. *Physical Review B*, 46(23):14985, 1992.

[30] Francesco Mezzadri. How to generate random matrices from the classical compact groups. *arXiv preprint math-ph/0609050*, 2006.

[31] R. Redheffer. Inequalities for a matrix Riccati equation. *J. Math. Mech.*, 8:349, 1959.

[32] Elie Cheron. *Guides d'ondes et transport dans les milieux désordonnés: effets de la symétrie et de la localisation*. PhD thesis, Le Mans Université, 2019.

[33] I. M. Vellekoop and A. P. Mosk. Focusing coherent light through opaque strongly scattering media. *Opt. Lett.*, 32:2309, 2007.

[34] H. Yılmaz, C. W. Hsu, A. Goetschy, S. Bittner, S. Rotter, A. Yamilov, and H. Cao. Angular memory effect of transmission eigenchannels. *Phys. Rev. Lett.*, 123:203901, 2019.

[35] P. Pai, J. Bosch, M. Kühmayer, S. Rotter, and A. P. Mosk. Scattering invariant modes of light in complex media. *Nat. Photon.*, 15:431, 2021.

[36] Hiroyuki Tamura and Tsuneya Ando. Conductance fluctuations in quantum wires. *Physical Review B*, 44(4):1792, 1991.

[37] Tsuneya Ando and Hiroyuki Tamura. Conductance fluctuations in quantum wires with spin-orbit and boundary-roughness scattering. *Physical Review B*, 46(4):2332, 1992.

[38] O. Leseur, R. Pierrat, J. J. Sáenz, and R. Carminati. Probing two-dimensional anderson localization without statistics. *Phys. Rev. A*, 90:053827, 2014.

[39] J. Wang and A. Z. Genack. Transport through modes in random media. *Nature*, 471:345, 2011.

[40] M. Davy, Z. Shi, J. Wang, and A. Z. Genack. Transmission statistics and focusing in single disordered samples. *Opt. Exp.*, 21:10367, 2013.

[41] H. Yılmaz, M. Kühmayer, C. W. Hsu, S. Rotter, and H. Cao. Customizing the angular memory effect for scattering media. *Phys. Rev. X*, 11:031010, 2021.

[42] N. Bender, A. Yamilov, A. Goetschy, H. Yılmaz, C. W. Hsu, and H. Cao. Depth-targeted energy delivery deep inside scattering media. *Nat. Phys.*, 18:309, 2022.

[43] H. Cao, A. P. Mosk, and S. Rotter. Shaping the propagation of light in complex media. *Nat. Phys.*, 18:994, 2022.

[44] K. A. Muttalib. Random matrix theory and the scaling theory of localization. *Phys. Rev. Lett.*, 65:745, 1990.

[45] J.-L Pichard, N. Zanon, Y. Imry, and A. D. Stone. Theory of random multiplicative transfer matrices and its implications for quantum transport. *J. Phys. IV (France)*, 51:587, 1990.

[46] Ravitej Uppu, Manashee Adhikary, Cornelis AM Harteveld, and Willem L Vos. Spatially shaping waves to penetrate deep inside a forbidden gap. *Physical review letters*, 126(17):177402, 2021.

[47] V. Pagneux, N. Amir, and J. Kergomard. A study of wave propagation in varying cross-section waveguides by modal decomposition. Part I. Theory and validation. *J. Acoust. Soc. Am.*, 100:2034, 1996.

[48] Matthieu Davy, Clément Ferise, Élie Chéron, Simon Félix, and Vincent Pagneux. Experimental evidence of enhanced broadband transmission in disordered systems with mirror symmetry. *Applied Physics Letters*, 119(14), 2021.

[49] F. Barra, V. Pagneux, and J. Zuñiga. Diffusive transport of waves in a periodic waveguide. *Phys. Rev. E*, 85:016209, 2012.

[50] Other similarity functions can be defined, with vanishing value for two similar patterns.

[51] Lord Rayleigh. On the dynamical theory of gratings. *Proceedings of the Royal Society of London. Series A, Containing Papers of a Mathematical and Physical Character*, 79(532):399–416, 1907.

[52] J Chandezon, G Raoult, and D Maystre. A new theoretical method for diffraction gratings and its numerical application. *Journal of Optics*, 11(4):235, 1980.

[53] Evgeny Popov. *Gratings: theory and numeric applications*. Popov, Institut Fresnel, 2012.

[54] Daniel Maystre. Diffraction gratings: An amazing phenomenon. *Comptes Rendus. Physique*, 14(4):381–392, 2013.

[55] Michel Nevière and Evgeny Popov. *Light propagation in periodic media: differential theory and design*. CRC Press, 2018.

[56] Gael Favraud and Vincent Pagneux. Multimodal method and conformal mapping for the scattering by a rough surface. *Proceedings of the Royal Society A: Mathematical, Physical and Engineering Sciences*, 471(2175):20140782, 2015.

[57] Agnès Maurel, Jean-François Mercier, and Simon Félix. Wave propagation through penetrable scatterers in a waveguide and through a penetrable grating. *The Journal of the Acoustical Society of America*, 135(1):165–174, 2014.

[58] Simon Félix, Agnès Maurel, and Jean-François Mercier. Local transformation leading to an efficient fourier modal method for perfectly conducting gratings. *JOSA A*, 31(10):224–2255, 2014.

[59] Agnès Maurel, Simon Félix, J-F Mercier, Abdelwaheb Ourir, and Zine Eddine Djeffal. Wood's anomalies for arrays of dielectric scatterers. *Journal of the European Optical Society-Rapid publications*, 9, 2014.

[60] E. Chéron, S. Félix, and V. Pagneux. Broadband-enhanced transmission through symmetric diffusive slabs. *Phys. Rev. Lett.*, 122:125501, 2019.

[61] R. S. Whitney, P. Marconcini, and M. Macucci. Huge conductance peak caused by symmetry in double quantum dots. *Phys. Rev. Lett.*, 102:186802, 2009.

[62] E. Chéron, S. Félix, and V. Pagneux. Sensitivity to losses and defects of the symmetry-induced transmission enhancement through diffusive slabs. *Sci. Rep.*, 10:16635, 2020.

[63] E. Chéron, S. Félix, and V. Pagneux. Broadband subwavelength sensitivity to symmetry defects of disordered slabs. *Phys. Rev. B*, 102:134201, 2020.

[64] R. S. Whitney, H. Schomerus, and M. Kopp. Semiclassical transport in nearly symmetric quantum dots. I. Symmetry breaking in the dot. *Phys. Rev. E*, 80:056209, 2009.

[65] R. S. Whitney, H. Schomerus, and M. Kopp. Semiclassical transport in nearly symmetric quantum dots. II. Symmetry breaking due to the asymmetric leads. *Phys. Rev. E*, 80:056210, 2009.

[66] Come Olivier, Anis Maddi, Gaelle Poignand, and Guillaume Penelet. Asymmetric transmission and coherent perfect absorption in a periodic array of thermoacoustic cells. *Journal of Applied Physics*, 131(24), 2022.

[67] Tetsushi Biwa, Hiroki Nakamura, and Hiroaki Hyodo. Experimental demonstration of a thermoacoustic diode. *Physical Review Applied*, 5(064012), 2016.

[68] Haitian Hao and Fabio Semperlotti. Band structure and effective properties of one-dimensional thermoacoustic bloch waves. *Physical Review B*, 104(104303), 2021.

[69] Côme Olivier, Gaëlle Poignand, Matthieu Malléjac, Vicent Romero-García, Guillaume Penelet, Aurélien Merkel, Daniel Torrent, Jensen Li, Johan Christensen, and Jean-Philippe Groby. Nonreciprocal and even willis couplings in periodic thermoacoustic amplifiers. *Physical Review B*, 104(18):184109, 2021.

[70] Nikolaus Rott. Damped and thermally driven acoustic oscillations in wide and narrow tubes. *Zeitschrift für angewandte Mathematik und Physik ZAMP*, 20(230–243), 1969.

Résumé

Les interférences jouent un rôle important dans le transport des ondes à travers des milieux complexes, influençant significativement les caractéristiques du scattering et conduisant à de nombreuses applications en contrôle des ondes. Un exemple notable est la structure de bande du spectre de transmission dans les milieux périodiques. D'autres exemples incluent les fluctuations de conductance et la localisation d'Anderson dans les milieux désordonnés. Dans ce manuscrit, nous montrons que des phénomènes tels que l'insensibilité du motif du champ transmis à l'onde incidente ("gel" du champ transmis) ou l'amélioration de la transmission due à la symétrie spatiale des diffuseurs, observés dans les milieux désordonnés, peuvent également se produire dans les milieux périodiques, même s'ils présentent des natures différentes de propagation des ondes.

Dans cette optique, dans le chapitre introductif, nous commençons par présenter les différents régimes de transport dans un guide d'onde désordonné, en soulignant la différence entre les régimes où le gel du champ transmis est observé et ceux où il ne se manifeste pas. En optique, l'image sur un écran du champ transmis à travers un milieu désordonné opaque - le speckle - est la même quelles que soient les conditions d'éclairage. Le guide d'onde désordonné supportant N de modes propagatifs, dans lequel est placé un milieu inhomogène constitué des diffuseurs positionnés aléatoirement dans une région finie de longueur L. Dans ce guide, il existe trois différents régimes de transport. Tout d'abord, un régime balistique lorsque la longueur L est inférieure au libre parcours moyen de transport l qui représente la distance typique après laquelle l'onde perd la mémoire de sa direction initiale. Dans ce régime, l'onde traversant le milieu désordonné subit peu de scattering. Le deuxième régime est le régime diffusif lorsque le milieu est caractérisé par une longueur intermédiaire, $l \ll L \ll \xi$ où ξ est la longueur de localisation. Dans ce régime, l'onde subit des multiples scattering en traversant le milieu. Dans ce régime la transmission est assurée par plusieurs canaux propres de transmission, ainsi changer les conditions d'incidence conduit à différentes combinaisons linéaires de ces canaux, rendant ainsi le speckle du champ transmis sensible à ces changements. Le dernier régime est le régime localisé, $L \gg \xi$, où l'onde est piégée dans le désordre et la transmission décroît de façon exponentielle. Le milieu désordonné est opaque. Ce régime est également connu

sous le nom de régime à canal unique, puisque la transmission est dominée par un seul canal propre de transmission, rendant ainsi le motif du champ transmis insensible aux conditions d'incidence, seule l'amplitude, qui décroît exponentiellement en fonction de la longueur du milieu désordonné, reste dépendante.

Nous montrons, dans le deuxième chapitre, que le régime à canal unique n'est pas seulement associé aux milieux désordonnés, mais peut également être observé dans d'autres milieux complexes, notamment dans les guides d'ondes périodiques. Avec des analyses numériques et algébriques, nous montrons que le régime à canal unique correspond à une fréquence située dans une bande interdite ou une bande avec un mode de Bloch propagatif du milieu périodique. Ainsi, pour une fréquence d'excitation qui correspond à une bande interdite, nous visualisons le champ dans le guide d'ondes périodique fini. Nous observons que le champ est progressivement gelé, présentant un même motif quel que soit la position de la source (quel que soit l'onde incidente) qui l'a généré et un gel complet en transmission avec une amplitude exponentiellement faible. Nous visualisons également le champ dans le guide d'ondes périodique fini avec une fréquence d'excitation qui correspond à une bande avec un mode de Bloch propagatif. Nous constatons également que le champ est progressivement gelé indépendamment de la position de la source et un gel complet en transmission avec une amplitude finie. Nous caractérisons l'évolution spatiale du gel avec une fonction de similarité F qui est égale à l'unité lorsque les profils du champ sont les mêmes. Cette fonction est différente de l'unité lorsque les profils du champ sont différents. Nous mettons en évidence que certaines configurations permettent d'obtenir le gel du champ en transmission pour une large bande. Le cas périodique diffère du cas désordonné comme il permet d'obtenir le gel du profil du champ transmis avec un mode de Bloch propagatif, et donc une transmission qui n'est pas exponentiellement faible. Ceci devrait faciliter la mise en évidence expérimentale et la caractérisation de l'invariance du profil du champ transmis à l'onde incidente et donc à la position de la source.

Dans le troisième chapitre, nous présentons une observation expérimentale du gel dans un guide d'ondes acoustique périodique constitué de cinq cellules. Nous caractérisons expérimentalement l'invariance du profil du champ transmis à la position d'une source acoustique en visualisant le spectre de la fonction de similarité F. Cette fonction de similarité est égale à l'unité si la fréquence d'excitation correspond une bande interdite ou une bande avec un mode de Bloch propagatif du milieu périodique. Dans ces conditions, nous constatons que le profil du champ transmis est insensible à la position de la source. Sous ces mêmes conditions, nous observons également le gel du champ lorsque le guide

n'est plus anéchoique à son éxtremité mais fermé.

Dans le quatrième chapitre, nous montrons que le gel du profil du champ transmis n'est pas intrinsèquement lié aux guides d'ondes périodiques et peut également être observé dans des réseaux de diffraction (gratings) à structures périodiques finies suivant la direction de propagation. Lorsque le grating est illuminé par une onde plane avec un angle d'incidence θ_0, nous ajoutons un autre grating composé de diffuseurs rectangulaires avec des orientations différentes pour changer les conditions d'incidence sur le grating d'intérêt. Les deux gratings ont la même périodicité d_y le long de la direction transversale. Nous montrons que, dans le cas d'un grating dit " fermé", un grating de guides d'ondes périodiques finis qui ne peuvent pas communiquer dans la direction transversale, le profil du champ transmis est insensible aux orientations des diffuseurs rectangulaires si, pour un θ_0 donné, la fréquence de l'onde plane incidente satisfait les conditions de gel, à savoir au plus un mode de Bloch propagatif dans la direction de propagation des guides d'ondes périodiques infinis équivalents. Le profil du champ gelé dépend de θ_0. En revanche, dans le cas d'un grating dit " ouvert ", un grating de guides d'ondes périodiques finis qui peuvent communiquer dans la direction transversale, les conditions de gel dépendent du choix de la fréquence et de l'angle d'incidence θ_0.

Un autre phénomène intrigant observé dans les milieux désordonnés peut également être observé en milieux périodiques : un gain significatif et large bande de la transmission à travers une barrière opaque lorsqu'elle est placée entre deux milieux diffusant symétriques. Dans le cinquième chapitre, nous donnons d'abord un rappel sur les résultats obtenus en milieux désordonnés. Ce gain est induit par des interférences multiples, qui sont inhérentes au transport diffusif des ondes. Il est sensible au décalage sublongueur de la barrière de sa position d'origine. Ensuite, nous étudions ce phénomène dans le cas d'un guide d'onde périodique fini et symétrique avec une barrière placée au centre. Nous constatons que la transmission à travers ce système est quatre fois supérieure à celle de la barrière seule. Nous observons que même pour un grand nombre de cellules unitaires $M \gg 1$, il y a une amélioration de la transmission. Tandis que dans les milieux désordonnés, pour $L \gg l$, la transmission tend vers zéro. Nous étudions le cas où la symétrie est brisée, typiquement lorsque la barrière est décalée de δx de sa position d'origine, au centre du guide d'ondes périodique symétrique fini. Nous observons que le gain en transmission est sensible au décalage sublongueur de la barrière, mais en raison de la périodicité d et de la symétrie de la cellule unitaire, il y a une répetition du gain de la transmission lorsque $\delta x = \frac{md}{2}$ avec m un entier.

Finalement, nous présentons quelques idées préliminaires qui ouvrent des perspectives et des pistes pour les recherches à venir. Pour certains événements rares qui se produisent uniquement dans la bande interdite du milieu périodique, nous avons observé que la transmission est dominée par deux canaux propres de transmission, donc le profil du champ transmis est sensible aux conditions d'incidence. Nous proposons pour les études futures de caractériser ces événements rares, qui se produisent également dans le régime localisé dans les milieux désordonnés. D'autre part, dans certains contextes expérimentaux, les pertes sont inévitables et peuvent compliquer la visualisation des phénomènes. Il est donc crucial de tenir compte de ces pertes non seulement pour décrire et interpréter précisément les expériences, mais aussi parce qu'elles peuvent affecter de manière significative les caractéristiques de transmission du milieu. Par conséquent, comme une deuxième perspective, nous proposons d'étudier la robustesse des deux phénomènes discutés dans cette thèse dans un milieu périodique, à savoir l'insensibilité du profil du champ transmis aux conditions d'incidence et l'amélioration de la transmission induite par la symétrie, lorsque l'absorption est introduite. Finalement, nous suggérons une troisième perspective pour étudier le phénomène du gel dans le cas où la réciprocité est brisée dans le milieu périodique, dans le but d'obtenir le gel du champ dans une seule direction.

Titre : Structures périodiques : invariance de la transmission et effets de symétrie

Mots clés : Localisation d'Anderson, modes de Bloch, symétrie spatiale.

Résumé : Une caractéristique du régime localisé dans un milieu désordonné est l'insensibilité du speckle transmis à l'onde incidente. En optique, l'image sur un écran du champ transmis à travers un milieu désordonné opaque - le speckle - est la même quelles que soient les conditions d'éclairage. Ce phénomène remarquable peut être expliqué par l'analyse des modes propres de transmission du matériau étudié. Le régime localisé se caractérise par la prédominance d'un unique mode, la transmission de tous les autres étant significativement plus faible. Le motif du champ transmis est alors déterminé par ce seul mode, indépendamment de la source. Un phénomène analogue est possible dans un milieu ordonné, périodique, lorsque l'onde propagée dans le milieu est principalement portée par un unique mode de Bloch. L'onde propagée dans le milieu périodique est alors progressivement « gelée », présentant un même motif, quelque soit la source qui l'a générée. Le travail présenté vise à caractériser et observer expérimentalement ce phénomène dans le cas de la propagation dans un guide d'onde périodique. Il vise aussi à caractériser ce phénomène dans le cas de la transmission à travers un réseau de diffraction. Finalement nous nous intéressons aux effets de la symétrie lorsqu'une barrière opaque est placée dans un guide d'ondes périodique, en particulier au gain de la transmission induit par la symétrie.

Title: Periodic structures: transmission invariance and symmetry effects

Keywords: Anderson localization, Bloch modes, spatial symmetry.

Abstract: A characteristic of the localized regime in a disordered medium is the insensitivity of the transmitted speckle to the incident wave. In optics, the image on a screen of the transmitted field through an opaque disordered medium - the speckle – remains the same regardless of the lighting conditions. This remarkable phenomenon can be explained by analysing the eigenmodes of transmission of the studied material. The localized regime is characterized by the predominance of a single mode, with the transmission of all other modes being significantly weaker. The pattern of the transmitted field is then determined by this single mode, regardless of the source. A similar phenomenon is possible in an ordered, periodic medium, when the wave propagated in the medium is mainly carried by a single Bloch mode. The wave propagated in the periodic medium is then gradually « frozen », presenting the same pattern, regardless of the source that generated it. The presented work aims to characterize and to observe experimentally this phenomenon in the case of propagation in a periodic waveguide. It also aims to characterize this phenomenon in the case of transmission through a diffraction grating. Finally, we are interested in the effects of symmetry when an opaque barrier is placed in a periodic waveguide, specifically focusing on the transmission enhancement induced by symmetry.